OUKA
The University of Osaka
Institutional Knowledge Archive

Title	Development of Thermophysical Properties Measurement Methods for High-Temperature Liquids with Aerodynamic Levitation
Author(s)	孫, 一帆
Citation	大阪大学, 2022, 博士論文
Version Type	VoR
URL	https://doi.org/10.18910/88066
rights	
Note	

The University of Osaka Institutional Knowledge Archive : OUKA

https://ir.library.osaka-u.ac.jp/

The University of Osaka

Doctoral Dissertation

Development of Thermophysical Properties Measurement Methods for High-Temperature Liquids with Aerodynamic Levitation

Yifan Sun

January 2022

Graduate School of Engineering,
Osaka University

Division of Sustainable Energy and
Environmental Engineering

©2022 – Yifan Sun
all rights reserved.

Thesis advisor: Assosicate Professor Yuji Ohishi Yifan Sun

Development of Thermophysical Properties Measurement Methods for High-Temperature Liquids with Aerodynamic Levitation

Abstract

The loss-of-coolant accident (LOCA) at the Fukushima Daiichi Nuclear Power Plant (1F) led to core meltdowns in reactor units 1-3. In the current decommissioning process, one of the main objectives is to clarify the behavior of the molten core materials during the accident. Computational fluid dynamics (CFD) is often used to study the spread of molten core materials. However, the quality of CFD simulations depends on the accuracy of the input data, such as the molten core materials' density, heat capacity, thermal conductivity, surface tension, and viscosity. The major component of the molten core materials is molten core oxides with melting points approaching 3000 K, making measurements of their thermophysical properties challenging. This is because sample-apparatus contamination is a significant source of error at such elevated temperatures.

In order to prevent sample-apparatus contact, levitation techniques are promising methods in the study of molten core materials. With aerodynamic levitation (ADL), molten core oxides can be levitated and heated over 3000 K with minimal contamination. The development of measurement methods for ADL has been slow because of issues with sample deformation, visibility, and heat loss. Although ADL is being used to measure the density, surface tension, and viscosity of molten oxides, the aforementioned problems introduce various levels of uncertainty in the measured result. It is therefore necessary to improve the reliability of the thermophysical properties measurement methods used with ADL in order to utilize it in the study of molten core oxides.

In this work, I will introduce new measurement methods for density, heat capacity, surface tension, and viscosity for ADL. The 'drop method' for density measurement makes sure the sample is not deformed and fully visible during the experiment. The 'multiple-gas cooling method' for heat capacity measurement introduces a simplified model to describe the radiative and convective heat loss experienced by the sample. Finally, the 'drop-bounce method' for surface tension and viscosity measurement removes the influence of the levitation gas on the sample's resonant frequency. The introduction of these measurement methods contributes to the development of levitation techniques and paves the way for future studies on molten core oxides.

Contents

1 Introduction 4

2 Background on levitation techniques 11
- 2.1 Overview of levitation techniques . . . 12
- 2.2 Existing measurement methods for levitation techniques . . . 16
- 2.3 Applicability of ESL in the study of nonstoichiometric molten core oxides . . . 28

3 Experimental setup 37
- 3.1 Aerodynamic levitator setup . . . 38
- 3.2 Image analysis method . . . 43
- 3.3 Temperature analysis method . . . 46

4 Heat capacity measurement (Multiple-gas cooling method) 55
- 4.1 Measurement setup . . . 56
- 4.2 Heat loss and heat capacity evaluation method . . . 57
- 4.3 Heat capacity data for various liquid transition metals . . . 66
- 4.4 Application to latent heat measurements . . . 73

5 Surface tension and viscosity measurement (Drop-bounce method) 76
- 5.1 Measurement setup . . . 78
- 5.2 Oscillation, surface tension, and viscosity evaluations . . . 94
- 5.3 Surface tension of liquid gold . . . 97
- 5.4 Surface tension and viscosity of liquid alumina . . . 99
- 5.5 On the necessity of a 'sum-rule' for surface tension measurements . . . 103

6 Density measurement (ADL-drop method) 108
- 6.1 Measurement setup . . . 109
- 6.2 Results and discussion . . . 110

7 Conclusion 116

Appendix A Comprising papers 119

Appendix B Liquid metals' cooling curves used in heat capacity measurements 121

Appendix C Values of the thermophysical properties used in heat capacity calculations 130

Appendix D The l=2, 3 spherical harmonics 132

References 150

Listing of figures

1.1 Shadowgraphs of an molten sample levitated with ADL and a solidified deformed sample. . . . 10

2.1 Schematic of the charging electrodes for ESL . . . 13
2.2 Schematic of the levitation coils for EML [1] . . . 14
2.3 Schematic of a levitation nozzle for ADL . . . 15
2.4 Simplified 3D model of the ADL setup used in this work . . . 16
2.5 Image of the l=2 m=0 oscillation. . . . 18
2.6 Schematic of a levitation drop calorimeter. . . . 23
2.7 A Zr-O sample cooled using ESL . . . 25
2.8 Images of the ESL used in this study and inside the ESL chamber. . . . 30
2.9 Zirconium oxygen binary phase diagram. . . . 32
2.10 $Zr_{1-x}O_x$ sample's composition after density measurement or oscillating drop experiment. . . . 34
2.11 Density of liquid $Zr_{1-x}O_x$ samples . . . 35
2.12 Surface tension of liquid $Zr_{1-x}O_x$ samples . . . 36
2.13 Viscosity of liquid $Zr_{1-x}O_x$ samples . . . 36

3.1 ADL setup (fiber laser) used in this work. . . . 38
3.2 ADL setup (CO_2 laser) used in this work. . . . 39
3.3 Levitation chamber used in this work. . . . 39
3.4 3D renderings of the nozzles used in this work. . . . 40
3.5 Schematic of the shadowgraph setup. . . . 44
3.6 Bandpass filter's effect on a blackbody's radiance at different temperatures. . . . 44
3.7 Images taken with different light sources and filters. Sample's temperature decreases from left to right. . . . 45
3.8 Shadowgraph image processing with DIPP-MACRO II. . . . 46
3.9 Front view of the l=2 zonal harmonics with different amplitudes and their deviations from an ellipse. . . . 47
3.10 Cooling curve of a liquid platinum sample. . . . 48

3.11 A comparison between the as-obtained and corrected cooling curves of a liquid platinum sample cooled under Ar gas. 50
3.12 Free-falling sample's temperature estimation. 52
3.13 The end portion of a liquid platinum sample's cooling curve. 53
3.14 Shadowgraphs of a free-falling liquid platinum sample as the nozzle splits open. . . 53
3.15 Schematic showing the method for calculating sample's speed which is used to obtain the time it spent in free-fall. 54

4.1 A molten sample levitated with ADL. 57
4.2 α coefficient under argon flow 63
4.3 Experiment cooling curve of liquid platinum, fitted using $\alpha = 0.751$ and $\alpha = 1$. . . 63
4.4 α coefficient under krypton flow 64
4.5 Heat capacity as a function of emissivity for a liquid platinum sample. 65
4.6 Flow diagram of the heat capacity measurement process. 68
4.7 Platinum sample with different undercooling. 75
4.8 Relationship between time of thermal arrest and undercooling temperature. . . . 75

5.1 The closed and open configurations of the splittable nozzle. 79
5.2 Cooling curves of liquid platinum samples cooled using a single top laser and two top-bottom lasers in argon gas. Temperature differences on the right side are expressed as $T_{double} - T_{single}$. 81
5.3 The Magnus effect simulated with COMSOL Multiphysics using a 2D laminar flow model. 83
5.4 Timelapse images of a bouncing liquid gold sample 84
5.5 A comparison between the sample's maximum deformation and the first few zonal harmonics l = 2, 3, 4. 85
5.6 Gold sample's position along the vertical direction. 86
5.7 Sample oscillating (l=2 m=0) without rotation. 87
5.8 Vertical (up) and horizontal (down) oscillation patterns. 88
5.9 Sample oscillating (l=2 m=0) while rotating along the x-axis. 89
5.10 Vertical (up) and horizontal (down) oscillation patterns. 90
5.11 Sample oscillating (l=2 m=0) while rotating along the y-axis. 91
5.12 Sample oscillating (l=2 m=0) while rotating along the z-axis. 92
5.13 Vertical (up) and horizontal (down) oscillation patterns. 93
5.14 Vertical and horizontal oscillation of a liquid gold (upper) and a liquid Al_2O_3 sample (lower). 95
5.15 Frequency spectrum with Lorentzian peak fitting 96
5.16 Oscillation pattern of a sample moving towards the camera. 97
5.17 Oscillation pattern of a sample moving towards the camera, corrected, then fit with a damped sine curve. 97
5.18 Surface tension of liquid gold. 98

5.19 Timelapse images of an oscillating liquid Al_2O_3 sample. 101
5.20 Damped oscillation of a liquid Al_2O_3 sample along its horizontal axis. 101
5.21 Surface tension of liquid Al_2O_3 102
5.22 Viscosity of liquid Al_2O_3 102
5.23 Freely-oscillating droplet, CFD simulation 105
5.24 Drop-bounce, CFD simulation 105
5.25 Oscillation along the x, y, and z-axis. 106

6.1 Sample's perimeter fitting using different numbers of edge points. From left to right: 360, 120, 36, 12, 6. 110
6.2 Relationship between the measured pixels and the sample's actual diameter 112
6.3 Simulated pressure field around a levitated sample within a conical nozzle 113
6.4 Image of a falling liquid platinum sample during density measurement. 114
6.5 Liquid platinum's density obtained in this study and reference values. 114

B.1 Cooling curves of liquid Au. 122
B.2 Cooling curves of liquid Cu. 122
B.3 Cooling curves of liquid Fe. 123
B.4 Cooling curves of liquid Ni. 123
B.5 Cooling curves of liquid Pd. 124
B.6 Cooling curves of liquid Pt. 124
B.7 Cooling curves of liquid Co. 125
B.8 Cooling curves of liquid Hf. 125
B.9 Cooling curves of liquid Ir. 126
B.10 Cooling curves of liquid Mo. 126
B.11 Cooling curves of liquid Nb. 127
B.12 Cooling curves of liquid Rh. 127
B.13 Cooling curves of liquid Ru. 128
B.14 Cooling curves of liquid Ti. 128
B.15 Cooling curves of liquid V. 129
B.16 Cooling curves of liquid Zr. 129

D.1 Front view, l=2 m=0 mode. 133
D.2 Top view, l=2 m=0 mode. 133
D.3 Front view, l=2 m=$\pm$1 mode. 134
D.4 Top view, l=2 m=$\pm$1 mode. 134
D.5 Front view, l=2 m=$\pm$2 mode. 135
D.6 Top view, l=2 m=$\pm$2 mode. 135
D.7 Front view, l=3 m=0 mode. 136
D.8 Front view, l=3 m=$\pm$1 mode. 136
D.9 Front view, l=3 m=$\pm$2 mode. 137

D.10 Front view, l=3 m=±3 mode. 137

List of Tables

1.1 Comparison between the main features of ChNPP-4, TMI-2, and 1F 5

2.1 System specifications of the ESL setup 31
2.2 Compositions of the $Zr_{1-x}O_x$ samples during the entire experiment. 33

3.1 Specifications of the lasers and pyrometers. 42
3.2 Various laser filters installed on the levitation chamber. 42
3.3 Specifications of the pyrometers. 42
3.4 Specifications of the components used for shadowgraph imaging. 45

4.1 Thermophysical properties of liquid platinum[2,3]. 62
4.2 List of chemicals used in this study. 67
4.3 Thermophysical properties of Ar and Kr gases at room temperature[4] 67
4.4 Heat capacity of liquid transition metals obtained in this work. 69
4.5 The undercooling limit and latent heat of liquid platinum 74

5.1 Parameters used in the CFD simulation. 104
5.2 Simulated pseudo-Al_2O_3 droplet's resonant frequency ν_R (Hz), surface tension σ (N·m^{-1}), and viscosity η (Pa·s). 105

6.1 Elliptical fitting results with different numbers of edge points of the same stainless steel sample. 110
6.2 Liquid platinum's density at the melting point and its temperature coefficient obtained in this study with reference values. 114

C.1 Densities of the pure elements used in this study. 131

Dedicated to the staff and students at Osaka University.

Acknowledgments

This research would not be possible without the guidance and support from my supervisor, Assoc. Prof. Ohishi, who introduced me to the study of levitation techniques. He designed and built the aerodynamic levitator at Osaka University, and the result from this work is the product of our endless discussions. I also want to thank co-examiners Prof. Kurosaki, Prof. Murata, and Prof. Nakagawa for supervising and offering advice to my dissertation.

My most sincere thanks to all members of the Muta laboratory: Prof. Yamanaka, Prof. Muta, Assoc. Prof. Fujieda, secretaries M. Kashi, S. Furutani, and fellow graduate students, especially Dr. Kondo, K. Kurokawa, T. Takatani, N. Gouda, and S. Kitagawa, for their work on levitation techniques.

In the field of levitation, I would like to thank Prof. Ishikawa from JAXA, Prof. Brillo from DLR, and Dr. Kondo from JAEA for their constructive criticism of my work. In the field of computational fluid dynamics simulations, I would like to thank Assoc. Prof. Yamaji of Waseda University and Assist. Prof. Duan of the University of Tokyo for their contribution to the CFD simulation of liquid alumina.

I was able to focus on my research thanks to the Research Fellowship for Young Scientists awarded by the Japan Society for the Promotion of Science during the 2020-2022 fiscal years and the Research Assistant positions offered by Osaka University.

Finally, I would like to thank my parents for supporting and encouraging me throughout my time in Japan. I give my thanks to my friends Dr. Yu, Dr. Gao, K. Nam, C. Chang, and A. Senpai, who were always there for me and reminded me to always strive for more extraordinary achievements.

Nomenclature

Abbreviations

1F	Fukushima Daiichi Nuclear Power Plant
ADL	Aerodynamic levitation
BWR	Boiling Water Reactor
CFD	Computational Fluid Dynamics
ChNPP-4	Chernobyl Nuclear Power Plant Unit 4
DLR	German Aerospace Center
ELF	Electrostatic levitation furnace
EML	Electromagnetic levitation
ESL	Electrostatic levitation
FFT	Fast Fourier Transformation
ISS	International Space Station
JAXA	Japanese Aerospace Exploration Agency
LFCMs	Lava-like Fuel-containing Materials
LOCA	Loss-of-coolant accident
MCCI	Molten core concrete interaction
PWR	Pressurized Water Reactor
RBMK	Reaktor Bolshoy Moshchnosty Kanalny
RPV	Reactor Pressure Vessel

TMI-2 Three Mile Island - Unit 2

Physics constants

ε_0	Vacuum permittivity, 8.85×10^{-12} F m^{-1}
σ	Stefan-Boltzmann constant, 5.67×10^{-8} W m^{-2} K^{-4}
c	Speed of light in vacuum, 3.00×10^{8} m s^{-1}
g	Gravitational acceleration, 9.80 m s^{-2}
h	Planck constant, 6.63×10^{-34} m^2 kg s^{-1}
k_B	Boltzmann constant, 1.38×10^{-23} m^2 kg s^{-2} K^{-1}
R	Gas constant, 8.31 J mol^{-1} K^{-1}

Variables, common units

ε	Emissivity, dimensionless
η	Viscosity, kg m^{-1} s^{-1}
Γ	Damping constant, dimensionless
γ	Surface tension, N m^{-1}
κ	Thermal conductivity, W m^{-1} K^{-1}
ν, ν_R	Frequency, resonant frequency, Hz
Ω	Rotation frequency, Hz
ρ	Density, kg m^{-3}
A	Surface area, m^2
B	Magnetic field flux, T
C_d	Drag coefficient, dimensionless
C_p	Heat capacity, J K^{-1}
E	Electric field, V m^{-1}
E	Energy, J

h	Heat transfer coefficient, W m^{-2} K^{-1}
l, m	Oscillation mode
M	Molar mass, kg mol^{-1}
m	Mass, kg
Nu	Nusselt number, dimensionless
Pr	Prandtl number, dimensionless
Q	Electric charge, C
Q	Heat transfer rate, W
q	Heat flux, W m^{-2}
r, d	Radius, diameter, m
Re	Reynolds number, dimensionless
V	Volume, m^3

1

Introduction

Overview of the Fukushima Nuclear Power Plant Accident

During the Fukushima nuclear power plant (1F) accident in 2011, the power plant's automatic emergency shutdown program was triggered by the initial 9.1 magnitude earthquake at 14:46, and the reactor is being slowly cooled. However, shortly after, the Tsunami following the

earthquake caused a blackout at the power plant, disabling the backup diesel generators and most of the emergency core cooling system. The nuclear reactor still generates decay heat even after shut down, and without sufficient cooling water, core meltdowns occurred in Units 1, 2, and 3. Details on the accident's progression have been extensively reported[5–7]. As temperature increases, reactions among the UO_2 fuel pellets, the zircaloy fuel cladding, boron carbide control rods, stainless steel components, and steam formed the molten corium that eventually deposited onto the concrete pedestal. Reactions between the corium and the concrete pedestal (mainly SiO_2 and CaO) can lead to the formation of MCCI products. The solidified molten core materials and the MCCI products are part of the generated fuel debris, and their removal from the reactor is required for decommissioning.

	ChNPP-4	TMI-2	1F*
Reactor	Soviet RBMK	PWR	BWR
Fuel	UO_2	UO_2	UO_2
Moderator	Graphite	Water	Water
Coolant	Water	Water	Water
Control material	B_4C	Ag-In-Cd	B_4C
MCCI	✓	-	✓

Table 1.1: Comparison between the main features of ChNPP-4, TMI-2, and 1F

Past studies on the ChNPP-4 and TMI-2 accidents provide valuable information on understanding the progress of the core meltdown and the characteristics of the fuel debris at 1F for its decommissioning. A comparison among ChNPP-4, TMI-2, and 1F is shown in Tab.1.1 to highlight the main features of each power plant. Unlike ChNPP-4, the RPV was not breached during the TMI-2 meltdown. Therefore, the debris-related reports on TMI-2 can be used in estimating the characteristics of any fuel debris left within the RPV at 1F. The TMI-2 accident's progression and distribution of the fuel debris within the reactor vessel were reported by Akers et al.[8] and Broughton et al.[9], re-

*Sea-water injected into the core for cooling after the accident

spectively. Analysis of the fuel debris samples taken from the lower plenum of TMI-2 showed that they were made up of mostly $(U,Zr)O_2$ [10]. On the other hand, because MCCI only occurred in ChNPP-4, data on the composition and properties of the LFCMs [11–14] from ChNPP-4 provide critical knowledge on the MCCI at 1F. Burakov et al. [15] provided a good summary on the possible components of the LFCMs: UO_x with Zr, $(U,Zr)_xO_{1-x}$, ZrO_2 with U, Chernobylite (high-uranium zirconium silicate), and uranium containing glass.

Over the years, the properties of fuel debris related materials have been thoroughly investigated [16–21], and the Muta Laboratory in Osaka University has contributed greatly to understanding the thermophysical and mechanical properties of various metal borides and oxides found in simulant fuel debris [22–27]. However, because the reactors' designs, structure materials' components, as well as the accident progression are all different in the past three nuclear power plant accidents, it is essential to understand the meltdown progression and fuel debris specifically for 1F. For example, a comparison given by F. Tanabe [28] showed that 1F contains a higher amount of metals such as Zr and Fe, which could lead to the formation of fuel debris not observed in TMI-2. Therefore, simulant fuel debris should be fabricated under conditions closest to that in 1F to better estimate the actual fuel debris' compositions.

Experiments and simulations of molten core materials at 1F

Large-scale molten corium spreading experiments, simulating MCCI accidents, have been performed at the VULCANO facility in France over the years. Prior to the VULCANO VF-U1 test in 2017, the conditions of the VBS-U4 test best resembled that of the Fukushima Daiichi. Using samples from the VBS-U4 test, Kitagaki et al. [21] reported the phase states, density, porosity, and hardness of the simulant MCCI products. In addition, they also investigated the quenching effect of cooling water on the MCCI products using samples from the VULCANO VW-U1 experiment [29].

Thermodynamic calculations using the cooling rates based on the VULCANO VE-U1 experiment suggested the majority of Fukushima Daiichi MCCI products are $(U,Zr)O_2$ or $(Zr,U)SiO_4$, along with calcium and silicon oxides[30]. Most recently, the VULCANO Fukushima VF-U1 test performed in 2017 used simulant corium and concrete whose compositions were estimated based on the materials used in Fukushima Daiichi. Details on the microstructure and phase distributions within several samples from the VULCANO VF-U1 test were given by Brissonneau et al.[31]

Although experiments such as the ones performed at the VULCANO facilities provide us with valuable information on fuel debris that could have formed at 1F, it is difficult to evaluate how well these studies represent the actual condition within the reactor core. It is both dangerous and practically impossible to replicate severe accidents with experiments. Therefore, computational method is an indispensable alternative route to study the progression of the core meltdown at 1F. In computational studies, the following mass, momentum, and energy conservation equations are commonly applied[32,33]:

$$\frac{1}{\rho}\frac{D\rho}{Dt} = 0 \tag{1.1}$$

$$\frac{Du}{Dt} = -\frac{1}{\rho}\nabla P + \frac{\mu}{\rho}\nabla^2 u + g \tag{1.2}$$

$$\rho C_p \frac{DT}{dt} = \kappa \nabla^2 T + Q \tag{1.3}$$

Here, ρ is density, u is velocity, P is pressure, μ is viscosity, g is gravity, C_p is heat capacity, κ is thermal conductivity, T is temperature, and Q is the heat source. Additional models, with extra variables, are used to describe the heat transfer between the solid and liquid phase, liquid solidification, as well as the movement of the viscous liquid. For example, the phase transition model requires the temperatures and enthalpy of the interacting solid and liquid[34]. Therefore, not only simulation models but also the thermophysical properties of the molten core materials, such as density, heat

capacity, surface tension, and viscosity, are important as they are necessary for accurately simulating the corium's flow within the reactor as well as during MCCI. However, because of the limited use of molten core materials such as metal borides, UO_2, and ZrO_2 outside the field of nuclear engineering, reports on the properties of these materials are limited. Therefore, in most CFD simulations, researchers can only assume generic properties for the molten core materials[35,36]. This lack of information on molten core materials is also due to their high melting temperatures, making measurements using conventional contact methods extremely challenging. For liquid ZrO_2, one of the major corium components, its thermophysical properties such as density, heat capacity, surface tension, and viscosity have never been reported using contact methods. Another concern for contact methods is that, at temperatures approaching 3000 K, sample-container reactions can significantly affect the reliability of the measured result. For example, the heat capacity of liquid UO_2 reported by Ronchi et al.[37] from 3150 to 5000 K contains an uncertainty of 15-20%. In another example, the viscosity of liquid UO_2 reported by Tsai & Olander[38] is roughly twice higher than that reported by R. E. Woodley[39] using the same oscillating cup viscometer method. R. E. Woodley attributed this large deviation between the results of the two studies to possible tungsten-contamination in the liquid UO_2 samples[39].

Aerodynamic Levitation to measure the properties of molten corium

Levitation techniques use electrostatic, electromagnetic, or aerodynamic forces to create a containerless environment, eliminating the primary source of sample contamination. Although these techniques have been around for more than half a century, tremendous growth took place over the past twenty years with better imaging techniques and the ability to perform experiments on the ISS. Depending on how levitation is induced, these methods are used to levitate different materials. The high-vacuum condition of ESL and EML works well with liquid metals, and the ability to use

oxygen-mixture levitation gas makes ADL the best choice for studying molten oxides. After the 1F accident, researchers noticed ADL's potential in studying molten nuclear materials because it can stably levitate oxides past 3000 K. For example, Alderman et al. and Weber et al.[40,41] performed *in-situ* structural analysis using ADL on molten UO_2-ZrO_2 systems. The structures of molten UO_2 under normal and reducing atmospheres have also been reported by Skinner et al.[42] and Alderman et al.[43], respectively. Aside from these structural analyses, ADL has been rarely used to report the thermophysical properties of molten core oxides[44,45]. This is because although ADL can stably levitate molten oxides, few reliable thermophysical properties measurement methods can be used with ADL. ADL's sluggish development is understandable because of its less controlled environment (non-vacuum) and the difficulty in analyzing the interaction between the sample and the levitation gas.

To the best of my knowledge, although researchers have attempted density, heat capacity, and surface tension measurements with ADL, they have made questionable assumptions during their analysis. For ADL, the sample is levitated within a nozzle and is not fully visible to the observation camera, as shown in Fig.1.1. To obtain the sample's density, past researchers generally assumed the sample is an ellipsoid and fit the contour of the sample with an ellipse (or a circle)[46–48]. However, as the bottom part is not visible, this assumption inevitably introduces unexplained uncertainty in the calculated sample volume. A recent simulation on molten Al_2O_3 by Borgard et al.[49] from CEA using COMSOL showed that the bottom of the sample could be deformed by the levitation gas. In this case, the sample's volume can no longer be calculated by applying an elliptical fitting.

To accurately describe the heat loss of a sample levitated with ADL, one needs a heat loss model containing both radiative and convective heat loss. Furthermore, the sample's total hemispherical emissivity and the convective heat transfer coefficient are required to calculate the radiative and convective heat loss term, respectively. The only previous attempt was by Millot et al.[50] to measure the heat capacity of liquid boron. However, they assumed negligible convective heat loss took place

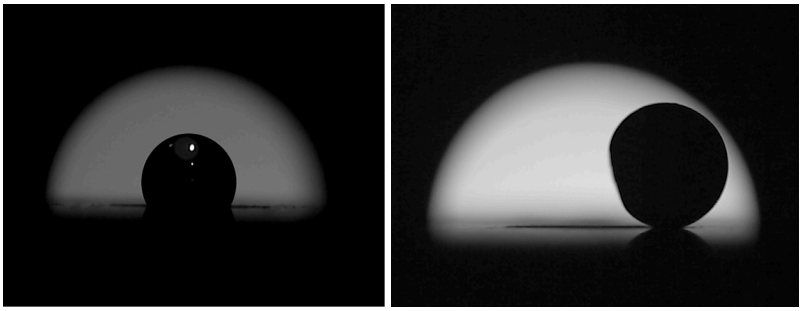

Figure 1.1: Shadowgraphs of an molten sample levitated with ADL and a solidified deformed sample.

during the sample's cooling process, which is clearly incorrect. Unfortunately, twenty years have passed since Millot et al.'s attempt, and a comprehensive heat loss model for ADL is still unavailable.

Finally, when using the oscillating drop method to evaluate the sample's surface tension with ADL, it is generally assumed that Rayleigh's equation [51] can be used directly in the calculation. However, Rayleigh's equation for surface tension calculation is derived for a force-free (perfectly spherical, not rotating) sample, which can only be achieved under microgravity conditions. The influence of the sample's rotation and deformation on its oscillation resonant frequency (specifically the l=2 mode) has been clarified for ESL and EML, but not ADL. Therefore, the reliability of using only the l=2 m=0 mode's frequency in surface tension calculation is unclear.

Although ADL is the most suitable levitation technique for molten oxides, it can currently only be reliably used in viscosity measurements. Thus, the motivation of this study is to design new and accurate measurement methods that can be used with ADL to study the thermophysical properties of molten core materials. Among the various thermophysical properties, this study specifically focuses on density, heat capacity, surface tension, as well as viscosity that can have a direct impact on improving the accuracy of CFD simulations for 1F's decommissioning. Although thermal conductivity is also one of the most important variables in simulating heat transport, designing a laser modulation system for ADL is out of the scope of this dissertation. However, the integration of a laser modulation system to ADL is planned for future works.

2

Background on levitation techniques

This chapter first briefly gives an overview of the three commonly used levitation techniques: electrostatic, electromagnetic, and aerodynamic levitation. I will cover the basic operating principles and the application of these levitation techniques. Then, I will provide a literature review of the measurement methods used with levitation techniques. The measurement methods cover thermophysical properties such as density, surface tension, viscosity, heat capacity, and latent heat.

Although this work focuses on studying the thermophysical properties of molten oxides, it is common for core oxides to be nonstoichiometric, for example zirconium oxidized under a slightly reducing atmosphere. While ADL is the default levitation technique for molten oxides, it could also cause nonstoichiometric oxides to become 'completely oxidized.' Among ESL, EML, and ADL, ESL is the only other levitation technique that can theoretically levitate metal oxides. Because of its high vacuum condition, it is possible that nonstoichiometric oxides can keep their original compositions. Therefore, at the end of this chapter, I will discuss ESL's potential in the study of molten core materials using zirconium oxides $Zr_{1-x}O_x$.

2.1 Overview of levitation techniques

2.1.1 Electrostatic levitation

As its name suggests, ESL utilizes the electrostatic interaction to levitate the sample. Two parallel disks electrodes placed within a high-vacuum chamber are used for sample charging. The top electrode is negatively charged, and the bottom electrode is grounded, which induces positive charges on the sample. Additional charging methods by removing electrons from the sample include UV light charging and thermionic emission charging[52]. While the top and bottom electrodes control the sample's vertical position, four side electrodes are positioned around the bottom electrode to control the sample's position in the xy-plane. A simple schematic of the electrodes within the ESL chamber is shown in Fig.2.1. After sample levitation, lasers are used to heat the sample.

Levitation with ESL is inherently unstable because a stable equilibrium position cannot be created from only the interaction of point charges (Earnshaw's theorem). Therefore, the sample's position is constantly monitored with a He-Ne laser, and a feedback system adjusts the voltage of the top and side electrodes. During the experiment, the sample is rotated along the z-axis by a rotating magnetic field to suppress unwanted oscillations and maintain temperature homogeneity.

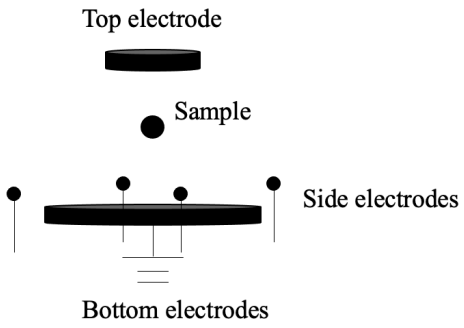

Figure 2.1: Schematic of the charging electrodes for ESL

The shape of a sample levitated with ESL on the ground closely resembles that of a perfect sphere because of the near-uniform distribution of electrostatic charges on the liquid sample's surface. The sample is also processed under a high vacuum where the heat loss is purely radiative, and sample-container contamination can be avoided. All of these features make ESL suitable to measure a wide range of thermophysical properties such as density, surface tension, viscosity, heat capacity, etc [53,54]. So far, the aforementioned ESL experiments are focused on metals because oxides are much harder to charge. Currently, attempts to levitate molten oxides with the electrostatic levitator onboard the ISS (ELF-ISS) is underway [55,56].

2.1.2 Electromagnetic levitation

EML levitates electrical-conducting samples through the Lorentz force generated by the eddy currents. The eddy currents are induced by the alternating currents within the levitation coils. In addition, the eddy currents will also contribute to heating the sample due to resistance heating, which means sample levitation and heating cannot be completely separated in EML. Therefore, the sample needs to be cooled with inert cooling gas like hydrogen mixed helium to reach the target temperature. A simple schematic showing the sample's position within the levitation coils is given in Fig.2.2.

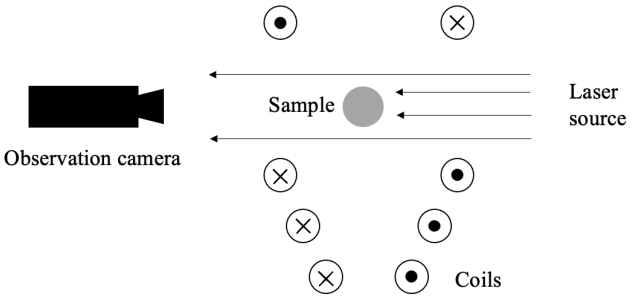

Figure 2.2: Schematic of the levitation coils for EML [1]

For a spherical sample, the necessary Lorentz force for levitation along the vertical direction is given in Eqn.2.1. Compared to the electrostatic force of ESL, the Lorentz force used in EML do provide an equilibrium position for the sample.

$$\rho\vec{g} \propto -\frac{\nabla_z \vec{B}^2}{2\mu_0} \tag{2.1}$$

or

$$\rho\vec{g}dV \propto -\frac{\nabla_z \vec{B}^2}{2\mu_0}\pi R^2 dz \tag{2.2}$$

From Eqn.2.2, it is obvious that the middle section of the sample (with a larger R^2dz) mainly contributes to generating the upward levitation force. Therefore, samples levitated with ground-based EML are deformed, with a round top and a hanging bottom.

Currently, ground-based EML cannot be used to measure the viscosity of liquid metals because of the additional magnetic pressure and induced turbulent flow within the sample [1]. These problems can be solved by conducting EML under microgravity conditions, where levitation can be achieved with much weaker forces. Microgravity conditions have been achieved with the use of

parabolic flights, sounding rockets, and space shuttle missions[57]. Since 2014, EML experiments have been conducted on board the ISS in the study of liquid metals[58–61].

2.1.3 Aerodynamic levitation

For ADL, the sample is levitated in a converging-diverging nozzle with levitation gas supplied from the bottom. The sample's weight is balanced by the buoyancy and drag forces. Because of the levitation nozzle, part of the sample's bottom cannot be seen during the experiment, and contour fitting is necessary. Similar to other levitation techniques, ADL uses lasers to heat and melt the levitated samples. Compared to EML and ESL, ADL can levitate both metals and oxides under normal gravity. However, EML and ESL operate under vacuum conditions and are preferred when dealing with liquid metals. ADL then has a niche of working with metal oxides because an argon-oxygen mixture gas can be used to prevent sample reduction at high temperatures. ADL also shines when handling materials with high vapor pressures that will evaporate easily under high vacuum. Aside from thermophysical property measurements[44,48,62], ADL is frequently used with X-ray diffraction to study the structure of molten oxides[42,63,64].

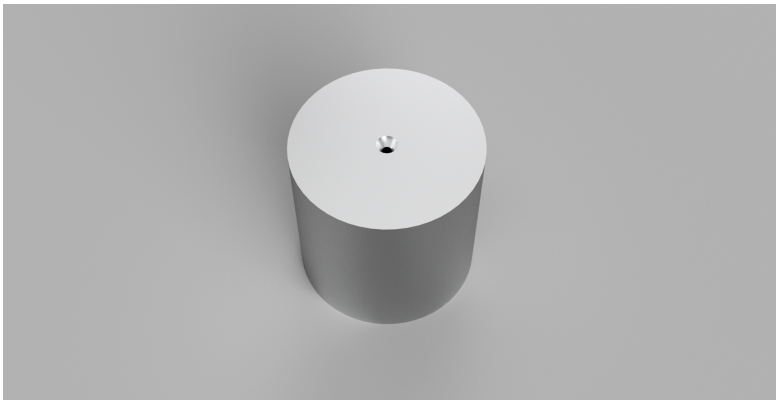

Figure 2.3: Schematic of a levitation nozzle for ADL

Since this study deals extensively with ADL, a simplified 3D rendering of the ADL setup used is

shown in Fig.2.4.

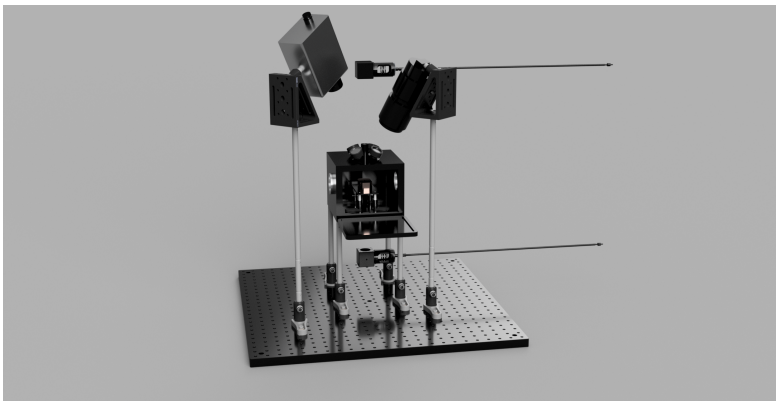

Figure 2.4: Simplified 3D model of the ADL setup used in this work

2.2 Existing measurement methods for levitation techniques

2.2.1 Density

Density measurement is very straightforward if accurate information on the sample's volume can be obtained. To observe the sample at high temperatures, the shadowgraph imaging technique, where the sample's shadow is measured against a white background, is commonly used. Details on the shadowgraph imaging technique will be discussed in section.3.2.

For ESL and EML, an unobstructed view of the sample is available. The distance from the center of mass of the sample to its contour, $R(\theta)$, is expressed as a linear combination of the first few Legendre polynomials $P_n(cos\theta)$ with fitting parameters α_n:

$$R(\theta) = \sum_{n=0}^{5,6} \alpha_n P_n(cos\theta) \tag{2.3}$$

The sample is assumed to be axisymmetric along the z-axis, and the volume of the sample can be expressed as the integral of the elemental volume units $R(\theta)d\theta \times dR \times R(\theta)sin\theta d\varphi$:

$$V = \int_0^{2\pi} \int_0^{\pi} \int_0^{R(\theta)} \{R(\theta)\}^2 dR sin\theta d\theta d\varphi \tag{2.4}$$

This axisymmetric assumption holds for ESL, EML, and ADL. For ADL, because the sample is larger than the orifice of the nozzle, the pressure of the levitation gas will deform the sample into something like an oblate spheroid. Since only the top part of the sample is visible to the camera, the sample's contour must be fitted to an ellipse. The volume of an oblate spheroid can be expressed with its semi-major, a, and semi-minor axis, c:

$$V = \frac{4\pi}{3} a^2 c \tag{2.5}$$

Finally, density can be expressed with the sample's mass:

$$\rho = \frac{M}{V} \tag{2.6}$$

2.2.2 Surface tension and viscosity

For all three types of levitation techniques, the oscillating drop method[65] is commonly used to evaluate the surface tension and viscosity of levitated materials. Strong internal flow is induced in a sample levitated with EML, so surface oscillation does not need to be artificially induced. For ESL and ADL, the sinusoidal oscillation signal is produced by a changing electrical field and gas pressure, respectively. The sample's resonant frequency can be theoretically related to its surface tension and viscosity using Rayleigh's[51] and Lamb's[66] equations, respectively.

$$\gamma = \frac{1}{l(l+2)(l-1)} \frac{3\nu_R^2 M}{4\pi} \tag{2.7}$$

$$\eta = \frac{1}{l(l+2)(l-1)} \frac{3M\Gamma}{4\pi R} \tag{2.8}$$

For ESL and ADL, the l=2 m=0 oscillation mode, shown in Fig.2.5, is generally used for oscillating drop experiments because it can be easily recognized and confirmed by the naked eye. Other oscillation modes, such as the $l = 0$ mode represents sample's volume change, and the $l = 1$ mode represents sample's translational movement. In addition, $l > 2$ oscillation modes damp much faster that of $l = 2$, as can be seen from Lamb's equation. When expressed using $l = 2$, Eqns.2.7, 2.8 are conveniently written as:

$$\gamma = \frac{3\nu_R^2 M}{32\pi} \tag{2.9}$$

$$\eta = \frac{3M\Gamma}{32\pi R} \tag{2.10}$$

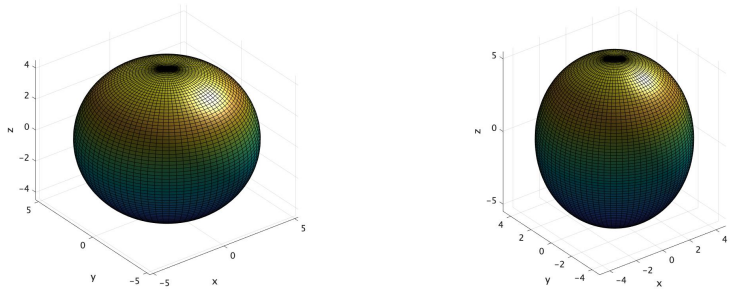

Figure 2.5: Image of the l=2 m=0 oscillation.

However, there are restrictions to both Rayleigh's equation and Lamb's equation. Rayleigh's equation was derived for an inviscid (undamped), spherical, and non-rotating sample, and Lamb's equation is for droplets that undergo weakly-damped oscillations. It is well known that the resonant frequency of a harmonic oscillator changes when it is damped, and this effect can only be assumed

to be negligible for weakly-damped oscillations ($\eta \ll \nu_R$). Therefore, one must take extra care when applying Eqn.2.9 or 2.10 for strongly-damped oscillations. Recently, calculations by Lohöfer[67] showed that while Rayleigh's equation can be applied to viscous liquids with negligible error (2% for strongly-damped oscillations), viscosity calculated using Lamb's equation can contain errors larger than 10%. Lohöfer recommended the following approximation for the l=2 oscillation:

$$\frac{1}{\eta} = \frac{20\pi R}{3M}\Gamma(1 - \sqrt{\frac{18}{125}}\frac{1}{\sqrt{\nu_R\Gamma}}) \tag{2.11}$$

In this study, the original Lamb's equation was used for viscosity calculations.

The l=2 mode can be further divided into l=2 m=0, ±1, ±2 modes, and these five modes have the same resonant frequency when freely oscillating. Images of the l=2, l=3 mode oscillations are shown in Appendix.D. This degeneracy in the resonant frequencies explains why there is only one term for the resonant frequency of the l=2 mode in Rayleigh's equation. However, the sample needs to be levitated with an external force on the ground, rotating and slightly deforming the sample. This unideal condition causes all five l=2 modes to take on different resonant frequencies from that of the original l=2 mode. Therefore, corrections to these resonant frequencies must be made before Rayleigh's equation can be used for surface tension calculations.

Correction for ESL Among the three levitation techniques, ESL can maintain a sample's shape closest to a perfect sphere because of the distribution of surface charges. In this case, frequency-splitting does not occur[68]. However, the levitated sample can never be perfectly spherical, resulting in an uneven surface charges distribution. Corrections to the charge distribution's effect on the resonant frequency of the sample are given by Feng et al.[69]:

$$\nu_R^2 = (\frac{8\gamma}{\rho R^3})(1 - \frac{Q^2}{64\pi^2 R^3\gamma\varepsilon_0})\{1 - f(\gamma, q, Y)\} \tag{2.12}$$

$$f(\gamma, q, Y) = \frac{(243.31\gamma^2 - 63.14q^2\gamma + 1.54q^4)Y^2}{176\gamma^3 - 120q^2\gamma^2 + 27\gamma q^4 - 2q^6} \tag{2.13}$$

q, γ in the correction term $f(\gamma, q, Y)$ are expressed as:

$$q^2 = \frac{Q^2}{16\pi^2 R^2 \varepsilon_0} \tag{2.14}$$

$$Y^2 = E^2 R \varepsilon_0 \tag{2.15}$$

The charge on the drop, Q, can be calculated from the force balance:

$$Q = \frac{Mg}{E} \tag{2.16}$$

During ESL experiments, the sample is forced to rotate along the z-axis to maintain temperature homogeneity and suppress other oscillation modes. The effect of sample rotation on the sample's resonant frequency and damping constant has been studied by Paradis and Ishikawa[70,71]. They experimentally confirmed that as long as the aspect ratio of the levitated sample is kept at less than 1.02, sample rotation does not affect the calculated surface tension and viscosity.

Correction for EML A sample levitated with EML is heavily deformed, and this aspherical shape results in the loss of the l=2 mode resonant frequency's degeneracy. The resonant frequencies of the l=2 m=0, ± 1, ± 2 modes are provided by Cummings and Blackburn[72]:

$$\nu_{2,0}^2 = \nu_R^2 + \nu_{tr}^2 (3.832 - 0.1714 \frac{g}{2R\nu_{tr}^2}) \tag{2.17}$$

$$\nu_{2,\pm 1}^2 = \nu_R^2 + \nu_{tr}^2 (3.775 + 0.5143 \frac{g}{2R\nu_{tr}^2}) \tag{2.18}$$

$$\nu_{2,\pm 2}^2 = \nu_R^2 + \nu_{tr}^2 (-0.9297 + 2.571 \frac{g}{2R\nu_{tr}^2}) \tag{2.19}$$

ν_{tr} is the mean translational frequency of the three directions, x, y, and z:

$$\nu_{tr} = \sqrt{\frac{1}{3}(\nu_x^2 + \nu_y^2 + \nu_z^2)} \tag{2.20}$$

According to Busse[73], sample's rotation along its axis of symmetry at a rotation frequency of Ω further splits the resonant frequency $\nu_{l,m}(0)$:

$$\nu_{l,m}(\Omega) = \nu_{l,m}(0) + \frac{m}{l}\Omega \tag{2.21}$$

For l=2 m=$\pm$1,$\pm$2, Eqn.2.21 together with Eqn.2.17-2.19, finally give the resonant frequencies of the five resonant peaks observed for a sample levitated with EML under normal gravity conditions. An overall shift to higher frequencies is observed in the split peaks (l=2 m=0, $\pm$1, $\pm$2) because of the influence of the added electromagnetic field in the Navier-Stokes equation[70].

Cummings and Blackburn[72] further provided a sum-rule for EML that allows one to calculate the sample's degenerate l=2 resonant frequency based on that of the five split peaks. Therefore, one can use Rayleigh's equation in ground-based EML surface tension measurements. Egry et al.[74] performed oscillating drop experiments with EML in space and confirmed the validity of the sum-rule.

Although surface tension can be measured using EML, viscosity measurements can only take place under microgravity conditions where the required levitation force is much smaller. Under normal gravity conditions, the total damping an oscillating sample experiences is the sum of the sample's 'natural' viscosity and an additional damping term imposed by the levitation magnetic field. This additional viscosity term can be roughly expressed as[75]:

$$\eta_{mangetic} = \sigma B^2 R^2 \tag{2.22}$$

$\eta_{magnetic}/\eta \ll 1$ is required to accurately measure the sample's viscosity[76], and this condition is only fulfilled if the sample can be levitated within a much weaker levitation magnetic field (i.e. under microgravity).

Correction for ADL Currently does not exist. Therefore, only the sample's viscosity can be obtained with ADL.

2.2.3 Heat capacity

Levitation drop calorimetry

When applying the conventional drop calorimetry method for the heat of fusion or heat capacity measurements of liquids, a container is needed to hold the liquid sample. Similar to all contact methods, sample-container contamination becomes an issue at high temperatures. Various types of levitation drop calorimeter designs[77,78] have been developed over the last 50 years that use EML to heat and levitate the sample. A schematic showing the general features of a levitation drop calorimeter is shown in Fig.2.6. For ESL and ADL, it is difficult to place a calorimeter block underneath the levitated sample.

After obtaining a stable temperature signal, the sample is dropped into the calorimeter block, where a thermocouple is used to monitor its temperature change. Materials with good thermal conductivity are used as the calorimeter block to eliminate temperature gradients within the calorimeter and shorten the experiment time. The theory behind heat capacity measurement with levitation drop calorimetry is straightforward. The temperature of the calorimeter is affected by the heat received from the sample and the heat lost to an isothermal surrounding. The sample's enthalpy at a specific temperature can be obtained each run, and the heat capacity C_p is the slope of the enthalpy-temperature plot, dH/dT.

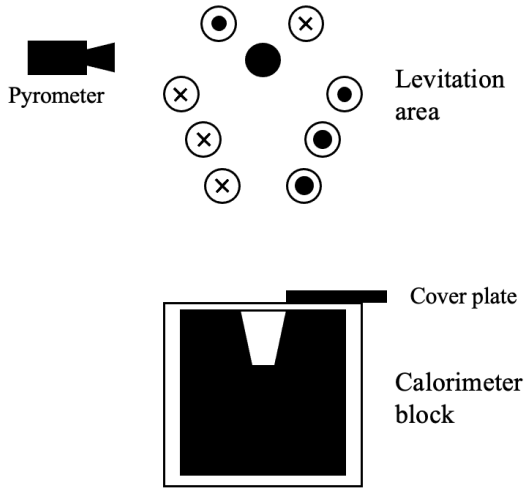

Figure 2.6: Schematic of a levitation drop calorimeter.

Modulation calorimetry with EML

A modulation calorimetry method for heat capacity measurement with EML was developed by Wunderlich et al.[79] for microgravity experiments. During the modulation process, only heat radiation (external) and conduction (internal) are considered. Ground-based EML cannot meet these criteria because a strong electromagnetic field is needed to counteract gravity, inducing strong internal flow within the sample. The output power of the heating coil used is modulated with a sinusoidal current $I = I_0 + I_m(sin\omega t)$. The sample's heat capacity, C_p, is related to the modulation frequency ω, the amplitude of the modulated temperature, ΔT_m, and the amplitude of the modulation heating power, $P_m \propto I_m^2$.

$$C_p = f(\omega, \tau_{rad}, \tau_{cond}) \frac{P_m}{\Delta T_m \omega} \tag{2.23}$$

Under adiabatic condition, where the relaxation time of the radiative heat loss (τ_{rad}) is much longer than that of the sample's internal conduction (τ_{cond}), the correction term $f(\omega, \tau_{rad}, \tau_{cond})$ is approximately equal to one.

For ground-based EML experiments, Fukuyama et al.[80] introduced the laser modulation calorimetry method, with an additional static magnetic field to suppress convection within the sample. A modulated laser with power $P = P_0(1 + cos\omega t)$ is used to heat the sample from the top, while the bottom of the sample is monitored with a pyrometer. The heat balance equations of the top (hot) and bottom (cold) part of the sample are expressed as follows:

$$V_{hot}C_p\frac{dT_{hot}}{dt} = Q_{hot} + \alpha S_{hot}AP_0(1 + cos\omega t) - S_{hot}A\varepsilon\sigma(T_{hot}^4 - T_\infty^4) - K_c(T_{hot} - T_{cold}) \quad (2.24)$$

$$(1 - V_{hot})C_p\frac{dT_{cold}}{dt} = Q_{cold} + (1 - S_{hot})A\varepsilon\sigma(T_{cold}^4 - T_\infty^4) + K_c(T_{hot} - T_{cold}) \quad (2.25)$$

V_{hot} and S_{hot} are the volume and surface fraction of the laser-irradiated 'hot' part. K_c is the thermal conductance from the top to the bottom part of the sample. The temperature of the hot or cold part during laser modulation can be expressed as a sum of the sample's initial temperature, T_0, the average increase in temperature because of laser irradiation, ΔT_{dc}, and the modulation part, $\Delta T_{ac}cos(\omega t - \varphi)$:

$$T = T_0 + \Delta T_{dc} + \Delta T_{ac}cos(\omega t - \varphi) \quad (2.26)$$

Under adiabatic conditions, where heat conduction within the sample is far greater than the sample's radiative heat loss, the average temperature increase $\Delta T_{ac,cold}$ of the non-irradiated 'cold' bottom part of the sample is expressed as:

$$\Delta T_{ac,cold} = \frac{\alpha S_b AP_0}{\omega C_p} f(\omega, \tau_r, \tau_c) \quad (2.27)$$

τ_r, τ_c are the relaxation times of the sample's heat radiation and conduction. The maximum value of the correction term $f(\omega, \tau_r, \tau_c), f = 1$, can be reached by carefully choosing the laser's modulation frequency, similar to the that of the modulation calorimetry method by Wunderlich et al.[79]. The sample's heat capacity can be calculated by finding $\Delta T_{ac,cold}$ using the sample's cooling curve.

Cooling curve analysis with ESL

The sample is levitated in a high vacuum with ESL, and therefore only radiative heat loss takes place during cooling. A zirconium oxide sample cooled using ESL is shown below.

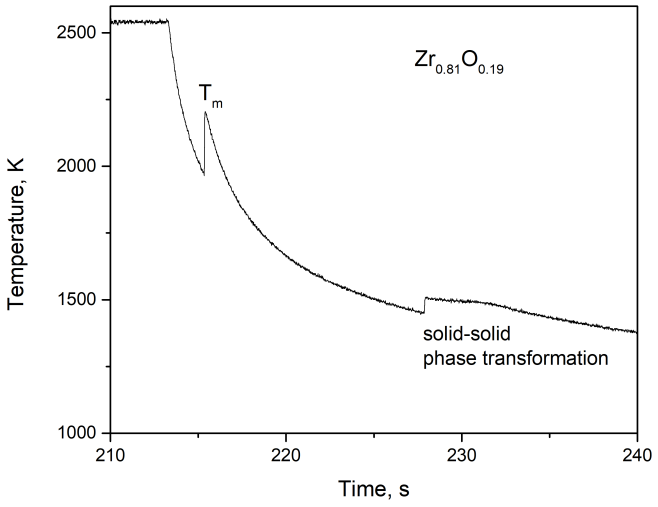

Figure 2.7: A Zr-O sample cooled using ESL

The sample's radiative heat loss, q_{rad}, can be expressed using the Stefan-Boltzmann law:

$$q_{rad} = \varepsilon(T)\sigma(T^4 - T^4_{surrounding}) \tag{2.28}$$

Further transformation of the Stefan-Boltzmann law gives:

$$\frac{dT}{dt} = \frac{A\varepsilon(T)\sigma T^4}{C_p m} \tag{2.29}$$

The sample's total hemispherical emissivity, rather than its spectral hemispherical emissivity, must be used to calculate its heat loss accurately. It is important to differentiate between the different types of emissivity because of its directional and wavelength dependence. The relationship between total hemispherical emissivity, $\varepsilon(T)$, and spectral hemispherical emissivity, $\varepsilon_\lambda(\lambda, T)$, is:

$$\varepsilon(T) = \frac{\int_0^\infty \varepsilon_\lambda(\lambda, T) I_{\lambda,black}(\lambda, T)\, d\lambda}{I_{black}(T)} \tag{2.30}$$

It should be further clarified that although spectral emissivity data for liquid metals are often available, total hemispherical emissivity data are not. A sample levitated with ESL is almost perfectly spherical, and it is reasonable to assume the sample's radiation, I, is isotropic. Therefore, the spectral emissivity is equal to the spectral hemispherical emissivity.

In the early 2000s, Paradis et al.[71,81–85] performed heat capacity measurements with ESL on numerous molten metals. However, due to the lack of emissivity data, Paradis et al. used the spectral hemispherical emissivity at 0.9μm in their calculations, which is questionable. In recent years, Ishikawa et al.[3,86–91] used a blackbody furnace, a series of pyrometers that covers the range between 0.7μm and 5.5μm, and ESL to measure the total hemispherical emissivity of liquid metals such as Pt, Ni, and Zr[3,86,87]. Due to the sample's simple heat loss behavior and the high vacuum condition, the ESL blackbody method is currently one of the more reliable emissivity and heat capacity measurements methods.

2.2.4 Latent heat of fusion

From sample's maximum undercooling

A liquid sample cooled with levitation technique experiences undercooling due to the lack of heterogeneous nucleation sites at the melting point. A schematic of the cooling curve of an undercooled α-Zr sample was already shown in Fig.2.7. During undercooling, the probability of homogeneous nucleation increases with the undercooling temperature, $\Delta T = T_m - T$, and nucleation eventually takes place above the sample's homogeneous nucleation limit. For an undercooled sample, its heat of fusion is released in two steps: during recalescence (non-equilibrium solidification) and thermal arrest (equilibrium solidification).

$$H_{fusion} = H_{noneq} + H_{eq} \tag{2.31}$$

The latent heat released during recalescence is used to heat the sample to its melting point. For ESL, it is possible to reach the sample's maximum undercooling limit ΔT_{limit}[92], and the latent heat of fusion can be expressed as:

$$H_{fusion} = H_{noneq} = C_p M \Delta T_{limit} \tag{2.32}$$

The heat capacity, C_p, is assumed to be temperature-independent and constant within ΔT_{limit}.

However, it is challenging to reach the maximum undercooling limit, and a linear relationship between the degree of undercooling, ΔT, and the time of thermal arrest, t, is roughly established to help extrapolate the maximum undercooling limit[93].

$$H_{fusion} = C_p M \Delta T + A t \sigma \varepsilon T_m^4 \tag{2.33}$$

$$C_p M \Delta T_1 + A_1 t_1 \sigma \varepsilon T_m^4 = C_p M \Delta T_2 + A_2 t_2 \sigma \varepsilon T_m^4 \tag{2.34}$$

$$C_p M(\Delta T_1 - \Delta T_2) = (A_2 t_2 - A_1 t_1)\sigma\varepsilon T_m^4 \tag{2.35}$$

Density and emissivity are assumed to be constant during thermal arrest, i.e. $A_1 = A_2 = A$, and a linear relationship can be established:

$$\frac{\Delta T_1 - \Delta T_2}{t_1 - t_2} = -\frac{A\sigma\varepsilon T_m^4}{C_p M} \tag{2.36}$$

and

$$\Delta T = -\frac{A\sigma\varepsilon T_m^4}{C_p M} t + \Delta T_{limit} \tag{2.37}$$

'Drop and catch' with ADL

For ADL, a 'drop and catch' method was introduced by Ushakov et al.[94] where a splittable nozzle was used with a constant-temperature copper calorimeter to measure the heat lost by the sample. By dropping the Al_2O_3 sample slightly higher and lower than its melting point, Ushakov et al. successfully obtained the latent heat of Al_2O_3. Although only the sample's temperature at the drop is available, this does not affect the latent heat measurements. However, this does limit the 'drop and catch' method's ability to measure the sample's heat capacity.

2.3 Applicability of ESL in the study of nonstoichiometric molten core oxides

In section2.1, I discussed the operating principles of various levitation techniques. Among ESL, EML, and ADL, only ESL and ADL are capable of levitating metal oxides with poor electrical conductivity. Unlike the majority of ADL experiments, only a handful of ESL experiments are performed on molten oxides[95–97] because of sample reduction under vacuum at high temperatures. Although oxygen mixture gases can be used in ADL, nonstoichiometric metal oxides or metal oxides

with higher oxidation states could get further oxidized. For example, Fe_3O_4 can get partially oxidized into Fe_2O_3 or UO_2 into UO_{2+x}. For these cases, levitation with ESL is theoretically possible and becomes a choice worth exploring, although it has only been used to levitate a few oxides, such as Al_2O_3, $BiTiO_3$, and $BiFeO_3$.

Although, in theory, ESL can complement ADL in the study of nonstoichiometric metal oxides, the experimental difficulty and error due to sample evaporation and reduction are unknown. Therefore, the last section of the research background chapter discusses the ESL experiments on molten zirconium oxides ($Zr_{1-x}O_x$).

2.3.1 ESL apparatus

The ESL setup used in this study was built based on the one used at JAXA with the help of T. Ishikawa. Detailed discussion on the operating principles of ESL is already given, so only the specifications of the setup used in this work are provided here. Images of the electrostatic levitator and the levitation chamber are shown in Fig.2.8.

In this work, the top and bottom disk electrodes for surface charging are approximately 10 mm apart. A stable equilibrium position does not exist for ESL, and the sample's position needs to be detected using a He-Ne laser (632nm), a bandpass filter (632±10nm), and a position detector (IVS-camera, C8201-80H, Hamamatsu). The computer constantly readjusts the voltage on the top (z-axis control) and the four side electrodes (xy-plane control) to keep the sample at the preset location for further measurements. Ishikawa et al.[98] reported that when the position feedback frequency is close to the oscillation frequency of the sample, the obtained sample's viscosity is erroneous. Based on their findings, the position feedback frequency for horizontal and vertical direction during the oscillating drop experiment (see section.2.2.2) were 240 Hz (720 Hz prior to the measurement) and 30 Hz, respectively.

The sample is heated with two fiber lasers (976 nm, Pearl), separated by 180°. The sample's tem-

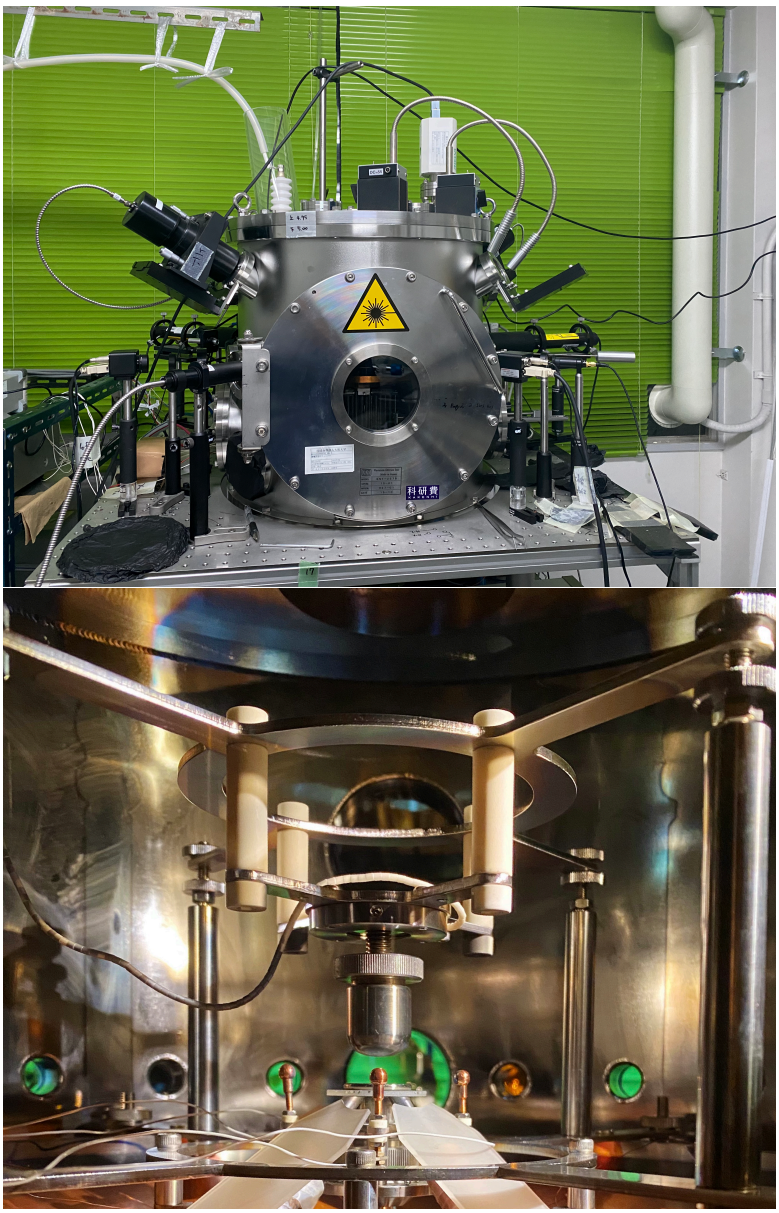

Figure 2.8: Images of the ESL used in this study and inside the ESL chamber.

perature is monitored with a pyrometer (1.55 μm, CHINO), and the as-obtained temperature signal was corrected based on the sample's recalescence and Wien's law. A detailed explanation of the temperature correction process is given in Chapter.3. A high-speed camera (HAS-LI, DITECT), bandpass filter (370 nm, Thorlabs), and ultraviolet background light (370 nm, Hamamatsu) are used to take shadowgraphs of the sample. A discussion on how to take shadowgraphs is given in section.3.2. Method for obtaining the sample's density from shadowgraphs can be found in section.2.2.1.

Apparatus	Specifications
Heating laser	976 nm fiber laser, Pearl
Positioning laser	632 nm He-Ne laser
Oscillation detection laser	532 nm semiconductor laser, Thorlabs
Pyrometer	1.55 μm, IR-CAI8CSL, CHINO
Background light	370 nm, Hamamatsu
High-speed camera	HAS-LI, DITECT

Table 2.1: System specifications of the ESL setup

The oscillating drop method is used to measure the sample's surface tension and viscosity (see section.2.2.2). A sinusoidal signal is added to the top electrode to induce sample oscillation. The desired oscillation mode can be generated by matching the signal's frequency with the sample's resonant frequency. For oscillating drop experiments, the l=2 mode oscillation is used. The sample is made to rotate along the z-axis by a rotating magnetic field, created by four coils under the bottom electrode, to reduce temperature inhomogeneity and the amplitude of unwanted oscillation modes. A vertical slit and photodetector (350 to 1100 nm, SM05PD1A, Thorlabs) are used to record the oscillation amplitude. Here, the shadowgraph technique is used again, with a semiconductor laser (532 nm, Thorlabs) acting as the background light and a bandpass filter with the corresponding wavelength (532 nm, Thorlabs).

2.3.2 Sample preparation

α-Zr, with nonstoichiometric composition $Zr_{1-x}O_x$ (x=0.1, 0.2) was chosen as the target materials based on the Zr-O binary phase diagram. Bulk $Zr_{1-x}O_x$ samples are fabricated by arc melting Zr (3N, Rare Chemical) grains and cold-pressed ZrO_2 (4N, Furuuchi) pellets. The obtained arc melting ingots ($Zr_{0.9}O_{0.1}$, $Zr_{0.8}O_{0.2}$) are annealed for 24 hours under vacuum at 1473K and 1673K, respectively. Prior to the ESL experiments, the annealed samples were crushed into smaller pieces (15 - 25 mg). Some of the samples are used in density measurements, and others in surface tension and viscosity measurements.

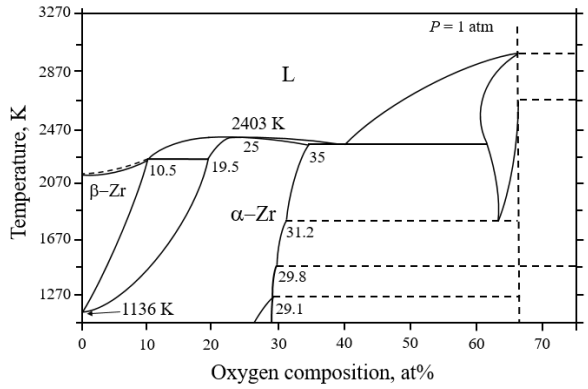

Figure 2.9: Zirconium oxygen binary phase diagram.

2.3.3 Measurement results

Before discussing the density, surface tension, and viscosity of $Zr_{1-x}O_x$, the sample's precise composition after the ESL experiment must be determined. The thermogravimetric method, where the $Zr_{1-x}O_x$ samples are completely oxidized into ZrO_2 (Eqn.2.38), is used to evaluate the sample's composition right after ESL experiments. The increase in the sample's mass with further oxidation is related to the sample's original composition. The sample's average compositions prior to ESL exper-

iments, after density measurements, and after oscillating drop experiments are listed in Tab.2.2. The oxygen concentrations of each $Zr_{1-x}O_x$ sample after the experiment are shown in Fig.2.10.

$$Zr_{1-x}O_x + \frac{2-3x}{2}O_2 \rightarrow (1-x)ZrO_2 \tag{2.38}$$

Nominal	Pre-ESL	Post-density	Post-oscillating drop	Oxygen loss, %
$Zr_{0.9}O_{0.1}$	$Zr_{0.91}O_{0.09}$	$Zr_{0.9}O_{0.1}$	$Zr_{0.93}O_{0.07}$	30%
$Zr_{0.8}O_{0.2}$	$Zr_{0.81}O_{0.19}$	$Zr_{0.8}O_{0.2}$	$Zr_{0.85}O_{0.15}$	25%

Table 2.2: Compositions of the $Zr_{1-x}O_x$ samples during the entire experiment.

Based on Tab.2.2, sample reduction after density measurement is almost negligible. However, oscillating drop experiments take a much longer time, so sample reduction is much more obvious. **Although, as expected, ESL can levitate and prevent the further oxidation of nonstoichiometric metal oxides, sample reduction limits the applicability of ESL to nonstoichiometric oxides at lower oxygen concentrations.**

As mentioned above, sample reduction is negligible during density measurements. On the other hand, if the sample's composition change is larger than 15% during the experiment, the corresponding oscillating drop measurement data is discarded. In addition, the samples are no longer addressed using their nominal compositions but their average compositions before levitation experiments. The obtained density, surface tension, and viscosity of liquid $Zr_{0.91}O_{0.09}$ and $Zr_{0.81}O_{0.19}$ samples are shown in Figs.2.11 to 2.13. The experiments were carried out at temperatures just slightly above the sample's melting point to minimize sample evaporation and reduction.

One might quickly notice the difference in the number of data points in Figs.2.11 and 2.12. Density measurements with ESL occur while the sample is cooled, so the temperature dependence of the sample's density can be directly obtained. However, oscillating drop experiments require the sample to reach thermal equilibrium before moving to a different temperature. Therefore, compared

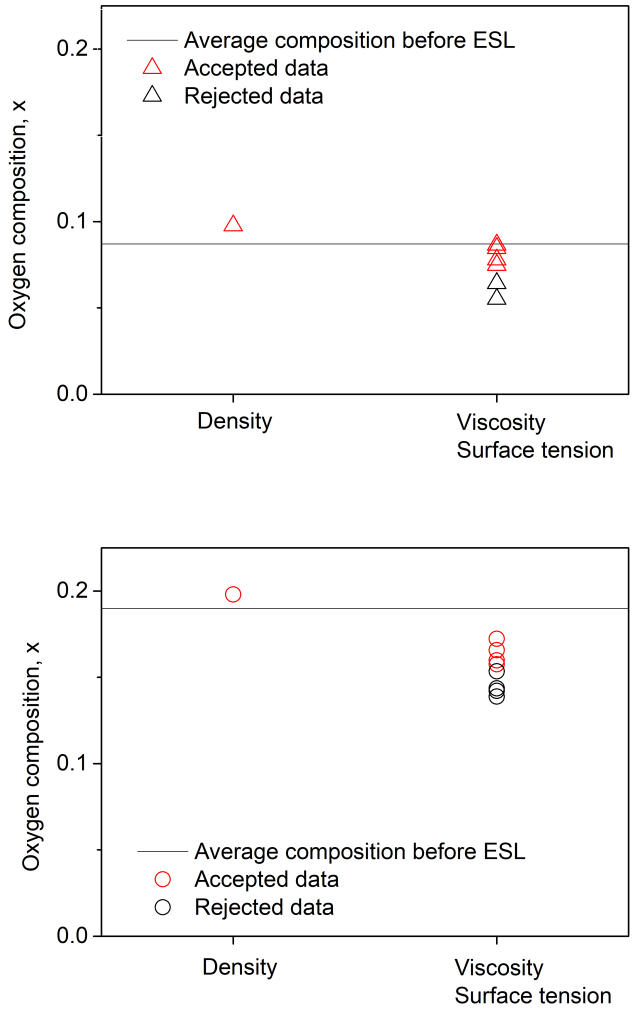

Figure 2.10: $Zr_{1-x}O_x$ sample's composition after density measurement or oscillating drop experiment.

to the large number of data points obtained during density measurements, far fewer data points can be taken during oscillating drop experiments for a given sample. In this work, the temperatures at which oscillating drop experiments were conducted fell within a narrow range. Therefore, the surface tension and viscosity results are expressed as single data points with corresponding x and y errors in Figs.2.12 and 2.13.

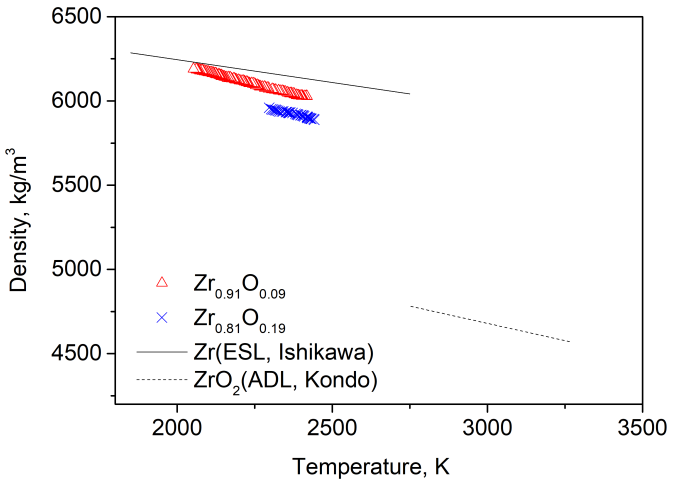

Figure 2.11: Density of liquid $Zr_{1-x}O_x$ samples

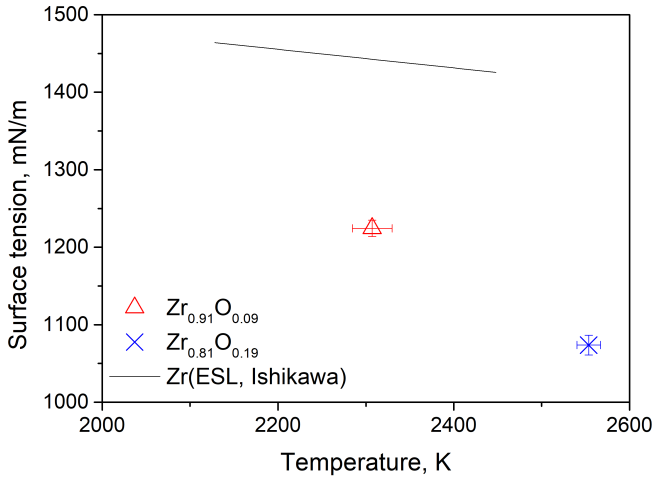

Figure 2.12: Surface tension of liquid $Zr_{1-x}O_x$ samples

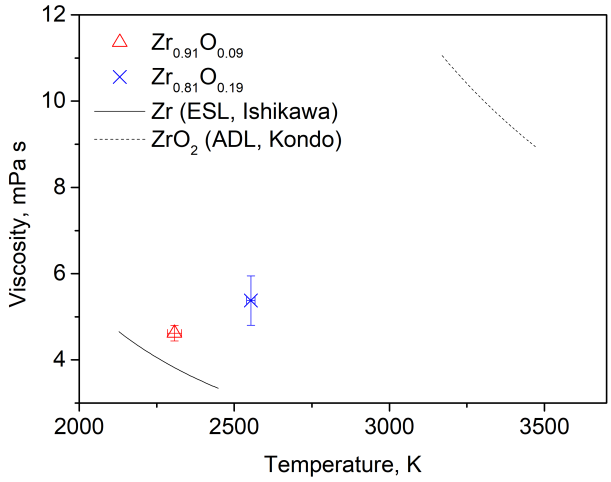

Figure 2.13: Viscosity of liquid $Zr_{1-x}O_x$ samples

3

Experimental setup

Chapter 3 discusses the aerodynamic levitator setup used in this work. Two different types of conical nozzles are used for different purposes, and fiber lasers and CO_2 lasers are used to heat metals and oxides, respectively. For a specific type of laser, the specifications of the corresponding laser optics, camera, and illumination systems are provided in this chapter. Explanations on the temperature calibration method based on Wien's law and the shadowgraph imaging technique are

given at the end of this chapter.

3.1 Aerodynamic levitator setup

Images of the two aerodynamic levitators used in this work are shown in Figs.3.1 and 3.2. The specifications of the levitation chamber, levitation nozzle, laser, laser optics, and camera are discussed in the following subsections.

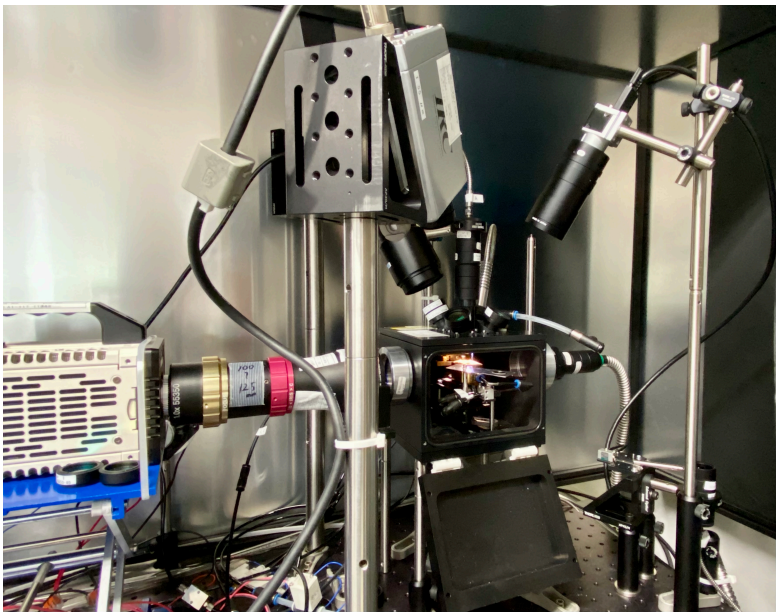

Figure 3.1: ADL setup (fiber laser) used in this work.

3.1.1 Levitation chamber

The same levitation chamber's design is used in the fiber laser ADL setup and the CO_2 laser ADL setup. The levitation chamber's wall is made from black alumina to eliminate laser reflections. As shown in Fig.3.3, two circular ports are made on the opposite sides of the chamber for shadowgraph imaging (see section.3.2). One of the two ports is connected to the background light, and the other

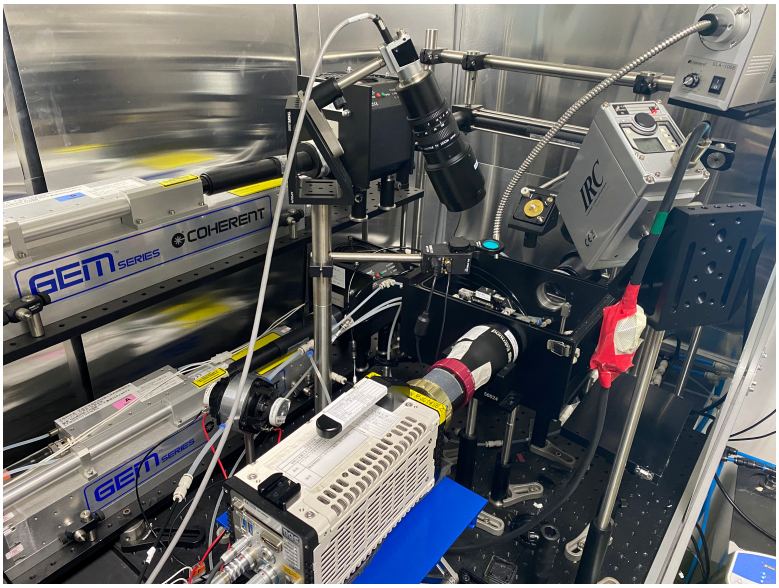

Figure 3.2: ADL setup (CO_2 laser) used in this work.

to the high-speed camera for recording. In addition, five ports are made on the levitation chamber's top plate. Four of them are at a 60° angle from the top plate and are used for chamber illumination, high-temperature observation, room-temperature observation, and temperature measurement, respectively. The port in the middle, pointing directly upward, is for the top laser. Although not shown in Fig.3.3, a circular opening is made on the chamber's bottom plate for the bottom laser.



Figure 3.3: Levitation chamber used in this work.

3.1.2 Levitation nozzles

Two types of converging-diverging conical nozzles (normal and splittable) were used in this study. The splittable nozzle is used whenever an unobstructed view of the sample is necessary. The splittable nozzle design was first introduced by Arai et. al.[99] to perform quenching experiments with ADL and has been applied in the study of latent heat of fusion of molten oxides by Ushakov et al.[100]. 3D models of the two types of nozzles are shown in Fig.3.4. The conical nozzle's orifice is be-

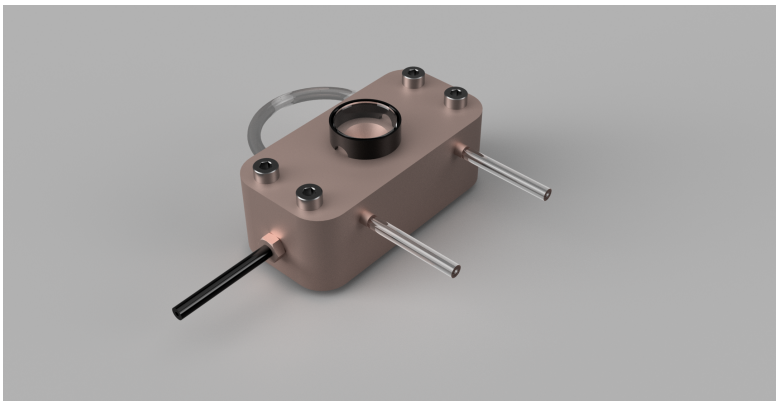

Normal conical nozzle

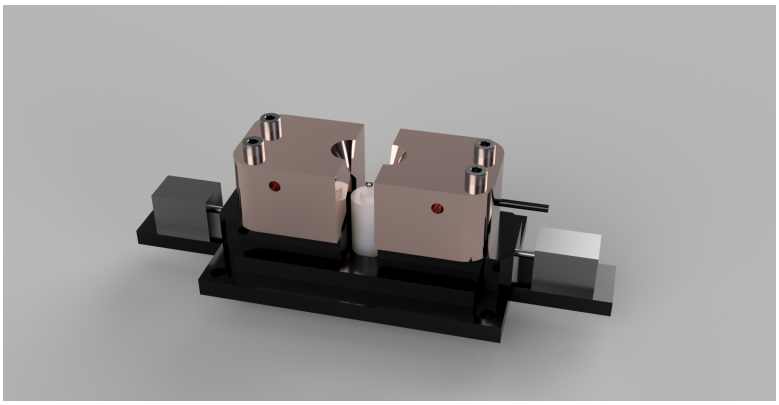

Splittable nozzle

Figure 3.4: 3D renderings of the nozzles used in this work.

tween 1.0 to 1.4 mm in diameter, with an opening semi-angle of 30°. For both types of nozzles, the

levitation gas is introduced through a channel within the nozzle, which can be seen in Fig.3.4 (black tube). Because levitation gas comes from the side of the nozzle and not directly from the bottom, the nozzle's bottom needs to be sealed to ensure gas tightness. For the normal nozzle, this is done using sapphire or NaCl windows. For the splittable nozzle, the stainless steel tube that supports the boron nitride platform acts as a seal when the nozzle is closed. Gas-driven linear motors are used to open and close the splittable nozzle, as shown in Fig.3.4 and later in Fig.5.1.

Initially, only the normal nozzle is cooled with cooling water to maintain a constant surrounding temperature for heat capacity measurements. Now, cooling water channels have been incorporated into the splittable nozzle's design. Finally, a top cover with a sapphire window is placed on the nozzle to minimize the sample's oxidation. Two small openings are made on the side of this top cover to allow the levitation gas to exit the nozzle. The top cover can be seen in Fig.3.4 on the normal nozzle.

3.1.3 Laser, pyrometer, and laser optics

Because of their different laser absorption spectrums, metals and metals oxides are heated using 976 nm fiber lasers (nLight, Pearl) and 10.6 μm CO_2 lasers (Coherent), respectively. In this work, only the top laser is used in the newly developed density and surface tension measurement methods. For heat capacity measurement, both the top and bottom lasers are used to minimize the temperature gradient within the sample. It is shown later in Fig.5.2 that the sample, when heated with the top laser or both top/bottom lasers, produces roughly the same cooling curves. Therefore, the temperature gradient within the roughly 1 mm diameter sample during the experiment was considered negligible. For the two ADL setups, the specifications of the lasers and pyrometers are summarized in Tab.3.1. Detailed specifications of the pyrometers are listed in Tab.3.3.

Various laser filters, listed in Tab.3.2, are placed within the ports on the top plate of the levitation chamber as shown in Fig.3.3. The heating laser reflected by the sample is blocked off by the laser filters, enhancing the pyrometer's signal-to-noise ratio. Without laser filters, the reflected heating

	Laser	Pyrometer
Metals (fiber laser setup)	Fiber laser, 976 nm	1.55 μm
Oxides (CO_2 laser setup)	CO_2 laser, 10.6 μm	0.9 μm

Table 3.1: Specifications of the lasers and pyrometers.

laser could make the pyrometer's signal unreadable for liquid metals with low emissivity. Sapphire windows are used to protect these filters from metal or metal oxide vapors. In addition, sapphire windows and NaCl windows are used whenever a window needs to be placed along the laser's path. Due to their different absorption spectrum, sapphire windows are used with fiber lasers and NaCl windows with CO_2 lasers.

	Fiber laser setup	CO2 laser setup
Pyrometer port	1400 nm longpass filter	950 nm shortpass filter
Illumination port	-	-
Observation port 1	950 nm shortpass filter	750 nm shortpass filter
Observation port 2	450 nm shortpass filter	-

Table 3.2: Various laser filters installed on the levitation chamber.

	IR-CAI	IR-CAS
Detector	InGaAs	Si
Wavelength	1.55 μm	0.9 μm
Precision	within 0.2°C	within 0.2°C
Accuracy*	below 1000°C, $\pm$5°C from 1000°C to 1000°C, $\pm$0.5% from 1500°C to 2000°C, $\pm$1% above 2000°C, $\pm$2%	

Table 3.3: Specifications of the pyrometers.

*when measuring a blackbody ($\varepsilon = 1$)

3.1.4 Camera and illumination

In this work, a high-speed camera (MEMRECAM HX-7s, nac Image Technology) is used for image recording. The images are generally taken at a rate of 4000 fps and a resolution of 1024×928. The camera is equipped with a telecentric lens (1.0X, 2/3", Gold TL, Edmund) to eliminate perspective errors from the sample's movements. Shadowgraph images [101] of the sample's shadow against a bright background are taken with the high-speed camera. Details on how to take such shadowgraphs are provided in section.3.2, and the equipment used is listed in Tab.3.4. Finally, the levitation chamber is illuminated with a regular LED light.

3.2 Image analysis method

3.2.1 Shadowgraph imaging

The shadowgraph technique [101] is used for sample observations at elevated temperatures. Images of the sample's shadow against a white background are used to offer a constant and sharp contrast so the sample's perimeter can be determined with greater accuracy. Compared to shadowgraphs, images of a bright sample against a black background suffer from the blooming effect, where the bright sample appears to be bigger than it actually is. A bandpass filter with a wavelength near/in the UV range is used because the sample's radiance is relatively weak at this wavelength. A background light emitting at the same wavelength would appear much brighter than the sample. A schematic showing how shadowgraphs are taken is shown in Fig.3.5.

The wavelength of the bandpass filter depends on the measurement temperature because the peak of the radiation curve shifts to lower wavelengths with increasing temperature. The specifications of the bandpass filters and background lights are summarized in Tab.3.4. A schematic showing the relationship between the bandpass filter's wavelength and the target sample's temperature is

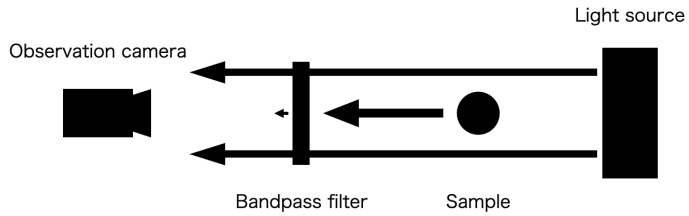

Figure 3.5: Schematic of the shadowgraph setup.

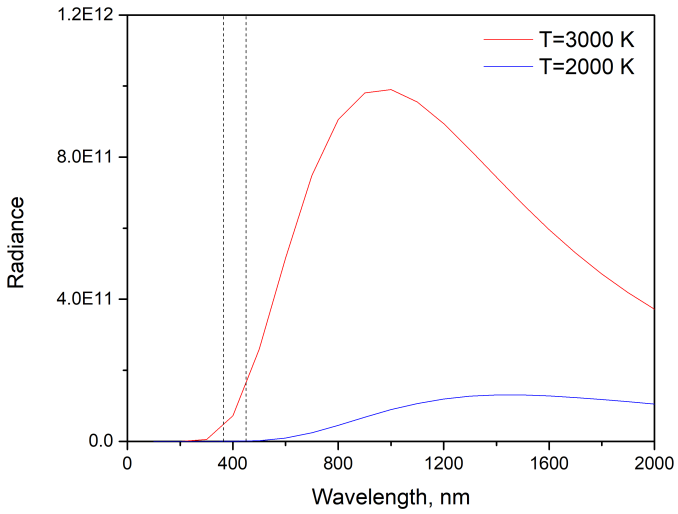

Figure 3.6: Bandpass filter's effect on a blackbody's radiance at different temperatures.

shown in Fig.3.6. Images of a molten iron sample taken under several different lighting conditions are shown in Fig.3.7. The sample's downward movement is caused by its increased density when cooled.

	Temperature	Bandpass filter	Background light
Molten metals	∼2000 K	445 nm, Thorlabs	White light, OptoSigma
Molten metal oxides	∼3000 K	365 nm, Thorlabs	365 nm, Hamamatsu

Table 3.4: Specifications of the components used for shadowgraph imaging.

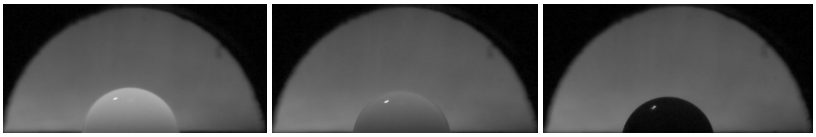

No bandpass filter, background light

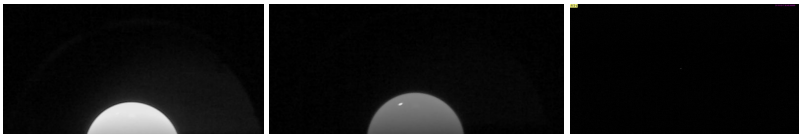

No bandpass filter, no background light

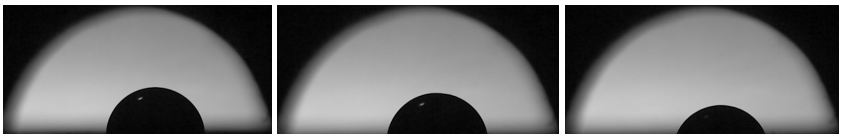

Bandpass filter, background light

Figure 3.7: Images taken with different light sources and filters. Sample's temperature decreases from left to right.

3.2.2 Elliptical fitting

The captured shadowgraphs are then processed using the software DIPP-MACRO II, where the edges of the sample are detected, and the sample's shape is fit into an ellipse, like the one shown in Fig.3.8. The ellipse's semi-major and semi-minor axis lengths are used in density and surface tension calculations.

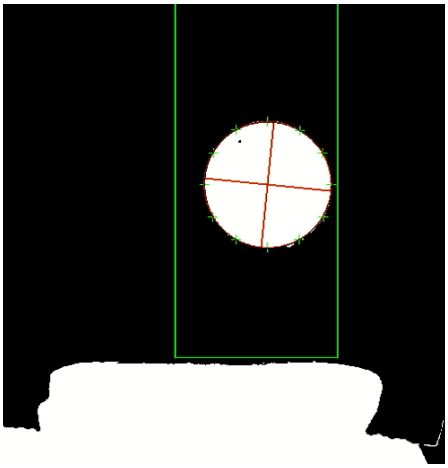

Figure 3.8: Shadowgraph image processing with DIPP-MACRO II.

For a sample undergoing the l=2 mode oscillation, its oscillation can be expressed with a time-dependent second-order Legendre polynomial, as shown in Fig.3.9. The blue line is generated with a second-order Legendre polynomial, and the red line is an ellipse constructed using five points (0,0) (0, y_{max}) (0, y_{min}) (x_{max}, 0) (x_{min}, 0). When the oscillation amplitude is large enough, the sample's cross-section is no longer an ellipse (Fig.3.9), which can potentially influence how the DIPP-MACRO II software fits the sample's perimeter. **Therefore, during surface tension and viscosity measurements, one should keep in mind not to induce an overly-large oscillation amplitude. This is also important as the sample's oscillation might no longer be that of a simple harmonic oscillator if the oscillation amplitude is larger than 5%[62].**

3.3 Temperature analysis method

3.3.1 Cooling curve correction

The cooling curve of a levitated sample under vacuum condition (ESL) was already shown in section.2.2.3. Although a sample levitated with ADL experiences convection heat loss in addition to

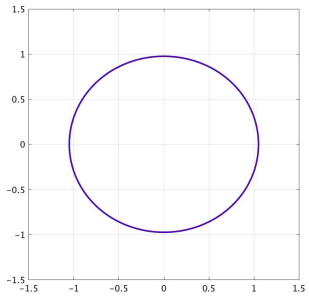

Sample radius = 1, oscillation amplitude = 0.025.

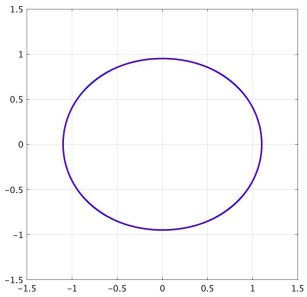

Sample radius = 1, oscillation amplitude = 0.05.

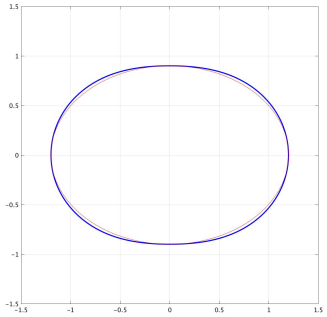

Sample radius = 1, oscillation amplitude = 0.1.

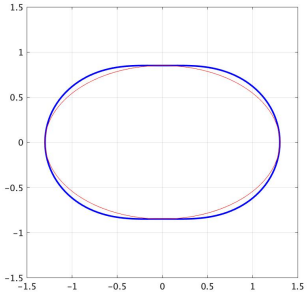

Sample radius = 1, oscillation amplitude = 0.15.

Figure 3.9: Front view of the l=2 zonal harmonics with different amplitudes and their deviations from an ellipse.

the radiative heat loss, the overall features of the cooling curve are the same. The cooling curve of a platinum sample levitated with ADL is shown below in Fig.3.10.

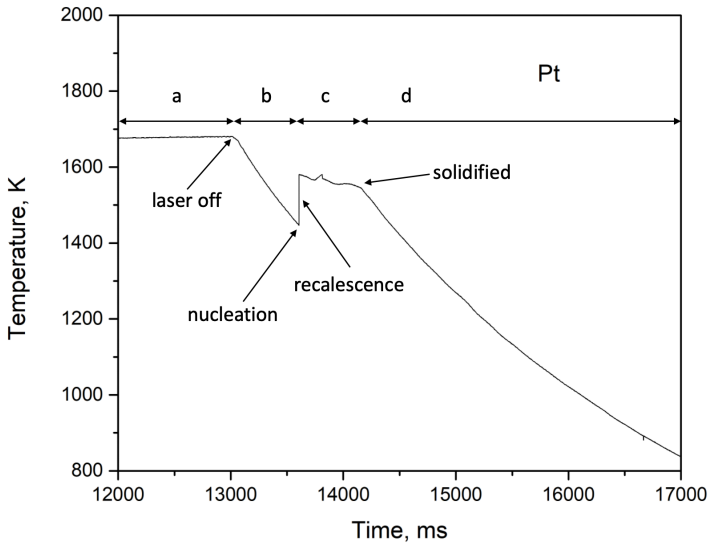

Figure 3.10: Cooling curve of a liquid platinum sample.

The sample reaches a constant temperature just before the laser is turned off at the end of **region a**. The sample is then allowed to cool, in **region b**, while levitated. Because the sample is not in contact with any container, deep undercooling can be achieved. Eventually, homogeneous nucleation starts, and an increase in temperature, called the recalescence process, is observed because of the increase in the sample's entropy. The sample undergoes liquid-to-solid phase transformation at the melting point in **region c** and completely solidifies in **region d**.

However, the cooling curve obtained directly from the pyrometer's signal does not show the sample's actual temperature. Since a pyrometer treats the sample as a blackbody with an emissivity value of $\varepsilon = 1$, the as-obtained cooling curve must be corrected. **In this discussion, the molten sample's emissivity is assumed to be temperature-independent and equal to its value at the melting point[102].**

The sample's spectral radiance at a given temperature and wavelength, $I(\lambda, T)$, is expressed with Planck's law:

$$I(\lambda, T) = \varepsilon \frac{2hc^2}{\lambda^5} \frac{1}{e^{hc/\lambda k_B T} - 1} \tag{3.1}$$

When $h\nu \gg k_B T$, Planck's law can be simplified into Wien's law:

$$I(\lambda, T) = \varepsilon \frac{2hc^2}{\lambda^5} e^{-hc/\lambda k_B T} \tag{3.2}$$

The as-obtained temperature given by the pyrometer, T_{pyro}, and the actual temperature of the gray body sample, T, can be related because their radiance is equal.

$$\varepsilon e^{-hc/\lambda k_B T} = e^{-hc/\lambda k_B T_{pyro}} \tag{3.3}$$

For a sample with a known melting point, T_m:

$$\varepsilon e^{-hc/\lambda k_B T_m} = e^{-hc/\lambda k_B T_{pyro,T_m}} \tag{3.4}$$

T_{pyro,T_m}, the as-obtained temperature from the pyrometer at the sample's melting point, can be found by locating the end of the sample's recalescence on the as-obtained cooling curve (end of **region b** and start of **region c** in Fig.3.10).

Eqns.3.3 and 3.4 combine to give the following expression for temperature correction:

$$\frac{1}{T} - \frac{1}{T_{pyro}} = \frac{1}{T_m} - \frac{1}{T_{pyro,T_m}} \tag{3.5}$$

The as-obtained cooling curve and a corrected cooling curve for a liquid platinum sample cooled with Ar gas are shown in Fig.3.11.

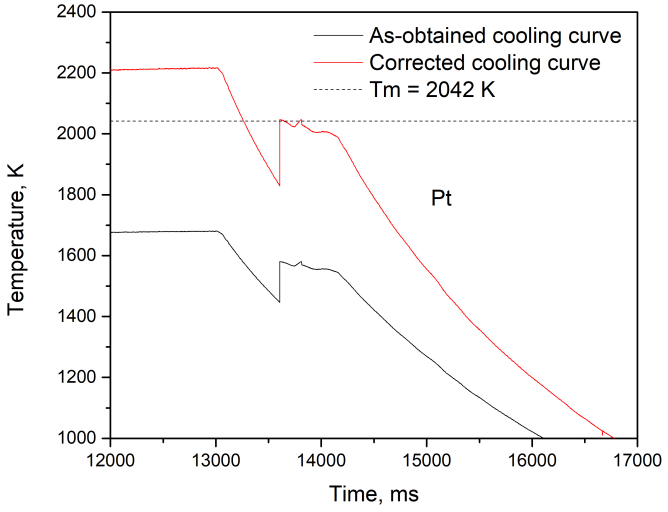

Figure 3.11: A comparison between the as-obtained and corrected cooling curves of a liquid platinum sample cooled under Ar gas.

3.3.2 Cooling curve estimation for drop experiments

A sample heated and levitated within the normal nozzle is constantly monitored with a pyrometer, and its temperature can be accurately recorded. However, density and surface tension measurements were done by dropping the levitated molten sample with the splittable nozzle. While falling, the sample is no longer visible to the pyrometer, and temperature estimation is necessary.

The sample's heat loss under the following three scenarios are considered to estimate the temperature of the sample during free-fall. All cooling curves obtained during the experiment, like the one shown in Fig.3.11, belong to case 1.

- Case 1. convection (in the nozzle) + radiation

  $dT/dt = \frac{A}{C_p m}[\varepsilon\sigma T^4 + h_{nozzle}(T - T_\infty)]$

- Case 2. convection (free-falling) + radiation

$dT/dt = \frac{A}{C_p m}[\varepsilon\sigma T^4 + h_{falling}(T - T_\infty)]$

- Case 3. purely radiation

  $dT/dt = \frac{A}{C_p m}[\varepsilon\sigma T^4]$

Obviously, for the same sample at the same initial temperature, its temperature decrease will be more drastic in cases 1 and 2. In cases 1 and 2, the heat transfer coefficient, h, for convection heat loss is related to the relative speed of the sample to the surrounding gas. The sample's relative speed to the levitation gas is higher when levitated within the nozzle than during free-fall. This means that using the cooling curve from case 1 to estimate the cooling behavior of a free-falling sample (case 2) will underestimate the sample's temperature. On the other hand, the free-falling sample's convection heat loss is non-zero. This suggests that using case 3 to estimate the sample's actual temperature will arrive at an overestimation. By combining cases 1 and 3, the lower and upper limits of the free-falling sample's temperature can be obtained.

Perhaps not apparent now, but the sample's density and surface tension is not measured at a single temperature. Density measurement takes roughly less than 50 ms, and surface tension measurement takes approximately 50 to 100 ms. If free-fall starts at time t_0, and the density measurement starts from t_1 to t_2, the temperature uncertainty can be calculated as follows:

- Case 1, when applied from t_0 to t_2, gives the lower limit of the sample's temperature.
- Case 3, when applied from t_0 to t_1, gives the upper limit of the sample's temperature.

Since convection heat loss is present in the free-falling sample, case 1, i.e., the cooling curve of a sample levitated within the nozzle, better resembles the sample's actual cooling behavior after the sample is dropped. Therefore, when expressing the estimated temperature of the dropped sample, the temperature calculated based on case 1 at $(t_1 + t_2)/2$ is used, along with the upper (case 3, at t_1) and lower (case 1, at t_2) limits. The entire temperature estimation process is summed up in Fig.3.12.

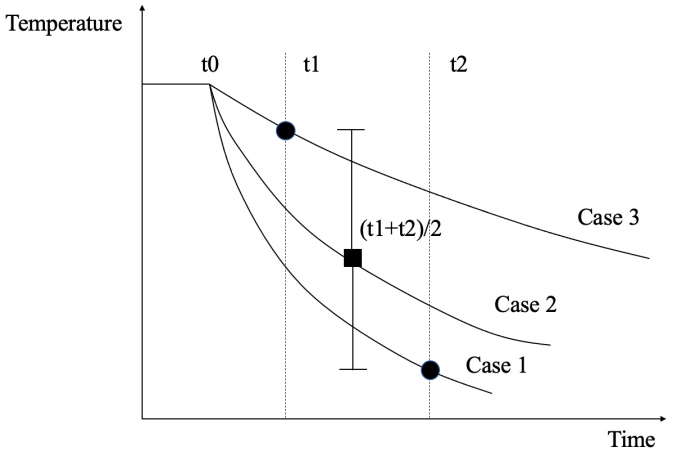

Figure 3.12: Free-falling sample's temperature estimation.

In this work, it is assumed that sample's free-cooling starts (t_0) as soon as it is dropped. It is commonsense that throughout all levitation experiments, the pyrometer should be set to observe the sample at its stably levitated position. Therefore, when the sample starts to fall, an increasingly smaller portion of the sample surface is visible to the pyrometer, causing the pyrometer's signal to slightly decrease, as shown in Fig.3.13. Three regions are highlighted in Fig.3.13: the sample's temperature when in thermal equilibrium, when dropped but is partially visible, and when completely invisible. The last temperature data point of the thermal equilibrium is selected as the temperature at t_0. The time elapsed since t_0 is simply the sample's free-falling time, which is calculated by extracting the sample's speed from the recorded shadowgraph images.

The high-speed camera records at a rate of 4000 fps, so the elapsed time since t_0 can be calculated based on the elapsed frames. However, until the gap made by the nozzle is wide enough, the sample's movement cannot be clearly identified with the naked eye, as shown in Fig.3.14. In addition, the dropped sample's initial velocity is close to zero, making it more difficult to pinpoint the exact frame when free-fall started.

However, once the sample is fully visible to the high-speed camera, its velocity can be precisely

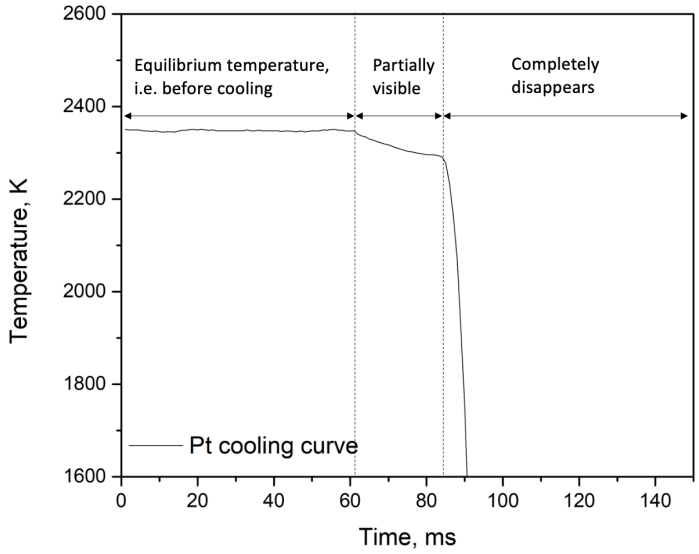

Figure 3.13: The end portion of a liquid platinum sample's cooling curve.

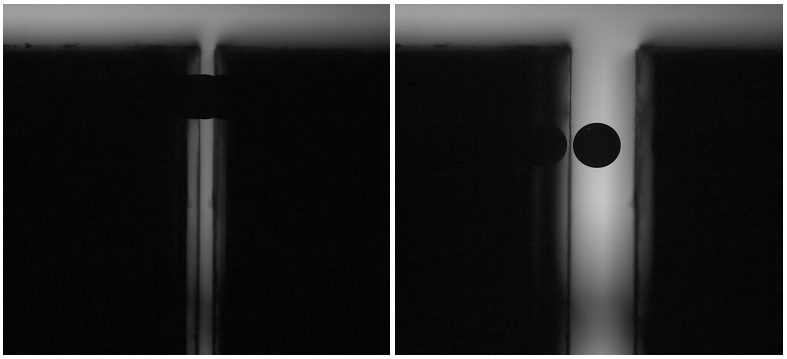

Figure 3.14: Shadowgraphs of a free-falling liquid platinum sample as the nozzle splits open.

calculated, assuming air resistance is negligible. This is done by first measuring the distance traveled by the sample's center of mass in pixels, which is then converted into millimeters with calibration. Given that one frame is 0.25 ms, the sample's speed, as well as the time (elapsed free-fall time) it takes to accelerate to that speed, can then be calculated. This process is shown in Fig.3.15. It should be clarified that the above calculation is only necessary because the sample is initially partially visible to the camera. The time elapsed after the sample is fully visible to the camera can be measured simply by converting recorded frames into milliseconds.

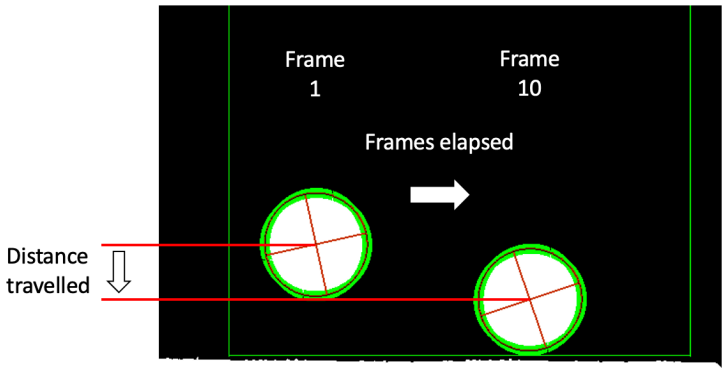

Figure 3.15: Schematic showing the method for calculating sample's speed which is used to obtain the time it spent in free-fall.

4

Heat capacity measurement (Multiple-gas cooling method)

Progress in heat capacity measurement with ADL has been slow, with only one attempt by Millot et al. [50] to measure the heat capacity of liquid boron while considering only radiative heat loss. This assumption is clearly invalid for ADL because the sample is not levitated under vacuum.

In addition, to accurately calculate the radiative heat loss, one needs the total hemispherical emissivity of the sample, which is usually not available. Therefore, a comprehensive heat loss model and an emissivity measurement method are needed for ADL.

The multiple-gas cooling method introduced in this chapter considers both the radiative heat loss and convective heat loss of a sample levitated with ADL. The heat loss model used is based on the Newton-Stefan model, and the convective heat transfer coefficient is expressed with the Ranz-Marshall correlation. The heat loss model was then calibrated using existing heat capacity and emissivity data of liquid platinum [3]. The heat capacity data of various liquid metals measured with the multiple-gas cooling method in this study agree well with literature values.

This chapter discusses the setup for heat capacity measurements, the heat loss model used, and the obtained heat capacity results of various liquid transition metals. Finally, the heat of fusion measurements, based on the multiple-gas cooling method, are also attempted.

4.1 Measurement setup

For heat capacity measurements, the normal nozzle with an orifice diameter of 1.4 mm is used. In the convective heat loss term, the surrounding temperature is a crucial parameter, and therefore the nozzle must be kept at a constant temperature by circulating cooling water at 25°C. Top and bottom fiber lasers (976 nm, Pearl) are used to minimize the vertical direction temperature gradient that can introduce an additional conductive term to the heat loss model. The temperature recording system consists of a pyrometer (1.55 μm, CHINO), a 1400 nm longpass filter, and a data logger that records the signal every 1 ms.

During the experiment, a cover with a sapphire window is placed on top of the nozzle to prevent sample oxidation. Three types of levitation gases are used: Ar (5N, Air Liquide), Kr (5N, Tokyo Gas Chemicals), and Ar-4%H_2 (Air Liquide). Heat capacity measurements are done under Ar and

Kr gas flow, while Ar-4%H_2 is used to clean the sample's surface between measurements. The samples used in this study are between 1.2 to 1.6 mm in diameter, and the purity of the various metal samples used are listed later in Tab.4.2.

4.2 Heat loss and heat capacity evaluation method

4.2.1 Heat loss related parameters

A sample levitated with ADL, shown in Fig.4.1, experiences both forced convective heat loss and radiative heat loss to its surroundings.

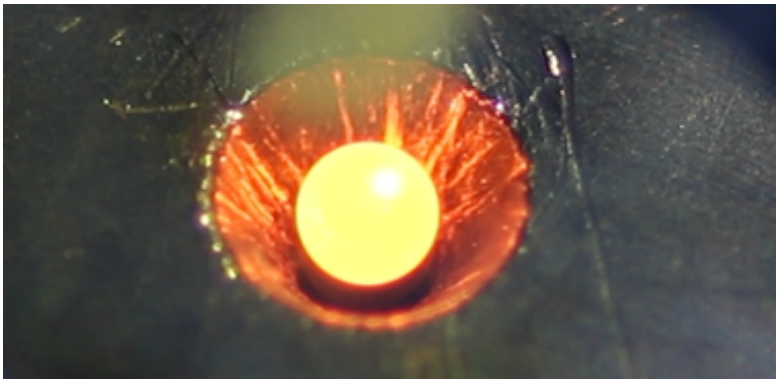

Figure 4.1: A molten sample levitated with ADL.

The Newton-Stefan's heat loss equation can be conveniently used to describe the heat flux of such a system:

$$\frac{Q}{A} = q = \varepsilon\sigma(T_{sample}^4 - T_{gas}^4) + h(T_{sample} - T_{gas}) \tag{4.1}$$

In this study, the sample's temperature is much higher than that of the surrounding gas, and therefore the radiative heat loss term in Eqn.4.1 is simplified:

$$q = \varepsilon\sigma T_{sample}^4 + h(T_{sample} - T_{gas}) \tag{4.2}$$

The heat transfer coefficient, h, is defined as a proportional constant between heat flux and the temperature gradient:

$$h = \frac{q}{\Delta T} \tag{4.3}$$

and can be expressed using the Nusselt number,

$$Nu = \frac{hL}{\kappa} \tag{4.4}$$

with the characteristic length, L, equal to the sample's diameter.

The Nusselt number is the ratio between the convective heat transfer and the conductive heat transfer across a surface. Although convection and conduction are two different heat transport methods, convection always involves some degree of conduction at the contact surface. For forced convection, the Nusselt number is often related to the Reynolds number, Re, and Prandtl number, Pr.

The Reynolds number, Re, is proportional to the fluid's speed and viscosity, which describes the flow pattern of the fluid (in this case, levitation gas). Flow with low Reynolds numbers is laminar with no lateral mixing or disturbance. In contrast, flow with higher Reynolds numbers is chaotic and turbulent. Mathematically, the Reynolds number is expressed as:

$$Re = \frac{v\rho L}{\mu} \tag{4.5}$$

On the other hand, the Prandtl number is a dimensionless parameter that describes how well the fluid can conduct heat compared to how well it can flow. Mathematically, it is expressed as:

$$Pr = \frac{C_p \mu}{\kappa} \tag{4.6}$$

Fluids with Prandtl numbers small than 1 are good heat-conducting agents because of their high thermal conductivity and low viscosity, and vice versa.

4.2.2 Application of the Ranz-Marshall correlation

For a free-falling sphere experiencing a flow with uniform velocity, the convective heat loss can be expressed using the empirical Ranz-Marshall correlation:

$$Nu = 2 + 0.6Re^{0.5}Pr^{0.33} \tag{4.7}$$

The convective heat loss term of Eqn.4.2 can be rewritten using the Ranz-Marshall correlation as:

$$q = \varepsilon\sigma T_{sample}^4 + \frac{Nu \cdot \kappa}{L}(T_{sample} - T_{gas}) \tag{4.8}$$

$$q = \varepsilon\sigma T_{sample}^4 + (2 + 0.6Re^{0.5}Pr^{0.33})\frac{\kappa}{L}(T_{sample} - T_{gas}) \tag{4.9}$$

Various thermophysical properties of the levitation gas are necessary to calculate the fully-expanded convection heat loss term in Eqn.4.10. More importantly, the relative speed, v, between the sample and the uniform velocity field is required. For a stably levitated sample, its relative speed to the levitation gas was assumed to equal to its terminal velocity. In addition, the relative speed between the levitated sample and the gas is assumed to be uniform across the entire sample surface.

$$q_{conv} = (2 + 0.6\frac{v\rho L}{\mu}^{0.5}\frac{C_p\mu}{\kappa}^{0.33})\frac{\kappa}{L}(T_{sample} - T_{gas}) \tag{4.10}$$

For a falling sample, the drag force it experiences is related to its speed and drag coefficient, C_d. At the sample's terminal velocity, the drag force and buoyancy force cancel out the effect of gravity, leaving the sample falling at constant speed instead of accelerating. In this work, buoyancy's effect is

neglected. The drag coefficient, C_d, is related to the sample's shape and gas flow (Reynolds number). The drag coefficients, C_d, of a sphere at different Reynolds numbers can be expressed as,

$$C_d = 24/Re, \quad Re < 2 \tag{4.11}$$

$$C_d = 10/Re, \quad 2 < Re < 500 \tag{4.12}$$

$$C_d = 0.44, \quad Re > 500 \tag{4.13}$$

and the terminal velocity containing the drag coefficient term is:

$$v_{terminal} = \sqrt{3gD\frac{\rho_{sample} - \rho_{gas}}{\rho_{gas}}} \tag{4.14}$$

However, for a sample levitated within a conical nozzle, the velocity vector field of the levitation gas around it is not uniform. Therefore, a modification coefficient, α, is introduced to the convection heat loss term. Because the flow around the sample in the nozzle can eventually be considered uniform if the sample is small enough, this coefficient is assumed to be related to the sample's diameter. Gas type was also considered as an relevant factor because for the same sample, properties of the levitation gas, such as density, determine the equilibrium position of the sample within the nozzle. The fully expanded heat loss equation, with α, is then:

$$q = \varepsilon\sigma T_{sample}^4 + \alpha(2 + 0.6\frac{v\rho L}{\mu}^{0.5}\frac{C_p\mu}{\kappa}^{0.33})\frac{\kappa}{L}(T_{sample} - T_{gas}) \tag{4.15}$$

From here onward, the lengthy term $(2 + 0.6\frac{v\rho L}{\mu}^{0.5}\frac{C_p\mu}{\kappa}^{0.33})$ is simply expressed as the Nessult number, Nu, again. The heat flux density, q, is rewritten in terms of power, Q:

$$\frac{Q}{A} = q = \varepsilon\sigma T_{sample}^4 + \alpha Nu\frac{\kappa}{L}(T_{sample} - T_{gas}) \tag{4.16}$$

The total amount of heat lost by the sample to reduce its temperature by ΔT, during a time of Δt, can be expressed with either ΔT or Δt:

$$\frac{C_p m \Delta T}{A} = \Delta t \{\varepsilon \sigma T_{sample}^4 + \alpha Nu \frac{\kappa}{L}(T_{sample} - T_{gas})\} \tag{4.17}$$

For an infinitesimal change in ΔT and Δt, rearrange into:

$$\frac{dT}{dt} = \frac{A}{C_p m}\{\varepsilon \sigma T_{sample}^4 + \alpha Nu \frac{\kappa}{L}(T_{sample} - T_{gas})\} \tag{4.18}$$

The left-hand side of Eqn.4.18 is the gradient of the experiment cooling curve, and on the right-hand side are three unknowns, C_p, ε, and α. The equation's degrees of freedom must be reduced to zero to obtain a unique solution set.

4.2.3 Elimination of unknown variables

Determining α

Strictly speaking, the added coefficient α could be affected by factors more than just the gas type and the sample's size. Ideally, the α value for a specific type of material levitated with a specific nozzle design under a specific type of gas should be known before the heat capacity calculation. However, to eliminate α in Eqn.4.18, the target properties, C_p and ε, must be known first. One might then consider using the reported C_p and ε of several materials to investigate whether α is additionally material-dependent. Unfortunately, there are two issues with this solution. First, the heat capacity and total hemispherical emissivity of only a very limited number of liquid metals have been reported. Second, only the heat capacity and emissivity of noble metals can be used to calculate α in Eqn.4.18. This is because sample oxidation is never fully eliminated in ADL. Therefore, the temperature curve, heat capacity, and emissivity in Eqn.4.18 are for metals potentially with a thin oxide

film. Unlike heat capacity, which is the sample's bulk property, emissivity heavily depends on the surface condition of the sample. For non-noble metals, emissivity values measured under a high vacuum in existing literature cannot be used to calculate α in Eqn.4.18.

In Chapter.2, I mentioned that both heat capacity and total hemispherical emissivity could be measured using the ESL blackbody furnace method[3]. The total hemispherical emissivity can be accurately obtained because the sample is close to a perfect sphere when levitated with ESL. Among the reported materials by Ishikawa et al.[86,88–91], liquid platinum, a noble metal, is chosen as a calibrant to remove the α coefficient in Eqn.4.15. Since only liquid platinum could be used to calculate α, it is implicitly assumed to be material-independent in this study. The thermophysical properties of liquid platinum used in the calibration are listed in Tab.4.1.

Melting point, K	2041K
Density at T_m, $g{\cdot}cm^{-3}$	19.2
Temperature coefficient, $mg{\cdot}cm^{-3}K^{-1}$	0.96
Emissivity	0.25
Heat capacity, $Jmol^{-1}K^{-1}$	38.8 ± 1.8

Table 4.1: Thermophysical properties of liquid platinum[2,3].

Calibrations on six platinum samples were performed under argon flow to understand how α changes with sample radius. The calculated α values are plotted against sample radius in Fig.4.2. For a sample cooled under argon flow, α_{Ar} is roughly constant at 0.751 ± 0.053 when its radius is between 1.2 and 1.6 mm. Using this α value and known thermophysical properties of liquid platinum listed in Tab.4.1, the cooling curve of liquid platinum can be accurately replicated, as shown in Fig.4.3. With α determined, only two unknown variables, emissivity and heat capacity remain in Eqn.4.18.

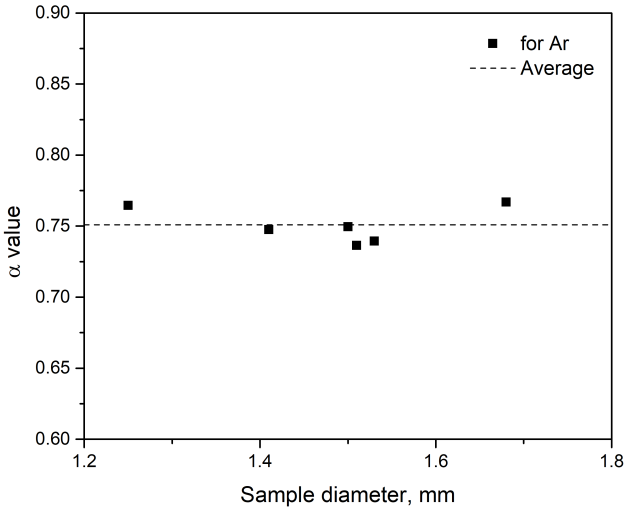

Figure 4.2: α coefficient under argon flow

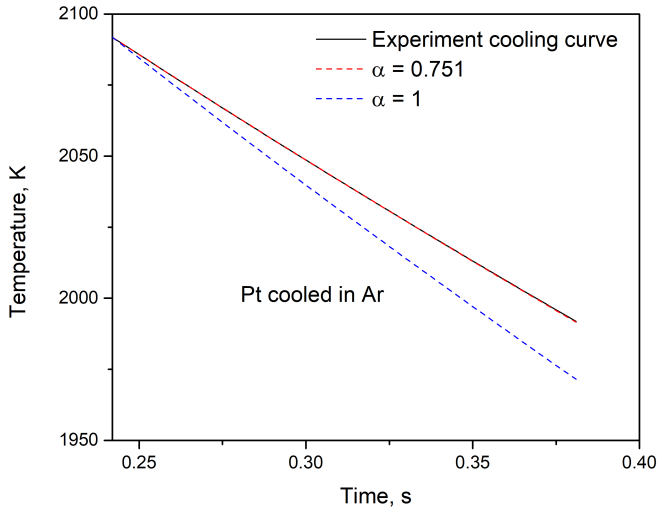

Figure 4.3: Experiment cooling curve of liquid platinum, fitted using α = 0.751 and α = 1.

Multiple gas cooling

One of the advantages of ADL is its versatility when it comes to gas choice. The two remaining unknowns, emissivity and heat capacity, can be solved using two independent cooling curves shown in Eqns.4.19 and 4.20. These independent cooling curves can be obtained by cooling the sample using argon and krypton.

$$\frac{dT_{inAr}}{dt} = \frac{A}{C_p m}\{\varepsilon\sigma T_{inAr}^4 + \alpha_{Ar} Nu_{Ar}\frac{\kappa_{Ar}}{L}(T_{sample} - T_{gas})\} \tag{4.19}$$

$$\frac{dT_{inKr}}{dt} = \frac{A}{C_p m}\{\varepsilon\sigma T_{inKr}^4 + \alpha_{Kr} Nu_{Kr}\frac{\kappa_{Kr}}{L}(T_{sample} - T_{gas})\} \tag{4.20}$$

The calculated α coefficient, $\alpha_{Kr} = 0.787 \pm 0.068$, for krypton flow is shown in Fig.4.4.

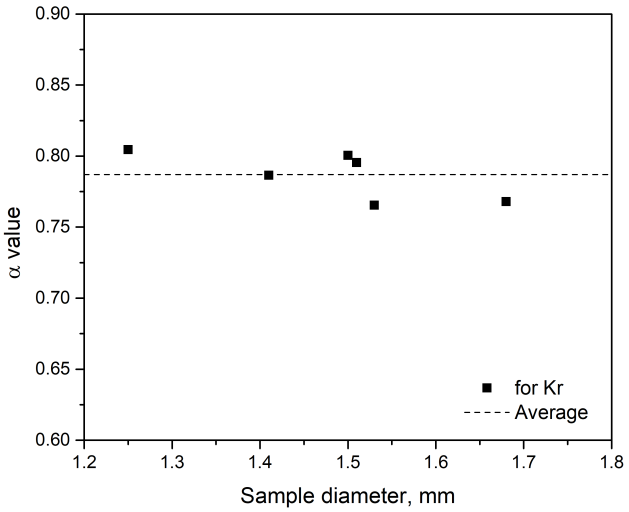

Figure 4.4: α coefficient under krypton flow

Each cooling curve has a degrees of freedom of one, and thus C_p can be expressed as a function of

ε. The intersection of the two functions, $C_p(\varepsilon)$, gives the unique pair of C_p and ε that satisfies both cooling curves. Heat capacity as a function of emissivity for a liquid platinum sample is shown in Fig.4.5. It should be noted that emissivity is a surface property and is highly sensitive to any contamination such as oxidation. Therefore, compared to emissivity obtained with a blackbody furnace under vacuum, the emissivity obtained with the multiple-gas cooling method is less accurate. On the other hand, heat capacity is the sample's bulk property and is much less influenced by the thin oxide layers formed on the sample's surface.

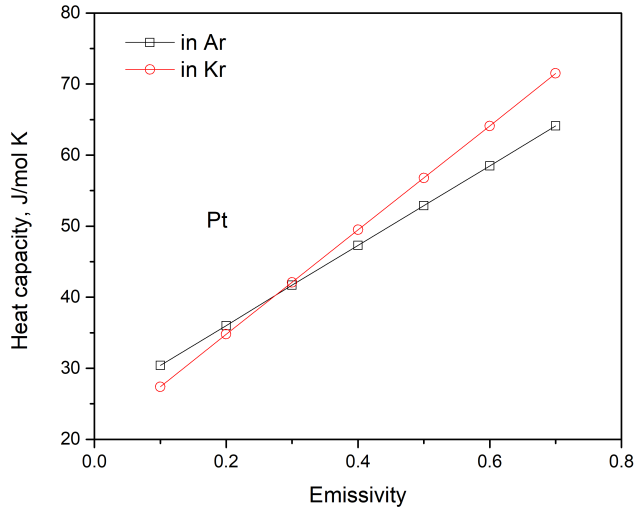

Figure 4.5: Heat capacity as a function of emissivity for a liquid platinum sample.

With the multiple-gas cooling method, the calculated heat capacity of liquid platinum in this study was 38.7±0.9. This value is in good agreement with the 38.8±1.8 reported by Ishikawa et al.[3], confirming the reliability of the multiple-gas cooling method.

4.3 Heat capacity data for various liquid transition metals

Because the end goal is to apply the multiple-gas cooling method to the study of molten oxides, the method's reliability as the sample's melting point approaches 3000 K needs to be confirmed. Therefore, the multiple-gas cooling method was applied to measure the heat capacity of various transition metals with melting points within this range. Another reason why transition metals were chosen is that there are considerable discrepancies among the values reported by different research groups. Also, for materials like ruthenium, only Paradis et al.[71] have reported its heat capacity, and the values presented in this work can fill in the gaps in the literature.

The materials used are listed in Tab.4.2. Spherical samples were made by melting with a fiber laser under Ar+4%H_2 flow. The prepared sample's mass is controlled so that its diameter is between 1.2 and 1.6 mm at the melting point in the liquid phase. The sample is weighed before and after each heating/cooling session to determine its mass change. In addition, to ensure the sample's surface condition remains the same, the sample is 'cleaned' by melting under Ar+4%H_2 flow before each measurement. The experiment procedure is summarized in a flow diagram shown in Fig.4.6. The maximum change in the sample's mass was -0.65% for liquid rhodium in this work. This negligible mass difference shows the effectiveness of the top cover with a sapphire window at preventing sample oxidation under Ar-4%H_2 flow.

The properties of the cooling gas, Ar and Kr, are listed in Tab.4.3. The densities of argon and krypton are calculated using the ideal gas law, and the heat capacity of a monoatomic ideal gas is assumed to be 1.5R. The melting points, temperature-dependent densities, and the corresponding references of the transition metals are given in Appendix.C. The cooling curves of all of the transition metals (one set per material), cooled in argon and krypton flow, are provided in Appendix.B. The calculated heat capacity values of various liquid transition metals at $T_m \pm 50$ are listed in Tab.4.4.

Element	Purity	Manufacturer
Au	3N5	Nilaco
Co	3N7	Rare Metallic
Cu	4N	Kojundo Chemical
Fe	3N up	Kojundo Chemical
Hf	3N (Zr≤0.03wt)	Furuuchi Chemical
Ir	3N	Nilaco
Mo	3N5	Nilaco
Nb	3N	Nilaco
Ni	4N	Kojundo Chemical
Pd	3N up	Kojundo Chemical
Pt	3N8	Nilaco
Ti	3N	Furuuchi Chemical
Rh	3N	Nilaco
Ru	3N	Rare Metallic
V	3N	Furuuchi Chemical
Zr	3N (Hf≤35ppm)	Rare Metallic

Table 4.2: List of chemicals used in this study.

Table 4.3: Thermophysical properties of Ar and Kr gases at room temperature[4]

Gas type	Thermal conductivity (mW/mK)	Viscosity (μPa s)
Ar	18.3	23.1
Kr	9.5	25.6

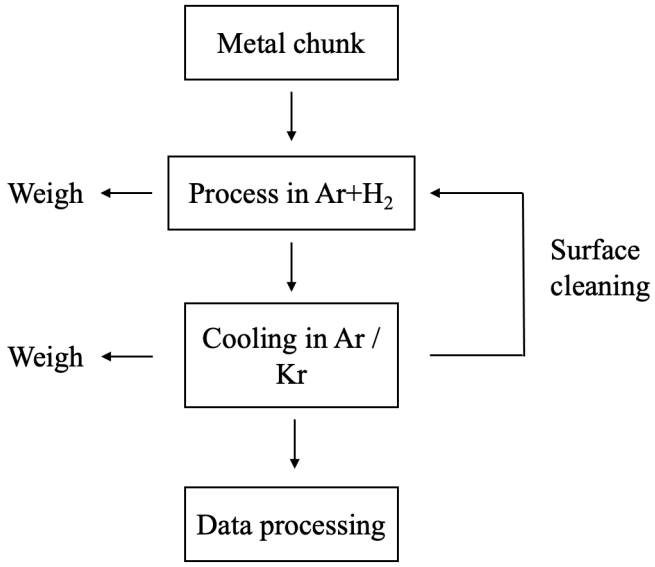

Figure 4.6: Flow diagram of the heat capacity measurement process.

Table 4.4: Heat capacity of liquid transition metals obtained in this work.

Element	C_p (J/mol K)	Reference	Comment
Au	30.9 ± 0.6	This study	ADL
	28.3	Wust [103]	Drop calorimetry
	28.9	Umino [104]	Drop calorimetry
	32.1	Plaza [105]	Drop calorimetry
	29.4	Smithells [106]	Recommended value
	33.6	Tester [107]	Drop calorimetry
Co	44.3 ± 0.9	This study	ADL
	40.6	Wang et al. [108]	Levitation drop calorimetry
	41.2	Watanabe et al. [109]	Levitation laser modulation
	45.9	Hess et al. [110]	Pulse heating
	48.5 ± 0.8	Treverton and Margrave [111]	Levitation drop calorimetry
	50.2	J. L. Margrave [112]	Levitation drop calorimetry
Cu	30.9 ± 0.7	This study	ADL
	36.3	Chekhovskoi [113]	Drop calorimetry
	32.8	Chase [114]	Recommended value
	30.2	Dokko [115]	Levitation drop calorimetry
	31.5	Smithells [106]	Recommended value
Fe	44.5 ± 0.8	This study	ADL
	46.0	Chase [114]	Recommended value
	43.9	Wilson [116]	Recommended value
	46.1	Beutl [117]	Pulse heating
	44.4	Smithells [106]	Recommended value

Table 4.4 – continued from previous page

Element	C_p (J/mol K)	Reference	Method
Hf	38.1±0.8	This study	ADL
	33.5	Paradis et al.[82]	ESL
	41.9	Korobenko et al.[118]	Pulse heating
	44.8	Kang et al.[119]	ESL with solid Hf emissivity
	60.32	Kang et al.[119]	ESL
Ir	45.1±1.4	This study	ADL
	30.1	Margrave[112]	Pulse heating
	34.3	Paradis et al.[71]	ESL
	44.2	Cagran and Pottlacher[120]	Pulse heating
	59.4	Margrave[112]	Levitation drop calorimetry
Mo	41.5±0.7	This study	ADL
	34.2	Paradis et al.[83]	ESL
	37.7	Margrave[112]	Levitation drop calorimetry
	40.7	Minakov et al.[121]	Simulation
	47.2	Cagran et al.[122]	Pulse heating
	53.7	Pottlacher et al.[123]	Pulse heating

Table 4.4 – continued from previous page

Element	C_p (J/mol K)	Reference	Method
Nb	42.3±1.8	This study	ADL
	38.9	Boboridis [124]	Pulse heating
	40.6	Margrave [112]	Levitation drop calorimetry
	40.6	Paradis et al. [84]	ESL
	40.8	Cezairliyan and McClure [125]	Pulse heating
	41.9	Ishikawa et al. [89]	ESL blackbody furnace
	45.7	Kang et al. [119]	ESL
Ni	40.3 ± 1.3	This study	ADL
	38.9	Chase [114]	Recommended value
	39.0	Vollmer [126]	Calorimetry
	39.9	Ishikawa [87]	ESL blackbody furnace
	36.4	Smithells [106]	Recommended value
	43.1	Geoffray [127]	Drop calorimetry
Pd	34.4 ± 1.3	This study	ADL
	37.4	Cagran [128]	Pulse heating
	41.2	Arblaster [129]	Recommended value
	41.0	Guthrie [130]	Recommended value
	40.5	Watanabe [131]	EML
	29.1	Paradis [132]	ESL
	34.7	Barine [133]	Recommended value

Table 4.4 – continued from previous page

Element	C_p (J/mol K)	Reference	Method
Rh	39.8±1.1	This study	ADL
	32.2	Paradis et al.[71]	ESL
	34.8	Kang et al.[119]	ESL
	41.8	Ishikawa et al.[90]	ESL blackbody furnace
	46.1	Hupf et al[134].	Pulse heating
Ru	46.4±0.9	This study	ADL
	35.9	Paradis et al.[71]	ESL
	41.9	Barin et al.[133]	Recommended value
Ti	44.4±0.7	This study	ADL
	35.3	Boboridis[124]	Pulse heating
	42.7	Kang et al.[119]	ESL
	43.4	Margrave[112]	Levitation drop calorimetry
	44.9	Ishikawa et al.[91]	ESL blackbody furnace
	45.5	Paradis and Rhim[85]	ESL
	48.9	Watanabe et al.[131]	Levitation laser modulation
	49.9	Wilthan et al.[135]	Pulse heating
V	48.0±1.4	This study	ADL
	46.9	Margrave[112]	Levitation drop calorimetry
	47.3	Margrave[112]	Pulse heating
	48.5	Ishikawa et al.[88]	ESL blackbody furnace
	48.8	Paradis et al.[81]	ESL
	49.1	Pottlacher et al.[136]	Pulse heating

Table 4.4 – continued from previous page

Element	C_p (J/mol K)	Reference	Method
Zr	38.9±0.7	This study	ADL
	39.1	Kang et al.[119]	ESL
	39.7	Paradis and Rhim[137]	ESL
	40.6	Margrave[112]	Levitation drop calorimetry
	40.9	Ishikawa et al.[89]	ESL blackbody furnace
	45.3	Brunner et al.[138]	Pulse heating

4.4 Application to latent heat measurements

As mentioned in section.2.2.4, it is possible to calculate latent heat if a relationship can be established between the thermal arrest time and the undercooling temperature. For a sample cooled in ADL, the additional convection heat loss term must be added to Eqn.2.33:

$$H_{fusion} = C_p m \Delta T + t\{A\sigma\varepsilon T_m^4 + \alpha t Nu \frac{\kappa}{L}(T_m - T_{gas})\} \tag{4.21}$$

The assumption that the solid-liquid mixture's emissivity, heat capacity, and density are constant within ΔT, the undercooling temperature, is necessary to transform Eqn.4.21 into:

$$\Delta T = -\frac{\sigma\varepsilon T_m^4 + \alpha Nu \frac{\kappa}{L}(T_m - T_{gas})}{C_p M} At + \Delta T_{limit} \tag{4.22}$$

and

$$H_{fusion} = C_p \Delta T_{limit} \tag{4.23}$$

The same sample needs to be heated and cooled repetitively to obtain different undercooling

temperatures, which makes the use of argon or krypton gas less ideal compared to that of Ar-4%H_2. Under constant Ar-4%H_2 flow, the sample's surface condition should not vary, and the thermal arrest time and undercooling temperature of the 'same' sample can be obtained. The heat capacity and emissivity obtained with the multiple-gas cooling method are used in latent heat calculations.

The temperature curves of a liquid platinum sample cooled under Ar-4%H_2, achieving different degrees of undercooling, are shown in Fig.4.7. The time of thermal arrest, t, and undercooling temperature, ΔT, are used to generate Fig.4.8. A linear relationship between the two variables is established with the least-squares method, and ΔT_{limit} is used to calculate the latent heat. The calculated undercooling limit and latent heat of this liquid platinum sample are listed in Tab.4.5.

As shown in Fig.4.8, the undercooling temperature's range is relatively narrow, and the addition of new data points could heavily influence the obtained linear relationship. Currently, this narrow temperature range is caused by the natural cooling of the sample, and methods to manually induce heterogeneous nucleation should be incorporated in future works. For example, when studying nucleation using EML [139], researchers use a ceramics needle to make contact with the bottom of the sample.

	Undercooling limit, K	Latent heat, kJ/mol
This work, ADL	max value 529 K	20.5
Wilthan et al. [140], pulse-heating	-	21.8
Hixson & Winkler [141], pulse-heating	-	24.2

Table 4.5: The undercooling limit and latent heat of liquid platinum

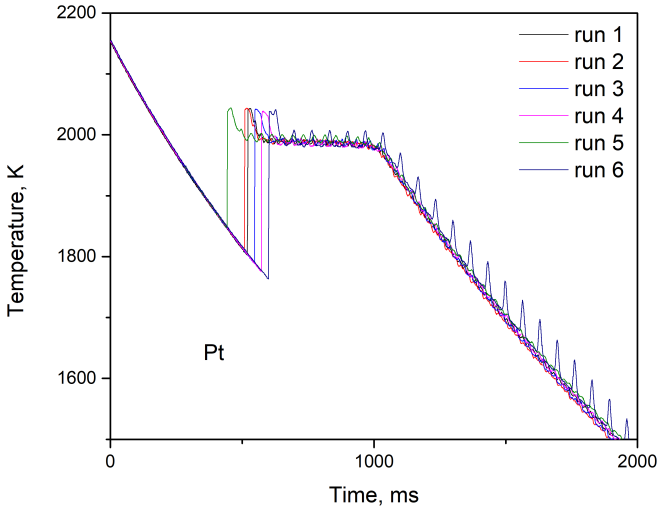

Figure 4.7: Platinum sample with different undercooling.

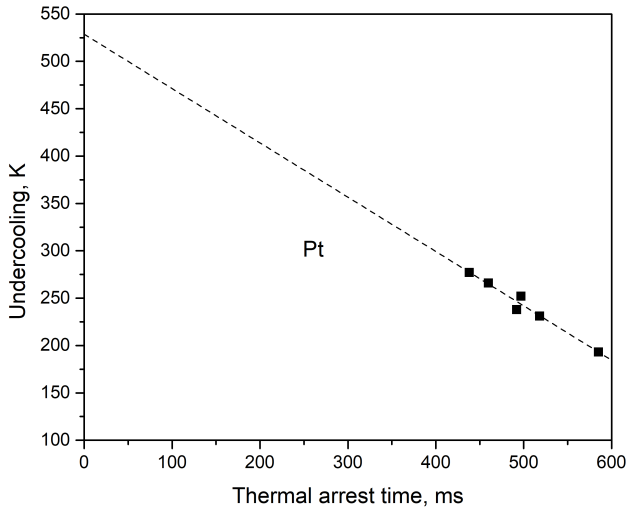

Figure 4.8: Relationship between time of thermal arrest and undercooling temperature.

5

Surface tension and viscosity measurement (Drop-bounce method)

Levitation experiments performed under normal gravity require an external force to counteract the effect of gravity, whether it be an electrostatic, electromagnetic, or aerodynamic force. As mentioned in section.2.2.2, the oscillating drop method is used with levitation techniques

to measure the surface tension and viscosity of liquid metals based on the sample's resonant frequency. However, during oscillating drop experiments, levitation forces deform and rotate the sample, causing the degeneracy in the resonant frequency to be lost. For example, for the l=2 oscillation modes, a total of five (l=2, m=0, $\pm$1, $\pm$2) resonant frequencies will be observed instead of a single degenerated resonant frequency. Rayleigh's equation for surface tension calculation requires the value of the degenerated resonant frequency, which cannot be directly obtained from experiments performed under normal gravity. Corrections to Rayleigh's equation for ground-based oscillating drop experiments to extract the degenerated resonant frequency have been introduced for ESL and EML but are not available for ADL.

Although the exact correction term is not known for ADL, past researchers[44,62] have directly used Rayleigh's equation to calculate the sample's surface tension, assuming the degeneracy in the resonant frequency still holds for ground-based ADL experiments. To verify this assumption, one needs to compare the surface tension obtained with ground-based ADL to that measured by ESL or EML under microgravity. However, this is a challenging task mainly because of three reasons:

- Oscillating drop experiment with ADL is difficult to perform on molten metals. To the best of my knowledge, only the surface tension and viscosity of molten oxides such as Al_2O_3 [44,48,62], ZrO_2 [44], and $CaAl_2O_4$ [48] have been measured by ADL.
- EML cannot levitate nor heat molten oxides.
- For ESL, a small number of surface charges is enough for sample levitation under microgravity. Because the amount of surface charges is directly related to the induced oscillation's amplitude, it is difficult to obtain sharp oscillation signals under microgravity. As of this writing, surface tension data of molten oxides obtained with microgravity ESL is unavailable.

This chapter introduces a novel surface tension measurement method for ADL called the drop-bounce method. This method utilizes the splittable nozzle with a boron nitride bounce platform

to allow the sample to oscillate during free-fall. Since gravity is the only force acting on the sample, Rayleigh's equation can be applied directly once the sample's resonant frequency is known. The sample's viscosity can then also be determined based on the oscillation's damping. This chapter first discusses the measurement and recording setup of the drop-bounce experiment. The temperature homogeneity within a sample heated by only a top laser is analyzed. Then, the sample's shape during free-fall is compared with that of MATLAB-generated spherical harmonics (l=2). Next, I will show how to obtain the oscillation's resonant frequency and damping constant for surface tension and viscosity calculations. The surface tension of liquid gold obtained with the drop-bounce method is compared with that measured by EML in space. Further, the surface tension and viscosity of liquid Al_2O_3 are determined with the drop-bounce method to demonstrate that it is capable of measuring the viscosity of viscous liquids and molten oxides. In the final section of this chapter, I will compare the surface tension of liquid Al_2O_3 obtained using the oscillating drop method, the drop-bounce method, and CFD simulations. Based on this comparison, I concluded that the resonant frequency of the l=2 m=0 mode, obtained from ground-based ADL oscillating drop experiments, when directly used with Rayleigh's equation, can produce reasonably accurate surface tension values.

5.1 Measurement setup

Setup overview

The setup used for the drop-bounce method is identical to that used in the ADL-drop density measurement experiment in Chapter.6. 3D renderings of the open and closed splittable nozzle are shown here in Fig.5.1. The sample's oscillation was observed by taking shadowgraph images at a rate of 4000 fps, 1024×928 resolution. The temperature calibration method, imaging techniques, as well as the specifications of the pyrometer and optical systems are all described in Chapter.3 for both the fiber laser and CO_2 laser setup.

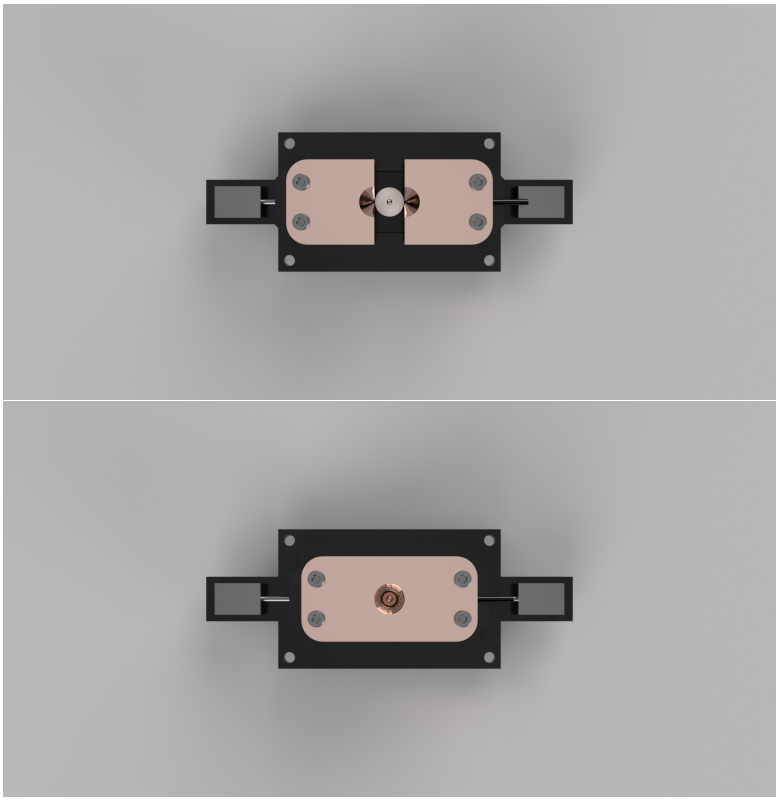

Figure 5.1: The closed and open configurations of the splittable nozzle.

After the sample is stable levitated, the splittable nozzle opens, and the sample falls until it hits the boron nitride platform, deforms, and bounces upward. The contact time between the sample and the boron nitride is on the order of microseconds; thus, heat loss through conduction is assumed to be negligible. In this work, the boron nitride platform is roughly placed 3-5 mm beneath the nozzle's orifice and is adjusted depending on the sample's mass. Because the liquid sample is in contact with the boron nitride platform, which will initiate heterogeneous nucleation, the drop-bounce method cannot be applied to undercooled liquids.

Temperature homogeneity

Two lasers should be used to heat the sample from the top and bottom to maintain temperature homogeneity within the sample. However, because of the boron nitride sample catcher, only the top laser is used for heating, which could generate a temperature gradient within the sample. To investigate whether the sample's cooling behavior changes when switching from heating with double lasers to only the top laser, I heated several platinum samples with both setups, and the cooling curves are shown in Fig.5.2. If a temperature gradient exists within the sample, heat conduction from the top part (hotter) to the bottom part (colder) of the sample is expected. Therefore, samples with temperature gradients will cool faster, and a steeper cooling curve should be observed.

For the platinum samples with a 1.4 and 1.5 mm diameter, their cooling curves are not significantly affected by the number of lasers used for heating, which means the temperature inhomogeneity can be neglected. The absence of a noticeable temperature difference can be explained by liquid platinum's relatively high thermal conductivity ($\sim$50 W/m^{2}K at its melting point[142]) and the sample's small size. However, for the sample with a diameter of 1.6 mm, the sample's cooling was faster when heated with double lasers, which cannot be attributed to the presence of a top-to-bottom temperature gradient. Because the cooling curves of the 1.6 mm diameter sample have numerous bumps, the sample's position might have been unstable, which affected its cooling. Even though the

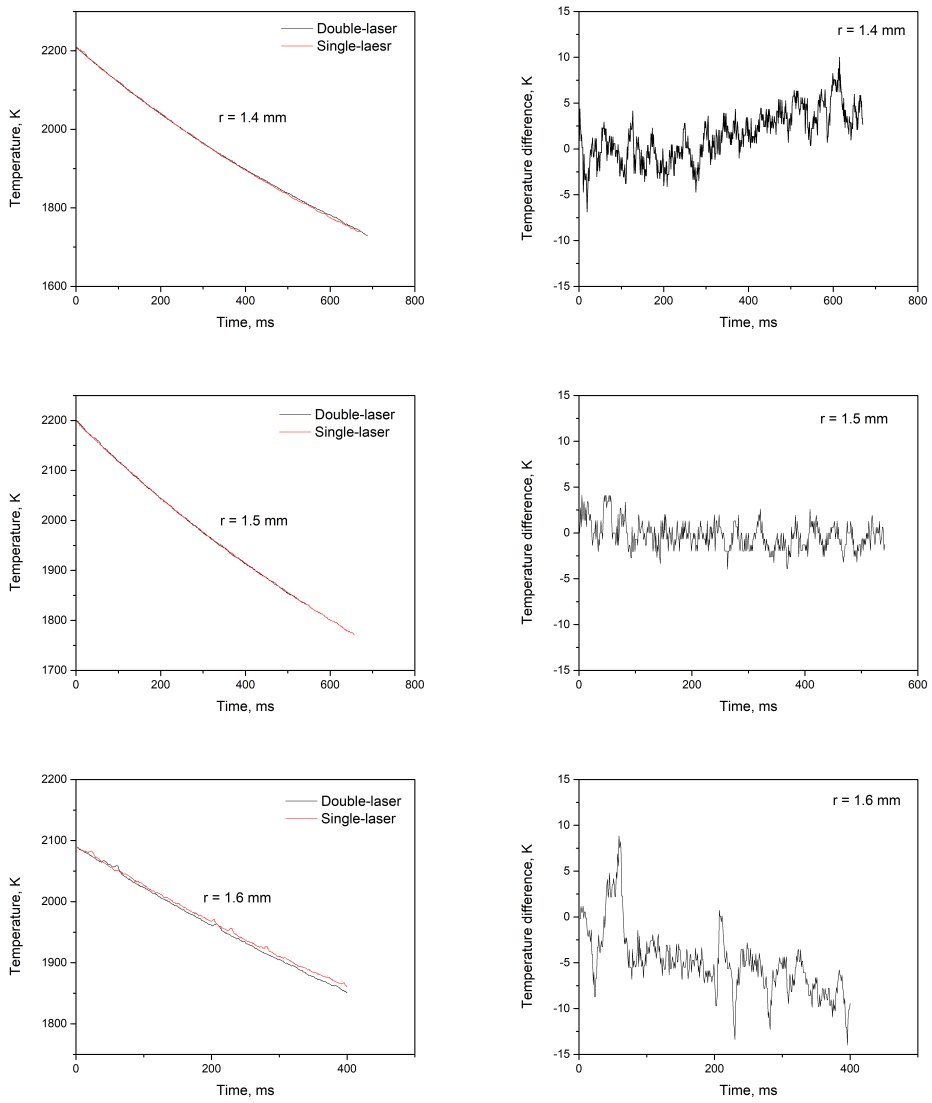

Figure 5.2: Cooling curves of liquid platinum samples cooled using a single top laser and two top-bottom lasers in argon gas. Temperature differences on the right side are expressed as $T_{double} - T_{single}$.

temperature difference increased with time for the 1.6 mm diameter sample, this difference is negligible (5 to 10 K) during the initial 100 ms when surface tension and viscosity measurements take place. The density measurements in Chapter.6 also only used the top laser for sample heating, and the temperature gradient within the sample is assumed to be negligible because the experiment time is even shorter (less than 50 ms).

Previous studies[143–145] have investigated the temperature gradient on the surface of a spherical sample heated with a single laser at thermal equilibrium. Simulations by Ge et al.[144] showed that for a 2 mm diameter alumina sphere, heating with a single top laser (to 2600 K) could induce a maximum temperature difference around 300 K if the sample rotates along the z-axis. On the other hand, if 'up to down rotation' can be induced, the temperature difference is greatly reduced to roughly 60 K. However, in this case, the sample might not be stably levitated because of the Magnus effect (Fig.5.3). McCormack et al.[143] reported a temperature difference between 100-200 K for a 3 mm diameter molten spherical oxide sample heated between 2500-3000 K with a single top laser. Finally, Schroers et al.[145] showed that, for ESL, the use of multiple diffusive-beam laser heating could reduce the sample's temperature gradient, as expected.

Based on the discussion above, the temperature gradients within the samples were considered negligible in this work for the following reasons:

- For heat capacity measurements, samples were heated from both directions instead of one[143,144], which can reduce any top-to-bottom temperature inhomogeneity.
- For density, surface tension, and viscosity measurements, although only the top laser is used, the majority of the samples measured in this work were metals that have higher thermal conductivity than metal oxides.
- The samples used in this work were smaller, which means the temperature difference between the top and the bottom of the sample is smaller at thermal equilibrium.

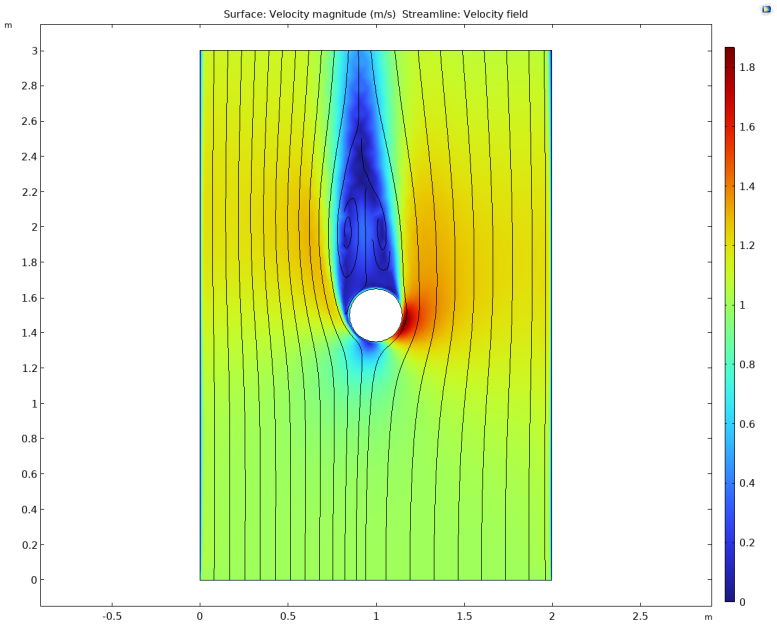

Figure 5.3: The Magnus effect simulated with COMSOL Multiphysics using a 2D laminar flow model.

Oscillation induction

Surface oscillation is induced when the sample hits the boron nitride platform and reaches maximum deformation. As the sample bounces upward, it attempts to minimize its surface area while oscillating, as shown in the timelapse images in Fig.5.4.

The sample's contour (distance from the center of mass to its perimeter) at maximum deformation can be expressed with a combination of Legendre polynomials like the one shown in Eqn.2.3. Therefore, not only the l=2 modes but higher-order oscillation modes (l = 3, 4, and higher) will also be present as the sample bounces upward. A comparison between the sample's shape at maximum deformation and the front view of the first few zonal harmonics, l = 2, 3, 4, is given Fig.5.5. From Fig.5.5, it is clear that $P_2(cos\theta)$ should have the highest oscillation amplitude. In addition, although higher-order spherical harmonic oscillations are present, the amplitude of these oscillations will be

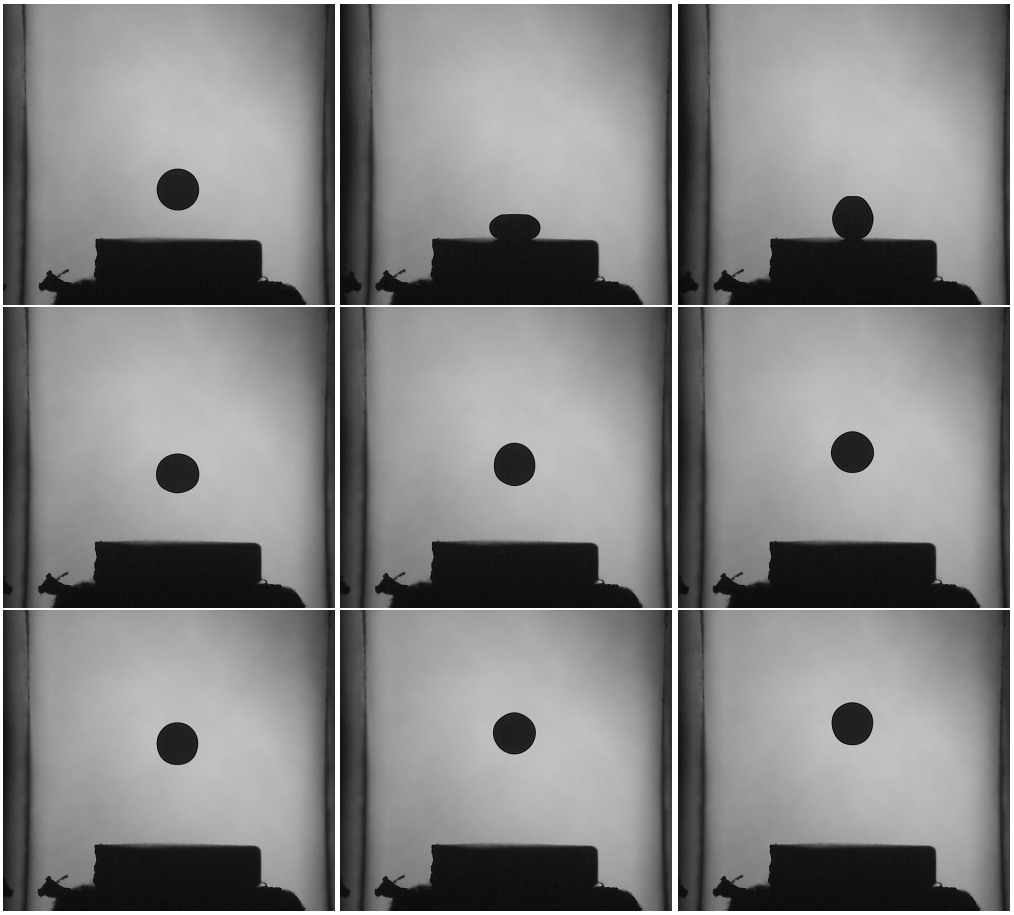

Figure 5.4: Timelapse images of a bouncing liquid gold sample

damped at much faster rates. This can be seen by rewriting Eqn.2.8 into:

$$\Gamma = \frac{4\pi R\eta}{3M} l(l+2)(l-1) \tag{5.1}$$

It is apparent that for the same sample, the damping constant, Γ becomes larger with higher-order oscillation modes (l=3, 4, ...). Therefore, as the sample bounces upward, the l=2 oscillation mode will soon dominate and eventually remain the only observable oscillation mode.

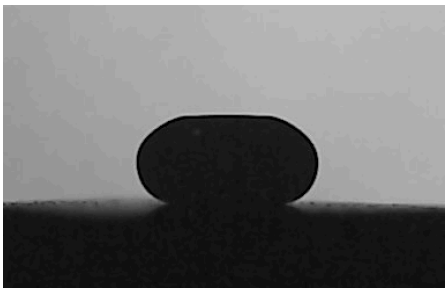

Sample deformation

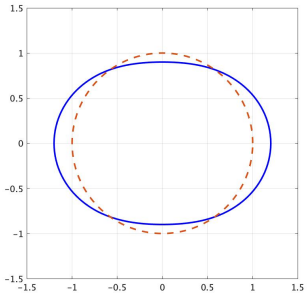

l=2

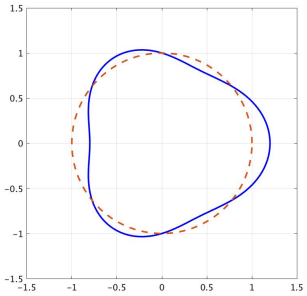

l=3

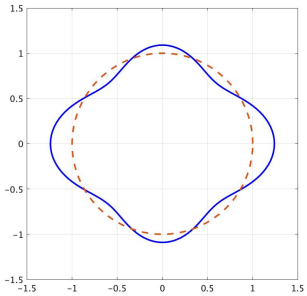

l=4

Figure 5.5: A comparison between the sample's maximum deformation and the first few zonal harmonics l = 2, 3, 4.

Free-fall

One of the key assumptions is that the sample is undergoing free-fall while oscillating. The position of a randomly-chosen sample's center of mass as a function of time is shown in Fig.5.6. Across all

samples, the sample's vertical position can be expressed as $y = \frac{9.81}{2}t^2$, which proves the sample is indeed undergoing free-fall during the drop-bounce experiment.

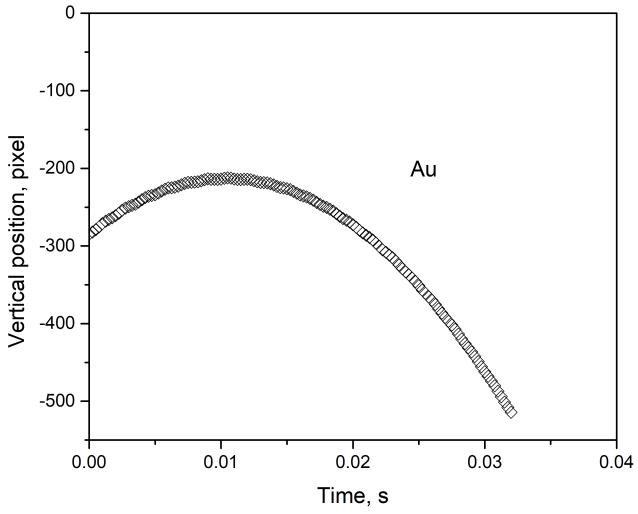

Figure 5.6: Gold sample's position along the vertical direction.

Sample rotation and data selection

For the sample oscillating while traveling upward, rotations along the x, y, z, or a combination of these axes could occur. Because shadowgraphs only record the sample's cross-section on the xz-plane, certain features of the sample cannot be captured. Therefore, it is crucial to understand the effect of sample rotation on the observed oscillation pattern. A series of images of a sample undergoing the l=2 m=0 mode oscillation without any rotation is shown in Fig.5.7, and the oscillation patterns along the z-axis and x-axis are given in Fig.5.8. The oscillation pattern is not a sine wave because I did not generate a simple harmonic oscillation using MATLAB. However, patterns like the ones in Fig.5.8 are enough to compare the oscillation frequencies along different axes. For a non-rotating sample, identical oscillation frequencies can be obtained regardless of whether one uses the

oscillation along the vertical or horizontal axis.

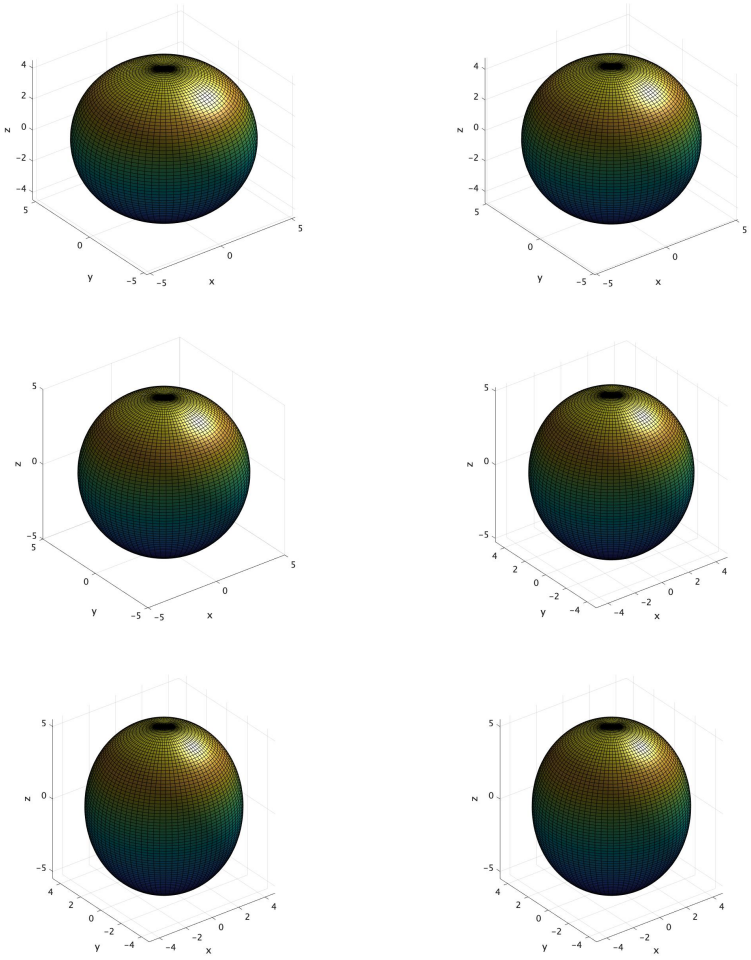

Figure 5.7: Sample oscillating (l=2 m=0) without rotation.

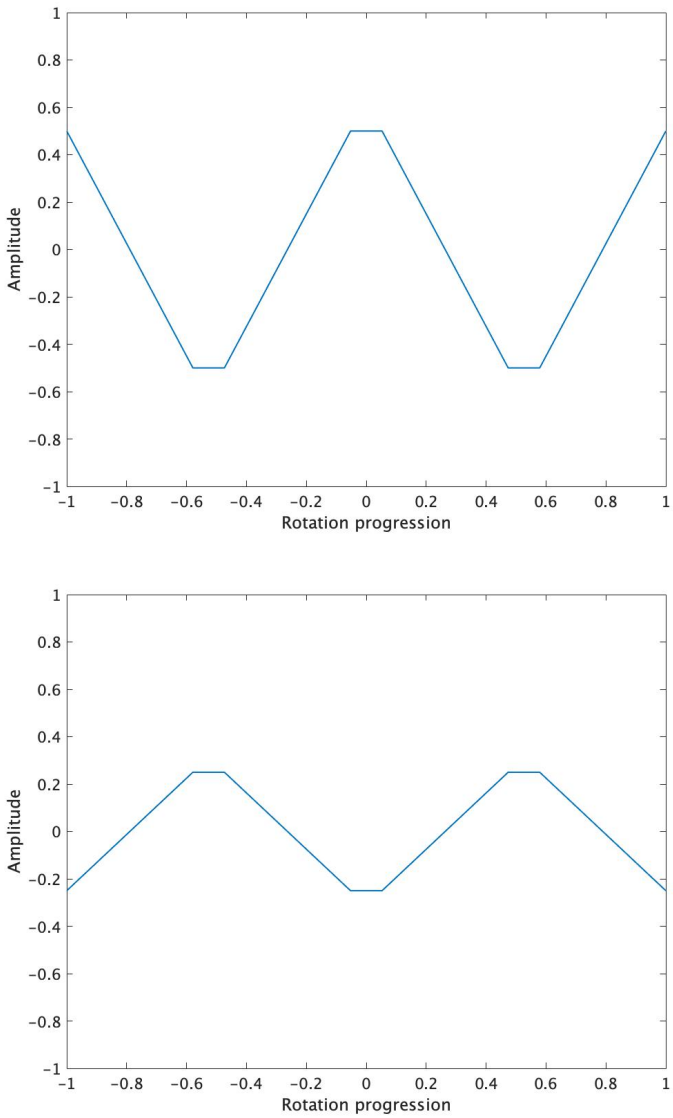

Figure 5.8: Vertical (up) and horizontal (down) oscillation patterns.

Rotation along the x-axis A series of images showing an oscillating sample rotating along the x-axis is given in Fig.5.9. The oscillation patterns plotted using the lengths along the z and x-axis are shown in Fig.5.10. A comparison with Fig.5.8 shows that when the sample oscillates while rotating along the x-axis, only the horizontal axis's oscillation pattern is unaffected.

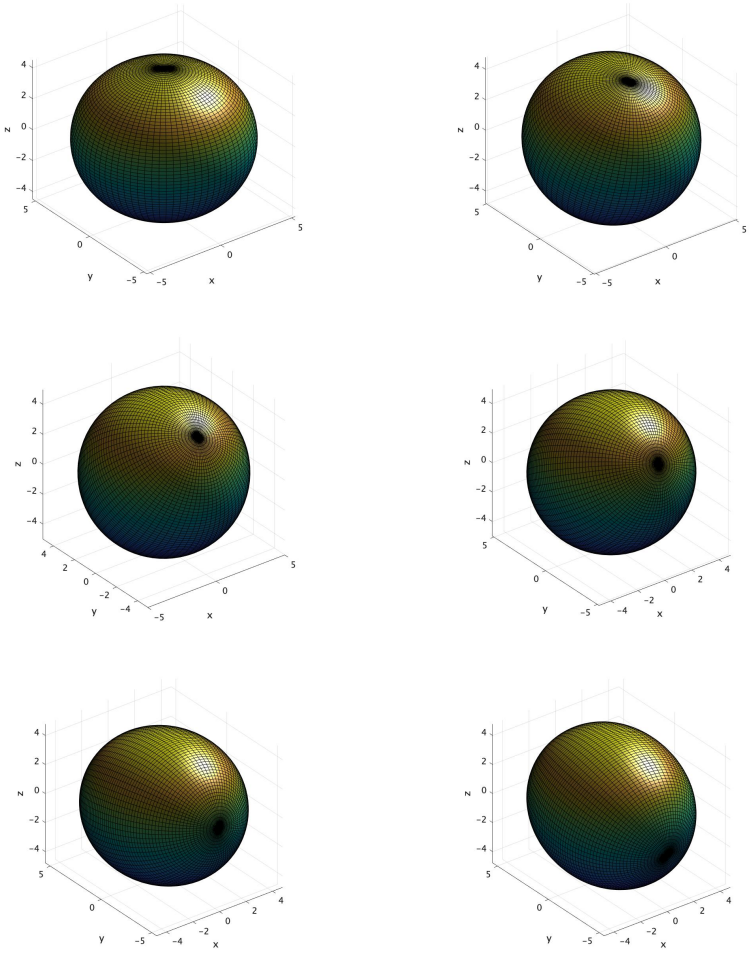

Figure 5.9: Sample oscillating (l=2 m=0) while rotating along the x-axis.

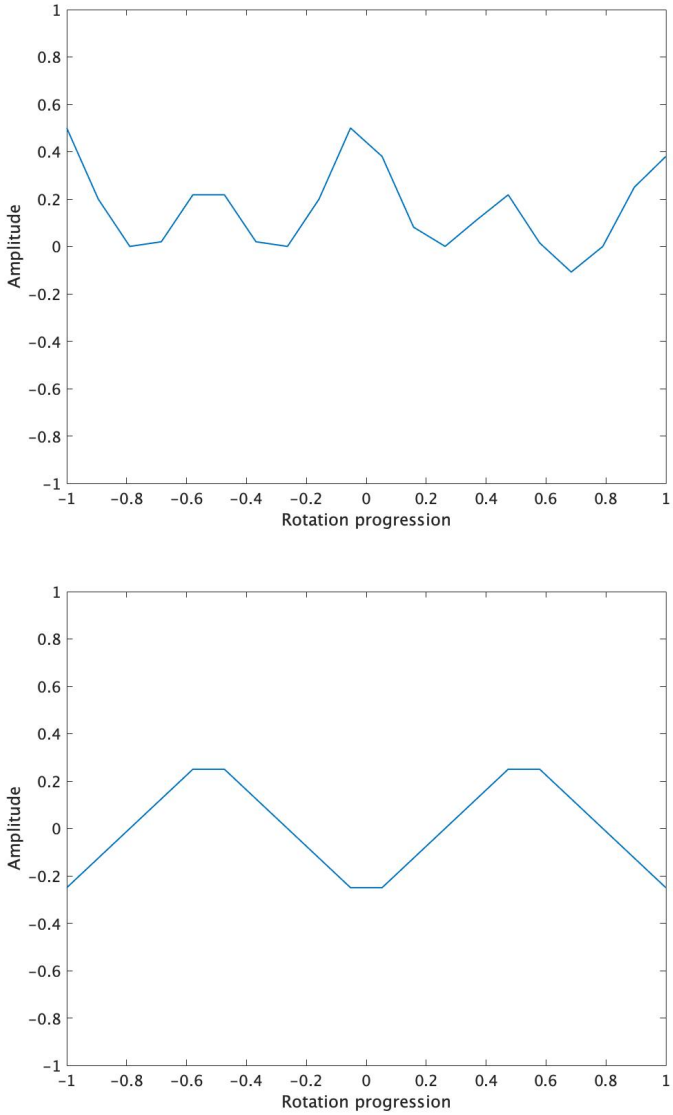

Figure 5.10: Vertical (up) and horizontal (down) oscillation patterns.

Rotation along the y-axis Unlike the rotation along the x-axis, rotation along the y-axis is readily observed from the xz-plane. Images depicting a sample oscillating while rotating along the y-axis are shown in Fig.5.11. When rotation along the y-axis occurs, the data is discarded because the sample's rotation speed is unknown, making it challenging to keep track of the length of the sample's semi-major and semi-minor axis.

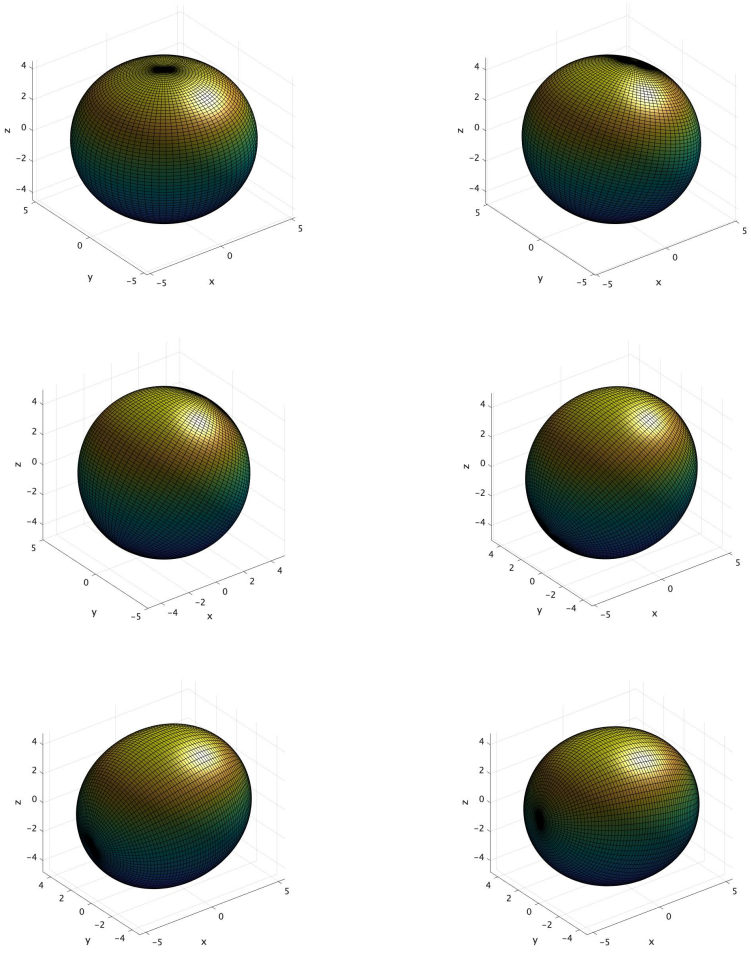

Figure 5.11: Sample oscillating (l=2 m=0) while rotating along the y-axis.

Rotation along the z-axis Images of a sample rotating along the z-axis are shown in Fig.5.12, and the corresponding vertical and horizontal axis's oscillation patterns are shown in Fig.5.13. It is apparent that sample rotation along the z-axis does not affect the obtained vertical and horizontal oscillation patterns.

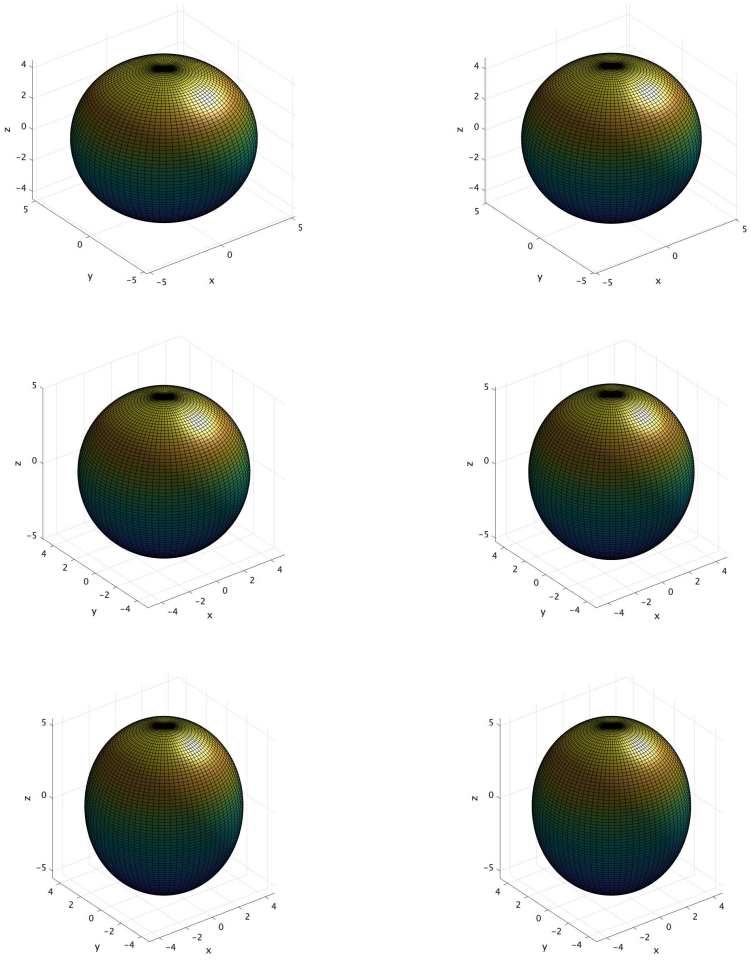

Figure 5.12: Sample oscillating (l=2 m=0) while rotating along the z-axis.

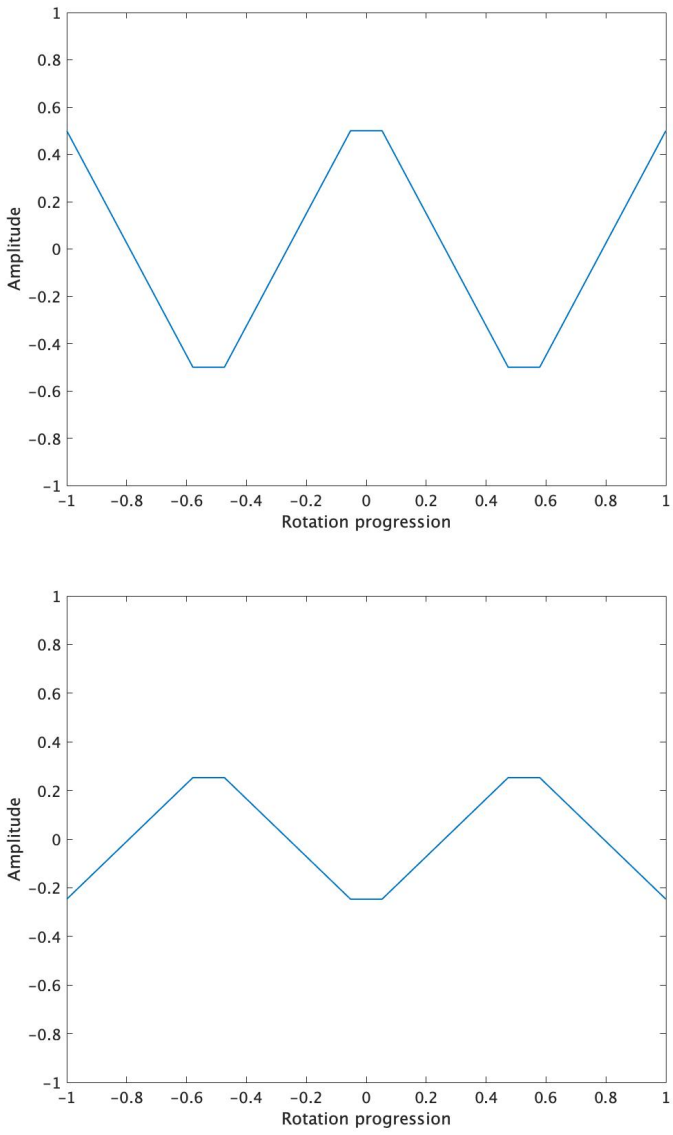

Figure 5.13: Vertical (up) and horizontal (down) oscillation patterns.

The discussion above shows that the sample's oscillation along the horizontal x-axis is the least affected by sample rotation. When sample rotation along the horizontal x-axis occurs, the oscillation pattern of the vertical z-axis becomes unusable. However, the amplitude of the vertical oscillation is always greater than that of the horizontal one, making the Lorentzian curve fitting after FFT more precise.

5.2 Oscillation, surface tension, and viscosity evaluations

After applying an elliptical fitting to the sample's perimeter using DIPP-MACRO II, the sample's horizontal and vertical axis lengths are used to generate an oscillation pattern. **Two types of analysis methods, Fourier transformation or fitting with a damped sine function, were used throughout this work.** The reason for using two different methods is because damping was initially not observed in the oscillation of liquid metals, making FFT alone sufficient to locate the resonant frequency for surface tension calculations. However, when the drop-bounce method is applied to the more viscous liquid Al_2O_3, damping is observed, and fitting with a damped sine function is more appropriate because FFT does not provide the oscillation's damping constant. A comparison between the oscillation patterns of liquid gold and liquid Al_2O_3 is given in Fig.5.14.

Using FFT

Once the sample's oscillation becomes stable and periodic, 128 data points were taken for FFT. The time the sample can stay in free-fall with the current setup is limited, which results in a relatively low spectral resolution in the frequency spectrum. The spectral resolution can be enhanced by recording at a higher fps or extending the free-fall time. These improvements should be considered in future works. Before FFT, a Hamming window is applied to the oscillation pattern to reduce the effect of spectral leakage from windowing. The obtained frequency spectrum is shown in Fig.5.15, and a

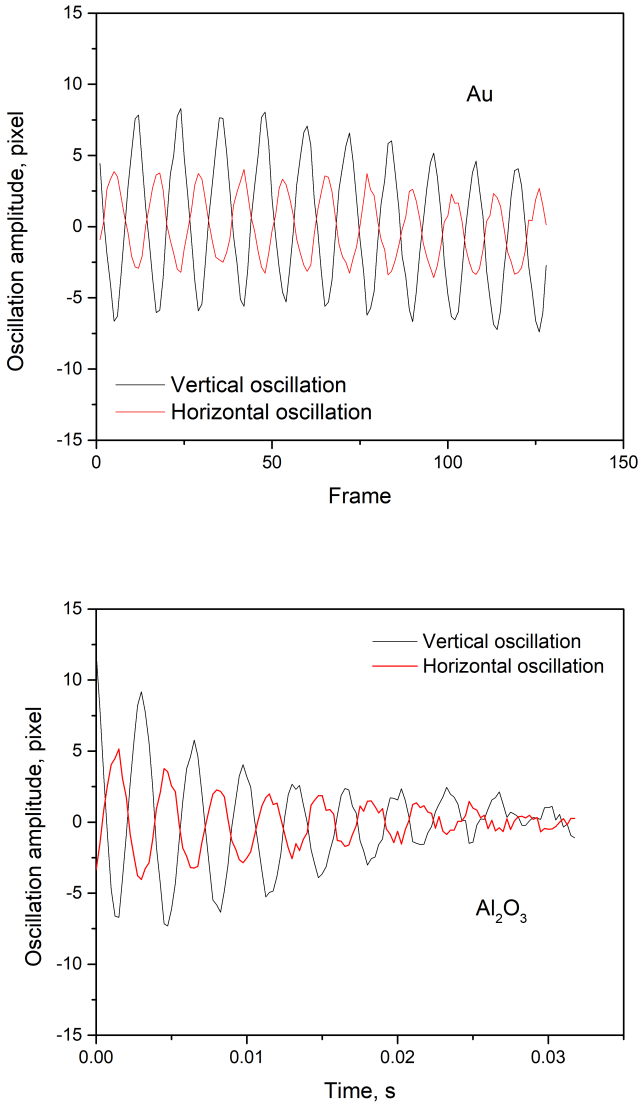

Figure 5.14: Vertical and horizontal oscillation of a liquid gold (upper) and a liquid Al_2O_3 sample (lower).

Lorentzian function is used to locate the resonant frequency peak.

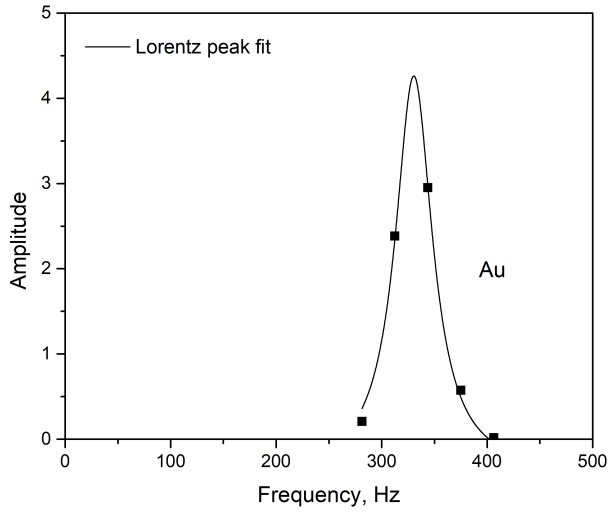

Figure 5.15: Frequency spectrum with Lorentzian peak fitting

Using damped sine function

The weakly-damped oscillation of a viscous liquid like Al_2O_3 is expressed with a sine function:

$$r = r_0 + Ae^{-\frac{t}{\Gamma}} sin(\pi \frac{t - t_c}{\nu_R}) \tag{5.2}$$

During drop-bounce experiments with liquid Al_2O_3, the sample was found to move towards/away from the camera, generating oscillation patterns like the one shown in Fig.5.16. Eqn.5.2 is then modified to eliminate the effect of the sample's movement on the observed oscillation amplitude by incorporating a fitting parameter α:

$$r = (r_0 + \alpha t) + Ae^{-\frac{t}{\Gamma}} sin(\pi \frac{t - t_c}{\nu_R})(\frac{r_0 + \alpha t}{r_0}) \tag{5.3}$$

The oscillation pattern in Fig.5.16 is then corrected using Eqn.5.3, as shown in Fig.5.17.

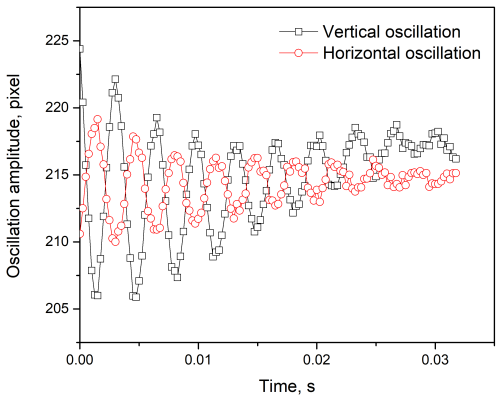

Figure 5.16: Oscillation pattern of a sample moving towards the camera.

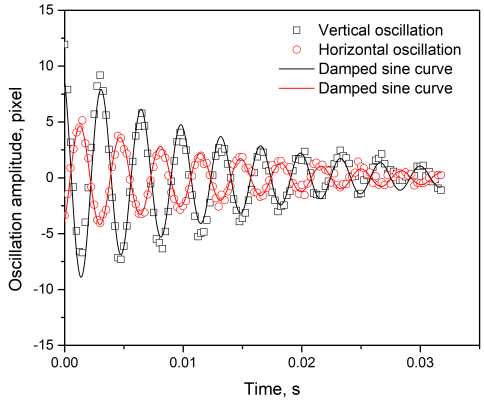

Figure 5.17: Oscillation pattern of a sample moving towards the camera, corrected, then fit with a damped sine curve.

5.3 Surface tension of liquid gold

We used liquid gold in this study because the surface tension of liquid gold has been measured in microgravity by Egry et al.[74] using EML. If the data obtained with the drop-bounce method agrees

with that reported by Egry et al.[74], it can be considered as a reliable surface tension measurement method.

Before the drop-bounce measurement, spherical gold samples (10-20 mg) were made by heating a gold wire (3N5, Nilaco) with a single top fiber laser under argon flow (5N, Air Liquide). The sample's mass was measured before and after the drop-bounce experiment. As expected, negligible mass change was observed because gold is a noble metal. The method for evaluating the uncertainty in the estimated sample's temperature was already discussed in detail in Chapter.3. The uncertainty in the calculated surface tension values comes from the peak fitting process with the Lorentzian peak function. With higher spectral resolution, more data points can be used in peak fitting, which will reduce the standard error of the fitted resonant frequency. The surface tension of liquid gold obtained with the drop-bounce method is compared with previously reported values in Fig.5.18. Liquid gold's surface tension as a linear function of temperature is given in Eqn.5.4.

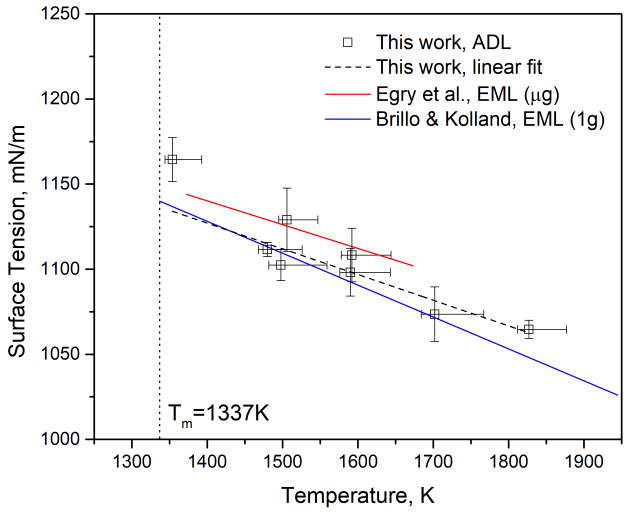

Figure 5.18: Surface tension of liquid gold.

$$\gamma_{Au}(mN/m) = (1138 \pm 61) - (0.15 \pm 0.02) \times (T - 1337) \tag{5.4}$$

The data obtained in this work are in excellent accord with those reported by Egry et al.[74] and Brillo & Kolland[146]. It is worth mentioning that Egry et al.[74] conducted the oscillating drop experiment using EML in space, and resonant frequency splitting (loss of degeneracy) was not observed in their data. Therefore, Egry et al. could use Rayleigh's equation to provide the true surface tension of liquid gold without further assumptions or corrections. By comparing Eqn.5.4 to the one reported by Egry et al.[74], a maximum deviation of only 1.7% from 1354 K to 1827K was found. This agreement shows the reliability of the drop-bounce method in surface tension measurements. In addition, it proves that the oscillation behavior of a droplet under microgravity was successfully replicated with the drop-bounce method on the ground.

5.4 Surface tension and viscosity of liquid alumina

In the previous section, the drop-bounce method was established as a reliable technique for surface tension measurements. However, one should keep in mind that ADL's advantage over ESL and EML is its ability to levitate liquid oxides, not metals. Therefore, investigations on the properties of liquid oxides should be the primary goal of this study. In addition, liquid gold's low viscosity made it impossible to observe any oscillation damping during the sample's free-fall. Molten oxides such as Al_2O_3 are more viscous and are good candidates for investigating whether viscosity can be evaluated using the drop-bounce method. Therefore, in this section, the drop-bounce method is used to measure both the surface tension and viscosity of liquid Al_2O_3.

The Al_2O_3 samples were fabricated by spark plasma sintering cold-pressed Al_2O_3 (4N, Kojundo Chemical) pellets at 1623K, 100 MPa, and under argon flow (6N, Air Liquide). Before the drop-bounce experiment, the samples are crushed into small chunks (5-10 mg) and made into spheres by

heating with a CO_2 laser (Coherent, 10.6 μm, 100 W). Details on the ADL and splittable nozzle setups were given in previous chapters. For liquid oxides, a 100W CO_2 laser (10.6 μm, Coherent) is used to heat the sample, and temperature measurement is done with a 0.9 μm pyrometer (IR-CAS8CNL, CHINO). A data logger (midi LOGGER GL240, Graphtec) records the pyrometer's signal every 10 ms. A 365 nm bandpass filter (Thorlabs) is used with a 365 nm LED-UV background light (LC-L1 V5, Hamamatsu) to take the sample's shadowgraphs. Shadowgraphs were recorded at 4000 fps with a 1024×928 resolution. The high-speed camera (MEMRECAM HX-7s, nac Image Technology) is equipped with a telecentric lens (1.0X, 2/3", Gold TL, Edmund) to correct parallax errors. Both argon (6N, Air Liquide) and oxygen (3N up Taiyo Nippon Sanso) gases (7:3 flow rate) are used in the levitation to prevent metal oxides from reduction upon heating. The sample's mass was measured before and after the experiment, with negligible changes observed.

Timelapse images of an oscillating liquid Al_2O_3 sample are shown in Fig.5.19. The oscillation pattern along the sample's horizontal axis is plotted in Fig.5.20, and Eqn.5.2 is used in the fitting of this damped oscillation pattern. The oscillation damping constant and resonant frequency can be extracted directly from Eqn.5.2 and used in surface tension and viscosity calculations.

The method for estimating the sample's temperature during the drop-bounce period was already given in Chapter.3, along with a discussion on this method's maximum uncertainty. The uncertainty in the calculated surface tension and viscosity arises from the curve fitting process using Eqn.5.2. The standard errors of the fitted resonant frequency and damping constant for each sample are used to express the uncertainties in the surface tension and viscosity results. The temperature dependences of liquid Al_2O_3's surface tension and viscosity are shown in Figs.5.21 and 5.22.

The surface tension of liquid Al_2O_3 obtained in this study is in good agreement with values in literature, especially with those obtained using levitation techniques[45,62,97]. As shown in Fig.5.21, deviations in the measured surface tension data between levitation techniques and traditional contact methods[147–149] increase with increasing temperature. Because sample-container contamina-

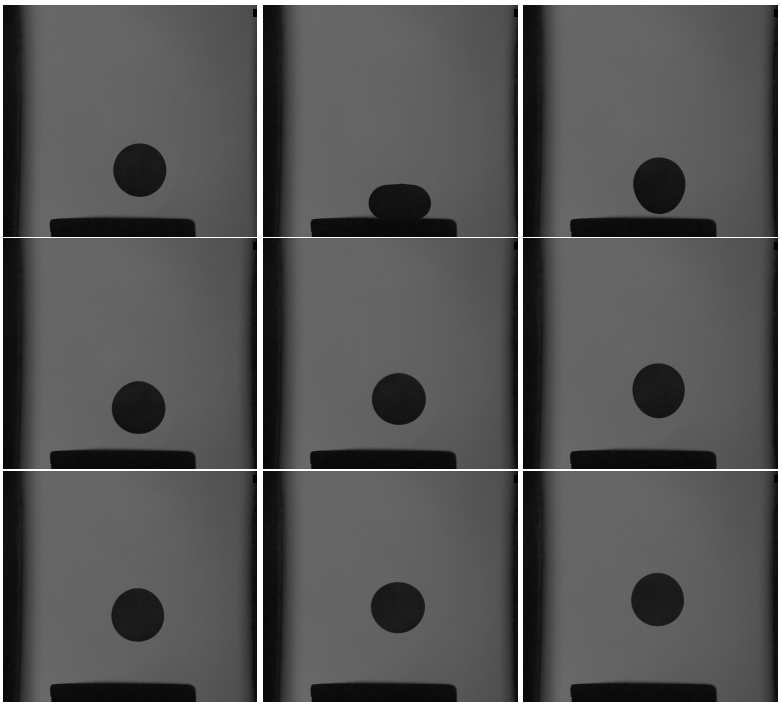

Figure 5.19: Timelapse images of an oscillating liquid Al_2O_3 sample.

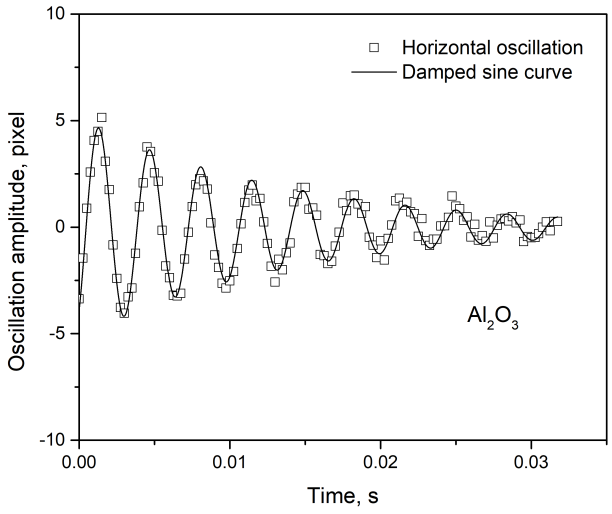

Figure 5.20: Damped oscillation of a liquid Al_2O_3 sample along its horizontal axis.

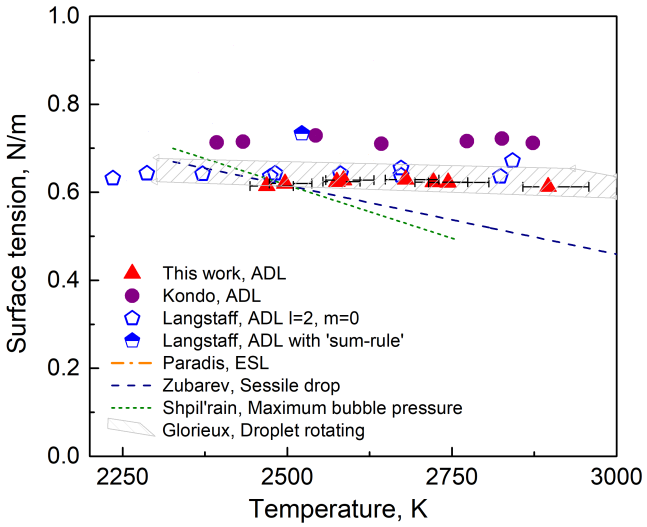

Figure 5.21: Surface tension of liquid Al_2O_3

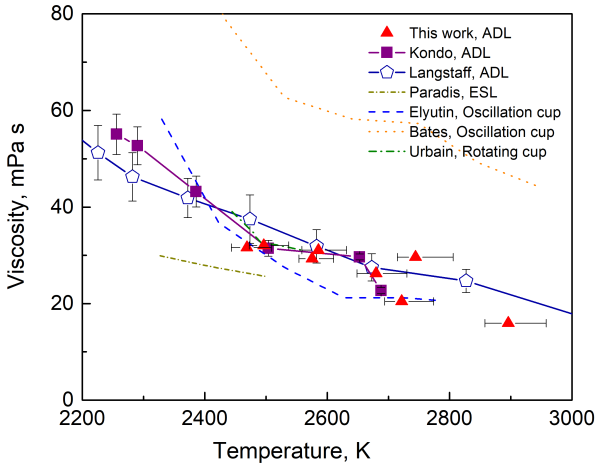

Figure 5.22: Viscosity of liquid Al_2O_3

tion does not occur during levitation, the surface tension data reported using levitation techniques should be more reliable. Similarly, this deviation can also be seen in the reported viscosity of liquid Al_2O_3. Furthermore, the data reported by levitation methods have better reproducibility than that of contact methods. For example, with the same oscillating cup method, the viscosity data reported by Bates et al.[150] is almost twice larger than that reported by Elyutin et al.[151]. The viscosity of liquid Al_2O_3 obtained in this study is in accord with values obtained using ADL by Kondo et al.[44] and Langstaff et al.[62]. Overall, the viscosity data obtained by ADL is slightly higher than that by ESL[97], and the reason for this mismatch is currently unknown. As mentioned in the introduction, ADL and ESL are generally used to levitate oxides and metals, respectively. Therefore, it is difficult to find materials that have been studied using both methods to compare the reported viscosity data.

5.5 On the necessity of a 'sum-rule' for surface tension measurements

From Fig.5.21 in the previous section, one might notice that the surface tension obtained with the drop-bounce method is in excellent agreement with that reported by Langstaff et al.[62]. Langstaff et al.[62] calculated the surface tension of liquid $Al2_2O_3$ in two ways. First, they calculated surface tension using the resonant frequency of the l=2 m=0 mode while ignoring the other resonant frequencies (l=2 m=$\pm$1, $\pm$2). Theoretically, this approach is incorrect for ground-based oscillating drop experiments. In addition, although they performed the oscillating drop experiment with ADL, they applied the 'sum-rule'[72] for EML in interpreting the frequency spectrum. The reasoning for using EML's 'sum-rule' is to qualitatively understand how the split in the l=2 mode's resonant frequencies can affect the calculated surface tension.

In section.5.1, I have already explained how the drop-bounce method allows the sample to oscillate in free-fall, and thus the resonant frequency's degeneracy is not lost (l=2 m=0, $\pm$1, $\pm$2 oscillation modes have the same resonant frequency). Interestingly, in Fig.5.21, the surface tension

obtained with the drop-bounce method agrees well with that reported by Langstaff et al.[62], while using only the l=2 m=0 mode's resonant frequency in Rayleigh's equation. To further confirm that the oscillation induced with the drop-bounce method is identical to that under microgravity, Assist. Prof. Duan and Assoc. Prof. Yamaji helped conduct CFD simulations on a pseudo-Al_2O_3 droplet. The properties of this pseudo-Al_2O_3 droplet and the surrounding environment used in CFD simulation are listed in Tab.5.1. The simulated droplet was given an impact velocity of 0.4 m/s when it makes contact with the bottom boundary and an acceleration of 9.8 m/s^2 to replicate the condition of the drop-bounce experiment. The droplet's diameter prior to hitting the bottom boundary was set to 2.2 mm. The freely-levitated droplet was introduced as a spheroid (major axis 2.6 mm, minor axis 2.0 mm) so that sample oscillation would naturally occur when the simulation started. The interface between the droplet and air is calculated with the front tracking method, and the curvature of the interface is related to the droplet's surface tension. In this work, a 10 mm by 10 mm by 10 mm boundary with a mesh size of 0.083 mm was used. The PARIS (PArallel, Robust, Interface Simulator) software used in the simulation is well documented by Aniszewski et al.[152]. Timelapse images of the simulation results for the two cases are shown in Figs.5.23 and 5.24.

Table 5.1: Parameters used in the CFD simulation.

Properties	Air	Droplet (drop-bounce)	Droplet (microgravity)
Density, $kg \cdot m^{-3}$	1.2	2900	2900
Viscosity, $Pa \cdot s$	1.9×10^{-5}	0.045	0.045
Surface tension, $N \cdot m^{-1}$	-	0.65	0.65
Initial diameter, mm	-	2.2	2a = 2.6, 2c = 2.0
Impact velocity, $m \cdot s^{-1}$	-	0.4	-
Acceleration, $m \cdot s^{-2}$	-	9.8	-

The droplet's oscillations along its x, y, and z-axis are shown in Fig.5.25. The simulated droplet's l=2 mode's oscillation frequency, calculated surface tension, and viscosity values are listed in Tab.5.2. In both simulations, no external forces interacted with the droplet during oscillation, which means

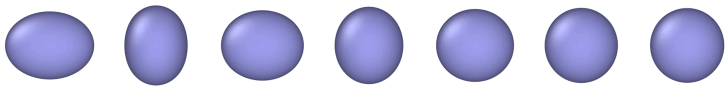

Figure 5.23: Freely-oscillating droplet, CFD simulation

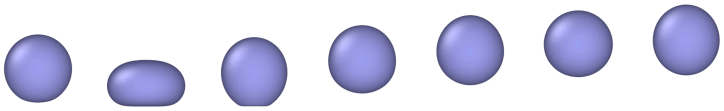

Figure 5.24: Drop-bounce, CFD simulation

resonant frequency splitting will not occur. The surface tension and viscosity were calculated using Eqns.2.9 and 2.10. Only a maximum deviation of 0.7% is observed in the calculated resonant frequency and surface tension between the two cases. For viscosity, a slightly larger deviation of 1.5% is observed. Back in section.5.3, it was already shown that the surface tension of liquid gold obtained with the drop-bounce method is in agreement with data taken in microgravity. These simulation results further confirm that the sample's oscillation behavior induced during the drop-bounce experiment can be considered identical to that of the l=2 mode under microgravity conditions.

Table 5.2: Simulated pseudo-Al_2O_3 droplet's resonant frequency ν_R (Hz), surface tension σ (N·m^{-1}), and viscosity η (Pa·s).

	x-axis			y-axis			z-axis		
	ν_R	σ	η	ν_R	σ	η	ν_R	σ	η
Freely-oscillating	182	0.629	0.0419	182	0.629	0.0414	183	0.632	0.0418
Drop-bounce	183	0.633	0.0413	183	0.634	0.0417	183	0.633	0.0412

As mentioned at the beginning of this section, the surface tension of liquid Al_2O_3 reported by Langstaff et al.[62], while only considering the l=2 m=0 mode's resonant frequency, agrees with that

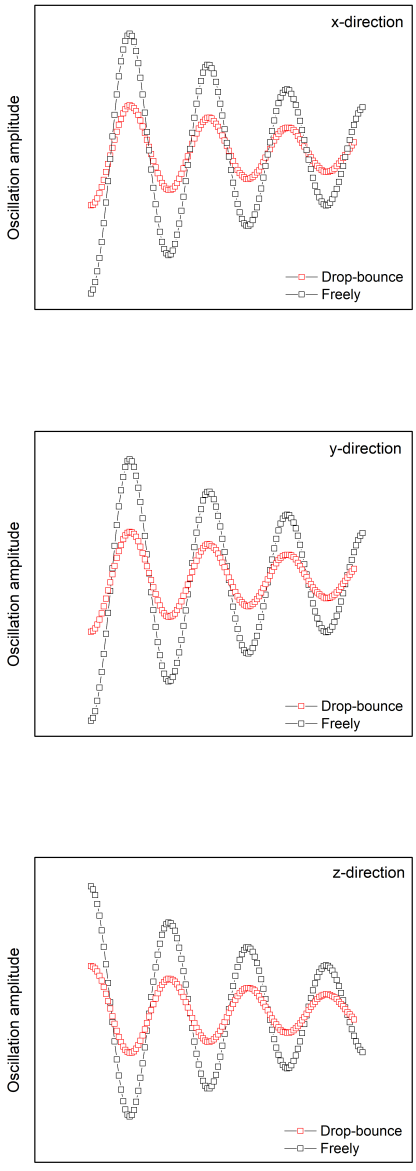

Figure 5.25: Oscillation along the x, y, and z-axis.

obtained using the drop-bounce method. Further, the oscillation induced by the drop-bounce method can be considered identical to the l=2 mode oscillation under microgravity, based on experiment and simulation results. These results suggest that unlike the case for EML where surface tension calculation without the 'sum-rule' can result in an underestimation of about 20-30%[62], this deviation is almost negligible for ADL. However, to theoretically explain how to re-calculate the degenerate resonant frequency based on those of the l=2 m=0, $\pm$1, $\pm$2 modes, one still needs a 'sum-rule' like the one for EML. In other words, until the force distribution on an aerodynamically levitated sample can be clarified, the resonant frequency of the l=2 m=0 mode obtained from oscillating drop experiments with ADL can be used to produce accurate surface tension values. This is a reasonable conclusion because resonant frequency splitting is caused by the sample's deformation and rotation. Compared to samples levitated with ground-based EML, those levitated with ADL are far less deformed. In addition, samples are only rotating at a rate of a few Hz during ADL experiments, far slower than the samples levitated with ESL.

6

Density measurement (ADL-drop method)

Unlike that in ESL and EML, a sample levitated with ADL is not fully visible to the high-speed camera because the sample's bottom part is hidden in the levitation nozzle. The common assumption in density measurements with ADL is to assume the sample's bottom is not deformed by the levitation gas[46–48]. However, it is impossible to clarify the uncertainty introduced in the calculated density with this assumption as long as the sample is partially hidden.

The ADL-drop method introduced in this chapter uses a splittable nozzle design to drop the sample after reaching the target temperature. After the nozzle splits, the free-falling sample is completely visible to the high-speed camera during density measurements. The fully-visible sample allows one to determine whether sample deformation took place and accurately fit its perimeter. This chapter discusses the measurement procedure, possible uncertainties, and the obtained density values of liquid platinum.

6.1 Measurement setup

For a detailed description of the ADL setup and imaging technique used in this study, please refer to Chapter.3. In this chapter, only a summary of the apparatus' specifications is provided. The platinum samples used in this study were fabricated by melting platinum wires (Nilaco, 3N8) with a fiber laser (976 nm, Pearl). The orifice of the conical levitation nozzle used has a semiangle of 30°C and is 1.4 mm in diameter. Because a boron nitride platform is placed underneath the splittable nozzle to catch the solidified sample, only the top fiber laser is used for heating during density measurements. Ar-4%H_2 mixture gas (Air Liquide) was used to levitate the sample. The temperature of the sample is monitored using a pyrometer operating at a wavelength of 1.55 μm, equipped with a longpass filter at 1400 nm (Thorlabs) to reduce the noise from the reflected lasers. The pyrometer's signal was recorded every 1ms with a data logger (GL900, Graphtec). 1024 by 928 shadowgraphs were taken at a rate of 4000 fps with a high-speed camera (MEMRECAM HX-7s, nac Image Technology). A white light (SLA-100B, OptoSigma) and a 465 nm bandpass filter (Thorlabs) were used to create the shadowgraphs.

6.2 Results and discussion

6.2.1 Data points used for fitting

The DIPP-MACRO II software conducts elliptical fitting using a selection of points on the edge of the sample. These points are equally-spaced at a predetermined angle from one another, and therefore the number of points used in fitting will affect the obtained length of the major and minor axis. Elliptical fittings were performed on a free-falling stainless steel ball to investigate this effect, using 360, 120, 36, 12, and 6 edge points, respectively. The results are shown in Fig.6.1 and Tab.6.1.

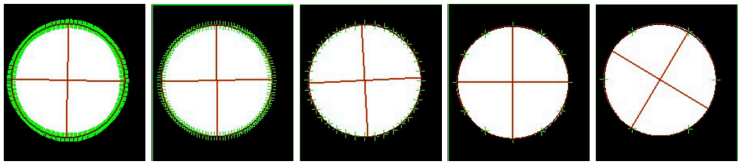

Figure 6.1: Sample's perimeter fitting using different numbers of edge points. From left to right: 360, 120, 36, 12, 6.

	Major axis		Minor axis	
	Average	Standard deviation	Average	Standard deviation
360 points	141.8	0.05	141.4	0.10
120 points	141.9	0.08	141.4	0.09
36 points	141.9	0.12	141.3	0.14
12 points	141.9	0.26	141.2	0.16
6 points	142.0	0.38	141.1	0.36

Table 6.1: Elliptical fitting results with different numbers of edge points of the same stainless steel sample.

Although a minimum of four edge points, 90° apart, and a center point are enough to determine a unique ellipse, more should be used for perimeter fitting to minimize the noise from edge detection. Indeed, in Tab.6.1, a decrease in the standard deviation of the obtained axis lengths can be observed as an increasing number of points are incorporated in the fitting. With a greater number

of edge points used in the fitting, the average lengths of the major and minor axis also began to converge. Since the solid stainless steel ball used is close to a perfect sphere, this convergence suggests an improvement in the elliptical fitting's accuracy with the number of edge points used. Therefore, 360 edge points (the maximum amount allowed) are used in the density measurements in this study.

6.2.2 Adjusting the camera's focus and calibration

Prior to density measurements, the camera's focus must be adjusted, which requires a stationary sample, generally a SUS or ZrO_2 ball, placed on the boron nitride platform. It is critical that the location of the sphere used for adjusting the camera's focus be identical to that of a dropped sample during density measurements. Therefore, a SUS ball is first levitated and then dropped onto the boron nitride plate. After focus adjustment, shadowgraphs of the stationary sample with a known radius are taken for pixel-to-millimeter conversion. In this work, five stainless steel balls with different diameters (from 1.5 to 3.5 mm) were stably levitated and then dropped. Shadowgraphs of the final ten frames before the sample hits the boron nitride platform were used for unit conversion, and the results are shown in Fig.6.2. The last ten frames were used so the uncertainty in the conversion can be evaluated. As expected, Fig.6.2 shows that pixel is linearly related to the actual distance in millimeter. During the ADL-drop density measurement process, shadowgraphs of the sample are taken as the sample free-falls. The last ten frames before the sample hits the boron nitride platform are used to calculate the sample's volume during density measurements because the pixel-to-millimeter conversion process is conducted within the same region.

6.2.3 Measured density of liquid platinum

Unlike solids, molten samples could be deformed by the levitation gas and even oscillate during its free-fall. If deformation or oscillation can cause the sample's shape to deviate from a spheroid,

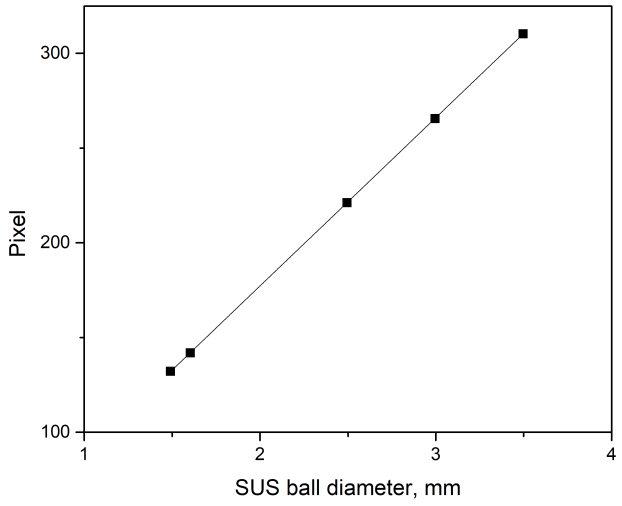

Figure 6.2: Relationship between the measured pixels and the sample's actual diameter

performing elliptical fitting while assuming the sample's cross-section is still an ellipse will introduce additional uncertainties. The following rules are therefore applied to standardize the data selection process:

- Data containing sample oscillations or rotations not along the z-axis are discarded.
- The falling sample is assumed to be axisymmetrically rotating along the z-axis. The gas pressure surrounding a levitated sample in a nozzle was simulated using COMSOL and is shown in Fig.6.3. Because of the higher pressure at the bottom of the sample, it should deform into an oblate spheroid. Therefore, the sample's horizontal axis must be longer than its vertical one. The data is discarded if otherwise.
- A single exception exists to the second rule. If the sample's vertical axis is longer than its horizontal one by less than 1%, the sample is considered as a sphere, and the data is usable.

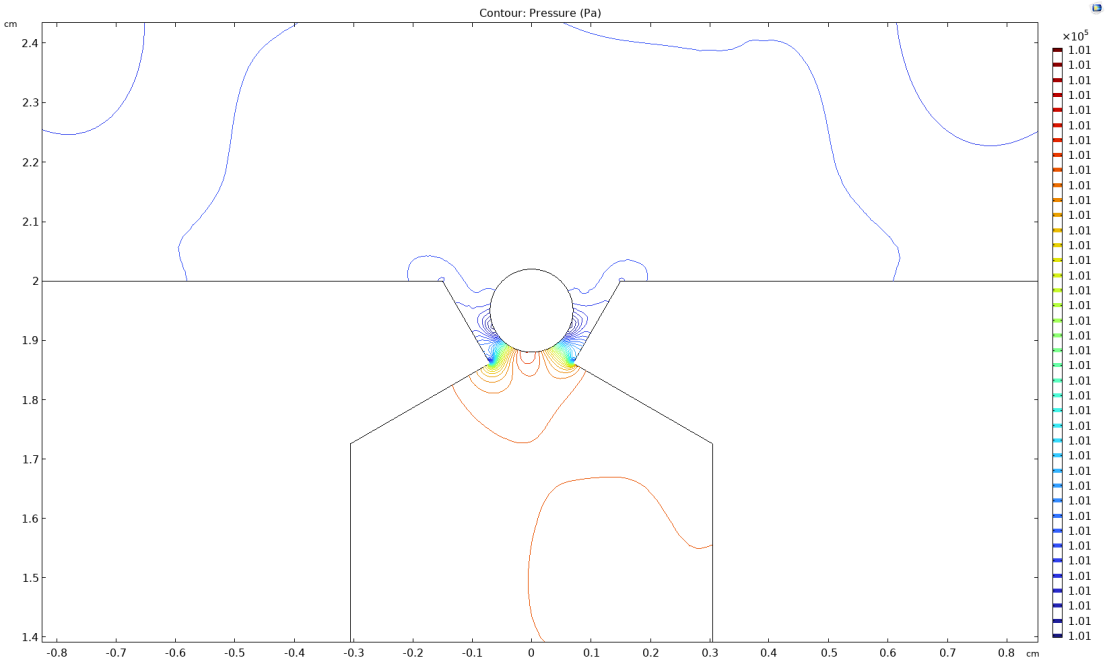

Figure 6.3: Simulated pressure field around a levitated sample within a conical nozzle

While the sample is falling, its temperature was extrapolated using the method described in section.3.3. The last ten frames before the sample hits the boron nitride platform are used for density calculations. The sample's density is calculated for each of the ten frames and is assumed to be temperature-independent. These ten density values are used to express the uncertainty in the reported density for each measurement. An image combining all ten shadowgraphs of a falling liquid platinum sample is shown in Fig.6.4. The obtained density data of liquid platinum are shown in Fig.6.5 and Tab.6.2 along with reference data. In Tab.6.2, density is expressed as:

$$\rho = \rho_{Tm} + \frac{d\rho}{dt}(T - T_m) \tag{6.1}$$

The liquid platinum's density data obtained in this study are in good agreement with reference values, confirming the validity and reliability of the ADL-drop method. Liquid platinum density's

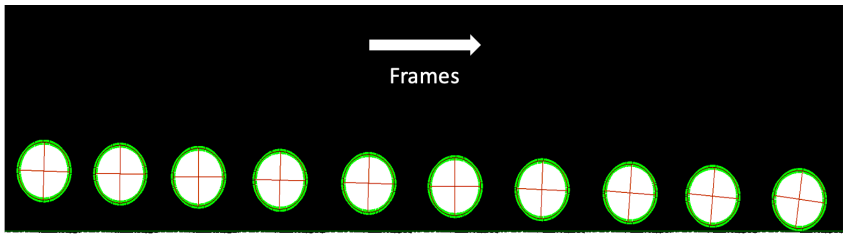

Figure 6.4: Image of a falling liquid platinum sample during density measurement.

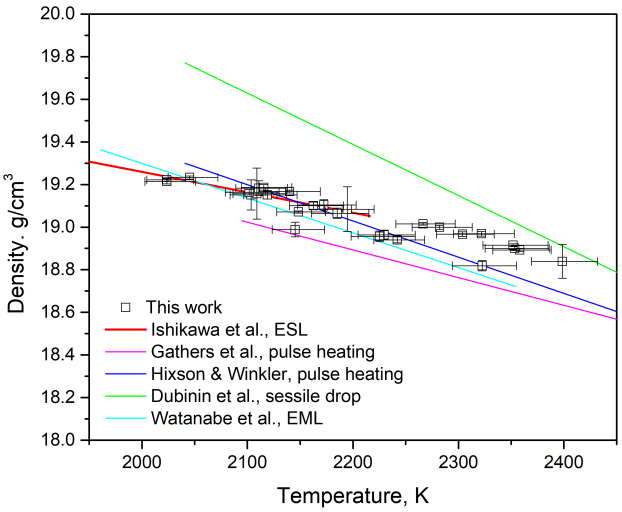

Figure 6.5: Liquid platinum's density obtained in this study and reference values.

Range, K	ρ_{Tm}, g· cm^{-3}	$d\rho/dt$, mg·cm^{-3}K^{-1}	Reference
2023-2399	19.32	-1.06	This study, ADL
1961-2354	19.23	-1.63	Watanabe et al.[153], EML
1691-2216	19.22	-0.96	Ishikawa et al.[2], ESL
2041-2473	19.77	-2.4	Dubinin et al.[154], sessile drop
2041-5100	19.3	-1.7	Hixson & Winkler[141], pulse heating
2095-4500	19.1	-1.3	Gathers et al.[155], pulse heating

Table 6.2: Liquid platinum's density at the melting point and its temperature coefficient obtained in this study with reference values.

temperature-dependency obtained in this work is between the values reported by Ishikawa et al.[2] and Watanabe et al.[153]. At its melting point 1941 K, liquid platinum's density is measured at 19.32 g/cm^3 with ADL, roughly 0.5% higher than previously reported values with ESL and EML. Dubinin et al.[154] reported a density data of 19.77 g/cm^3 at the melting point, which is higher than the rest of the reference values (19.2 - 19.3 g/cm^3). As Dubinin et al. is the only one to use a contact method, sample contamination could be the reason for this deviation. Although the pulse-heating method used by Gathers et al.[155] is technically a contact method, the measurement finishes under a few microseconds, effectively preventing sample contamination.

7

Conclusion

Levitation techniques, such as ESL, EML, and ADL, provide a way to handle high-temperature liquids while avoiding direct contact. Based on their operating principles and conditions, ESL and EML are used for liquid metals, while ADL is generally used for liquid oxides. Among these three methods, the development of precise measurement methods for ADL has been slow. Although there are ADL-related studies on density, heat capacity, and surface tension measurements, ques-

tionable assumptions on the sample's shape, heat loss, oscillation behavior have been made. After the 1F accident, there was an increasing interest in using levitation techniques to measure the properties of molten core materials. Uranium, zirconium oxides with extremely high melting points are some of the major components of these molten core materials and can only be levitated with ADL. This work's motivation is then to design reliable measurement methods that can be used with ADL to evaluate the thermophysical properties of molten oxides. This dissertation focused on four essential thermophysical properties: density, heat capacity, surface tension, and viscosity.

For heat capacity measurements, the primary issue is that no heat loss model for a sample levitated with ADL is available. This work started with the basic Newton-Stefan heat loss equation to describe the sample's convective and radiative heat loss during levitation. The heat transfer coefficient is expressed using the Ranz-Marshall correlation and modified with an empirical constant α. Mathematically, the sample's heat capacity and emissivity can be solved using two cooling curves obtained by cooling the same sample with two types of levitation gases. Therefore, this method is named the multiple-gas cooling method. The heat capacity values of various liquid transition metals are reported in this dissertation using the multiple-gas cooling method, all in good agreement with those in the literature. In addition, it is possible to measure the heat of fusion of liquids with ADL by establishing a relationship between the sample's undercooling and thermal arrest time. However, it is currently unclear what factors, e.g., flow rate, density, or nozzle shape, affect the empirical constant α used to modify the convective heat loss term. Further controlled experiments to clarify the origin of this parameter should be conducted in the future.

Furthermore, this work introduced the drop-bounce method for surface tension and viscosity measurements, using a splittable nozzle setup and a bouncing platform. The stably levitated sample is dropped, bounces from the platform, and oscillates during free-fall. Past ADL studies have directly used Rayleigh's equation in surface tension calculations, which is only valid under microgravity conditions. With the drop-bounce method, the force-free oscillation induced under micro-

gravity can be replicated on the ground, which justifies the use of Rayleigh's equation in this study. The surface tension of liquid gold obtained in this work is in accord with the data taken in space, proving the drop-bounce method's reliability in surface tension evaluations. In addition, results from CFD simulations showed that the oscillation of a freely-levitated sample could be considered identical to that induced with the drop-bounce method. Finally, the surface tension data of liquid alumina obtained in this work and that from previous ADL oscillating drop studies are compared. Based on this comparison, I concluded that for oscillating drop experiments with ADL, using only the l=2 m=0 mode's resonant frequency in surface tension calculations gives a reasonably accurate estimation.

Finally, to measure density, past researchers have used normal nozzles where the sample is only partially visible to the camera. This work uses the splittable nozzle to drop the sample after stable levitation is achieved. While the sample is undergoing free-fall, its entire cross-section is visible to the high-speed camera, allowing accurate calculation of its volume. Compared to previous studies, the ADL-drop method for density measurement introduced here does not make any assumptions on the sample's shape or degree of deformation during levitation.

To sum up, although new measurement methods that can be used to study the thermophysical properties of molten oxides for ADL are introduced in this work, most of the materials used during these development processes are noble metals like gold or chemically-stable oxides like alumina. When dealing with molten core oxides like UO_2 or ZrO_2, issues such as sample evaporation, radiation, as well as other unforeseen factors will require continuous improvements in the design of the levitation chamber and measurement techniques.

A

Comprising papers

Peer-reviewed papers

- Yifan Sun, Hiroaki Muta, and Yuji Ohishi, *Multiple-gas cooling method for constant-pressure heat capacity measurement of liquid metals using aerodynamic levitator*, Rev. Sci. Instrum., 92, 095102 (2021)
  DOI: https://doi.org/10.1063/5.0055555

- Yifan Sun, Hiroaki Muta, and Yuji Ohishi, *Novel Method for Surface Tension Measurement: the Drop-Bounce Method*, Microgravity Sci. Technol., 33, 32 (2021).
  DOI:https://doi.org/10.1007/s12217-021-09883-7

- Yuji Ohishi, Kouta Kurokawa, Yifan Sun, and Hiroaki Muta, *Thermophysical properties of molten $Zr_{1-x}O_x$ (x=0.1, 0.2) measured by electrostatic levitation*, J. Nucl. Mater., 528, 151873 (2020).
  DOI:https://doi.org/10.1016/j.jnucmat.2019.151873

Under review/In submission

- Yifan Sun, Guangtao Duan, Akifumi Yamaji, Tomoya Takatani, Hiroaki Muta, Yuji Ohishi, *Ground-based ADL replicates microgravity condition for surface tension and viscosity measurements: a study on molten Al_2O_3*, npj Microgravity.

- Yifan Sun, Hiroaki Muta, Yuji Ohishi, *Heat Capacity of Liquid Transition Metals Obtained with Aerodynamic Levitation*, J. Chem. Thermodyn.

B

Liquid metals' cooling curves used in heat capacity measurements

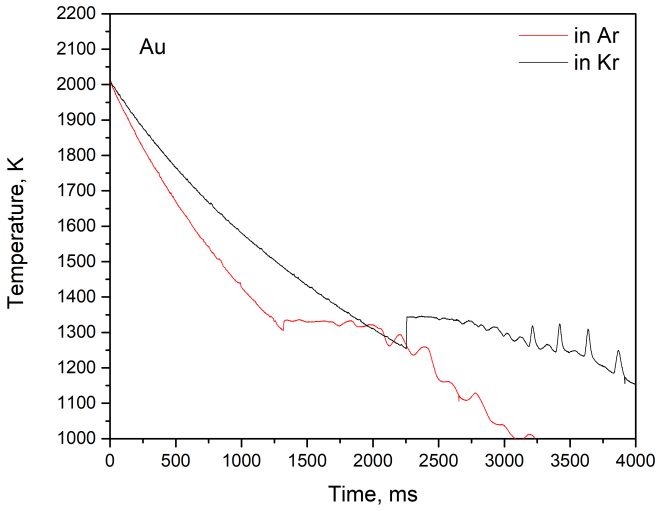

Figure B.1: Cooling curves of liquid Au.

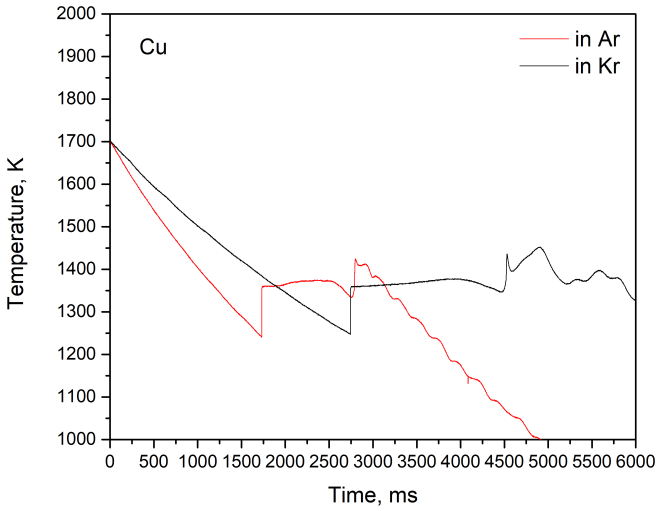

Figure B.2: Cooling curves of liquid Cu.

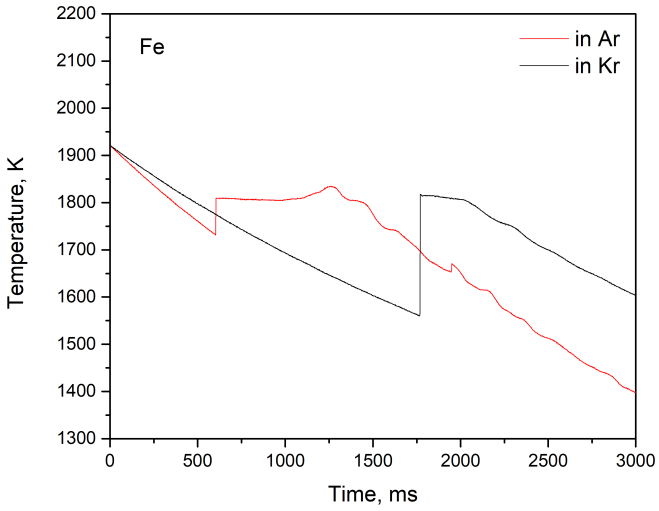

Figure B.3: Cooling curves of liquid Fe.

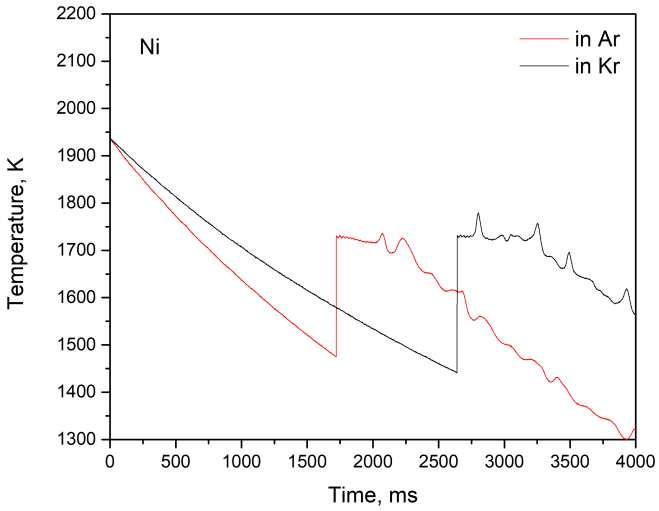

Figure B.4: Cooling curves of liquid Ni.

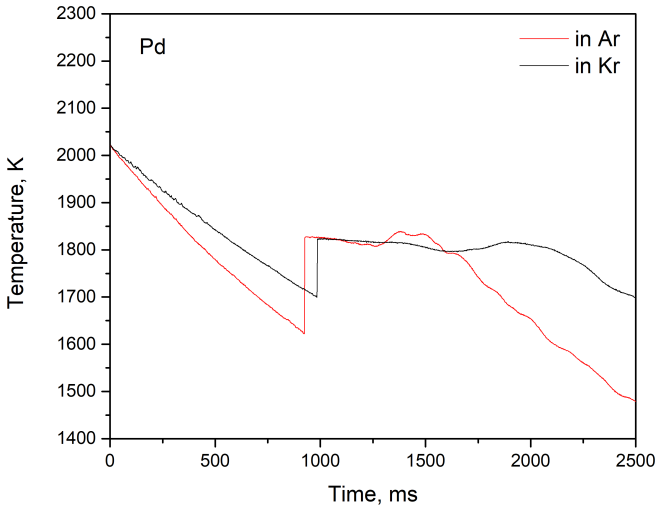

Figure B.5: Cooling curves of liquid Pd.

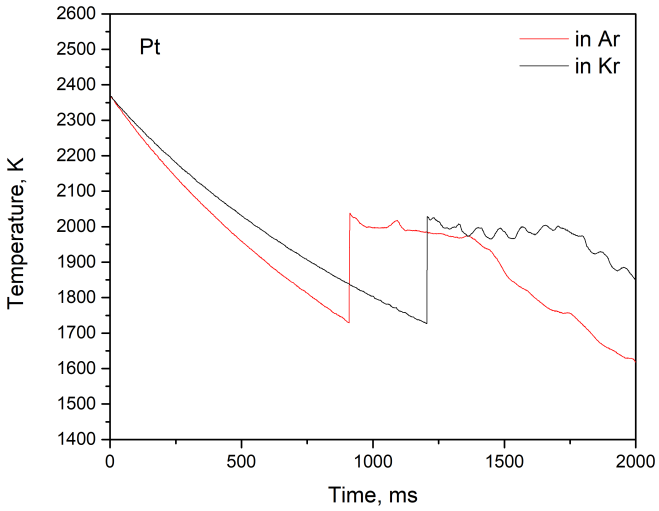

Figure B.6: Cooling curves of liquid Pt.

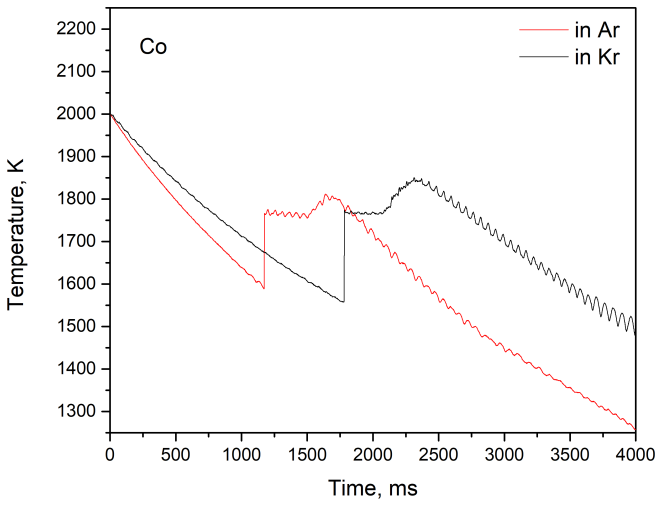

Figure B.7: Cooling curves of liquid Co.

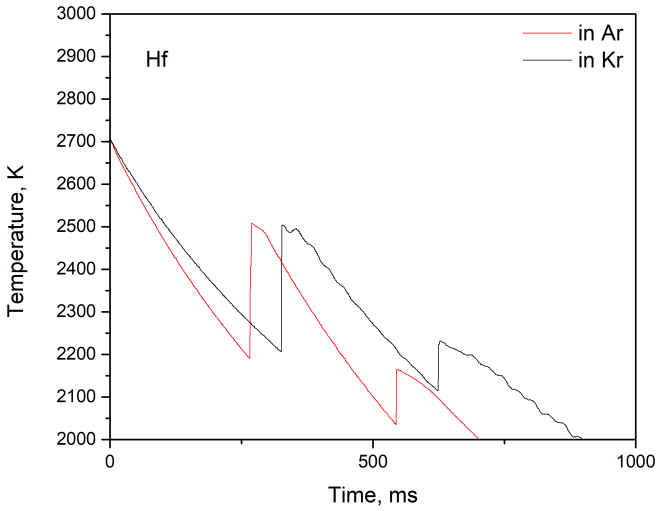

Figure B.8: Cooling curves of liquid Hf.

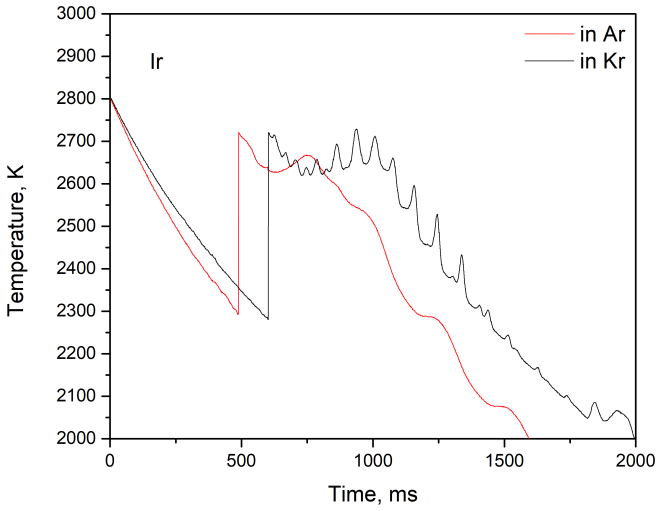

Figure B.9: Cooling curves of liquid Ir.

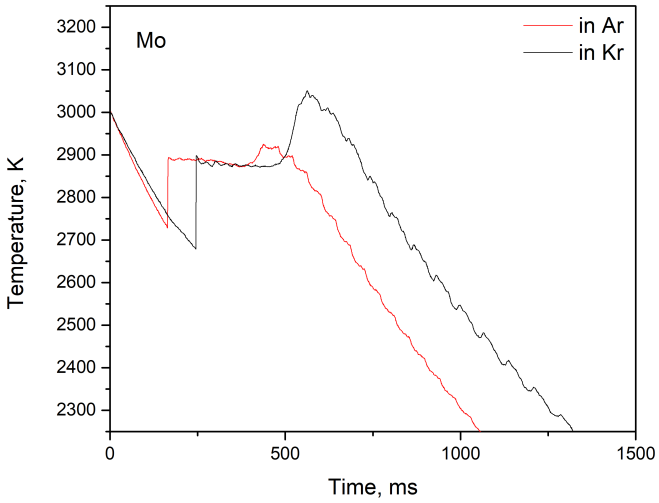

Figure B.10: Cooling curves of liquid Mo.

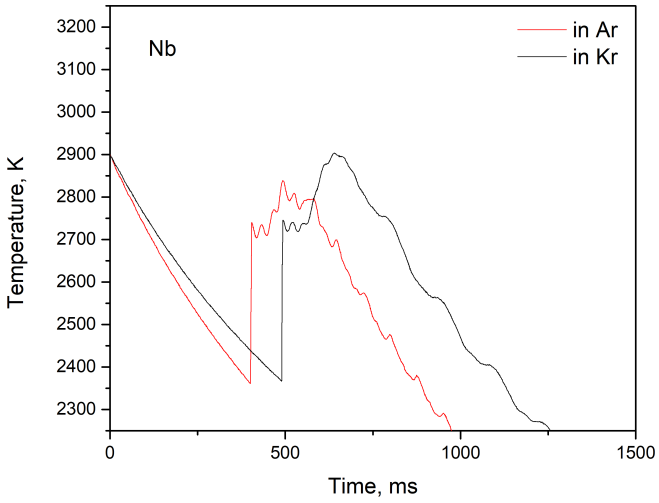

Figure B.11: Cooling curves of liquid Nb.

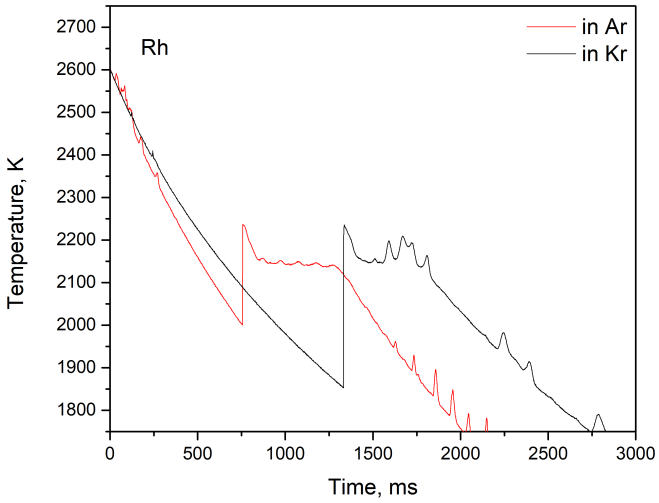

Figure B.12: Cooling curves of liquid Rh.

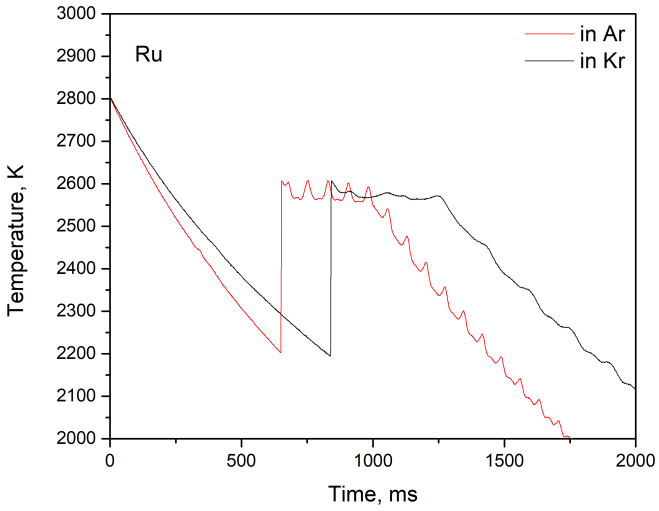

Figure B.13: Cooling curves of liquid Ru.

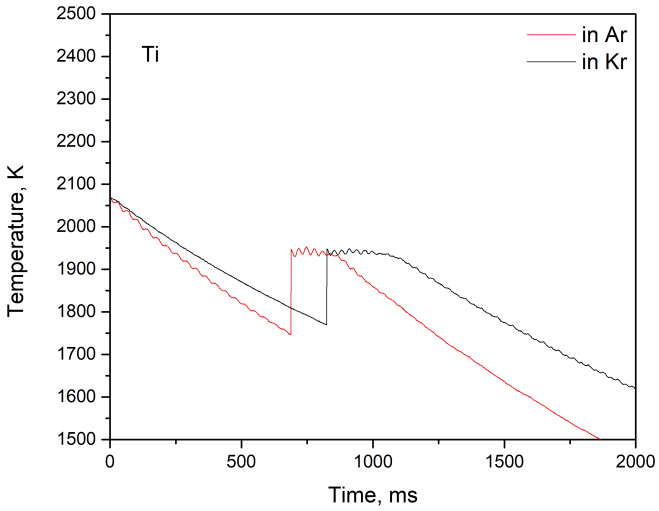

Figure B.14: Cooling curves of liquid Ti.

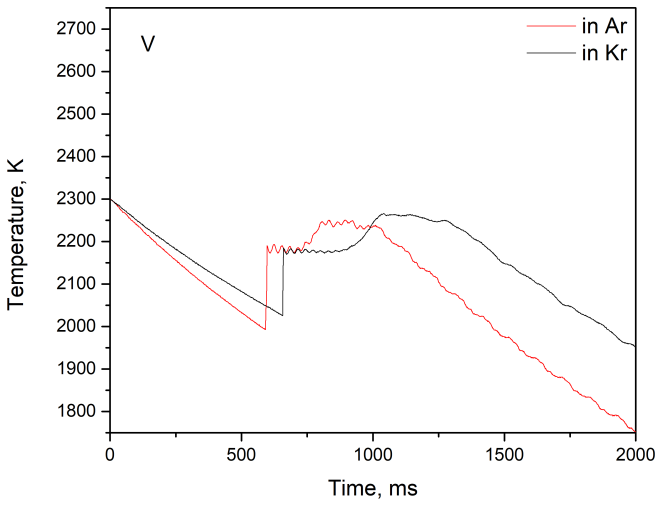

Figure B.15: Cooling curves of liquid V.

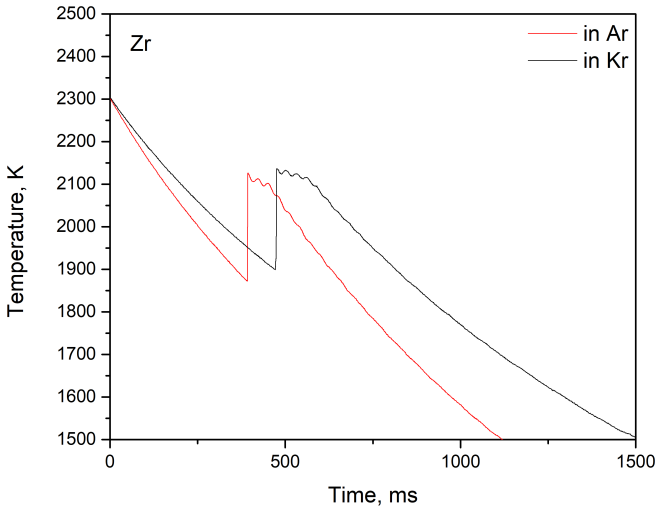

Figure B.16: Cooling curves of liquid Zr.

C

Values of the thermophysical properties used in heat capacity calculations

Density is expressed with the following expression:

$$\rho = \rho_{T_m} + \frac{d\rho}{dT}(T - T_m) \tag{C.1}$$

Element	T_m, K	ρ_{T_m}, kg/m^3	$d\rho/dT$, kg/m^{3}K	Reference
Au	1337	17400	1.44	Paradis et al.[156]
Co	1768	7827	0.936	Crovini et al.[157]
Cu	1358	7900	0.765	Brillo & Egry[158]
Fe	1811	7009	0.8358	Kirshenbaum & Cahill[159]
Hf	2504	12000	0.44	Paradis et al.[82]
Ir	2719	19500	0.85	Ishikawa et al.[71]
Mo	2896	9100	0.6	Paradis et al.[83]
Nb	2742	7950	0.23	Paradis et al.[84]
Ni	1728	7930	1.01	Brillo & Egry[158]
Pd	1833	10660	0.77	Paradis et al.[160]
Pt	2042	19200	0.96	Ishikawa et al.[2]
Ti	1941	4193	0.238	Ozawa et al.[161]
Rh	2236	10820	0.76	Paradis et al.[162]
Ru	2067	10750	0.56	Paradis et al.[163]
V	2183	5460	0.49	Paradis et al.[81]
Zr	2128	6240	0.29	Paradis & Rhim[137]

Table C.1: Densities of the pure elements used in this study.

D

The l=2, 3 spherical harmonics

The spherical harmonic oscillation images were generated using MATLAB R2021b. Images are arranged in the order from top left to bottom right. Only the top views of l=2 mode oscillations are presented because of their relevance with this work.

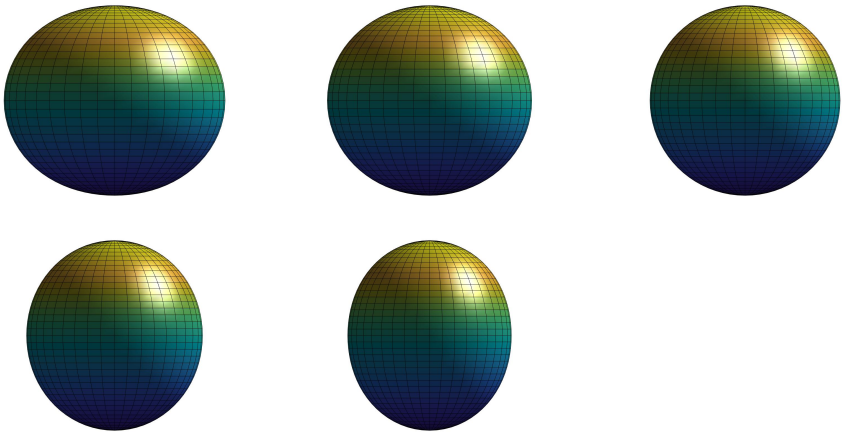

Figure D.1: Front view, l=2 m=0 mode.

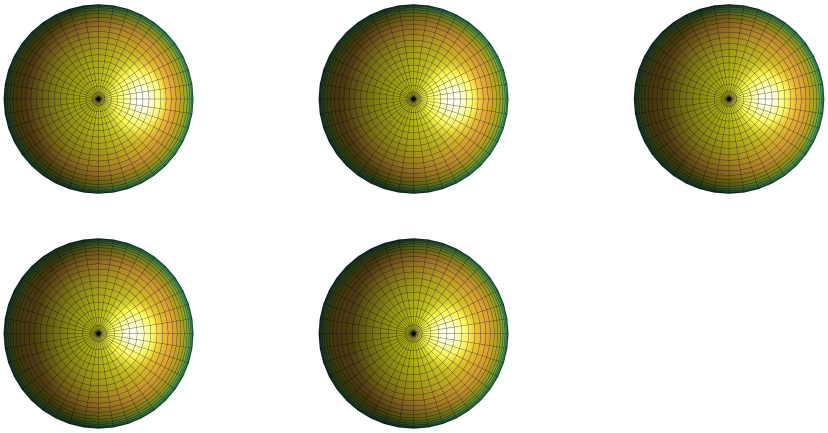

Figure D.2: Top view, l=2 m=0 mode.

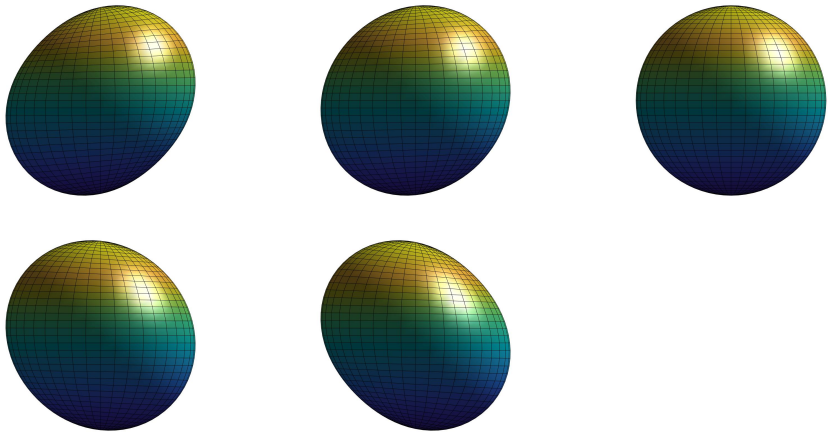

Figure D.3: Front view, l=2 m=±1 mode.

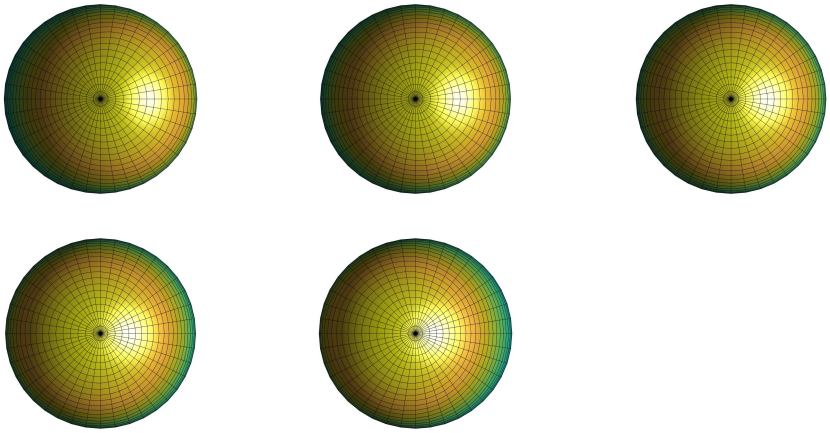

Figure D.4: Top view, l=2 m=±1 mode.

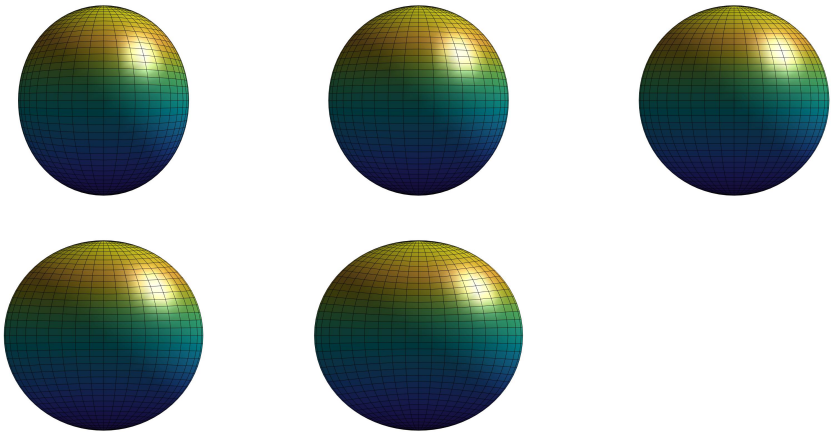

Figure D.5: Front view, l=2 m=±2 mode.

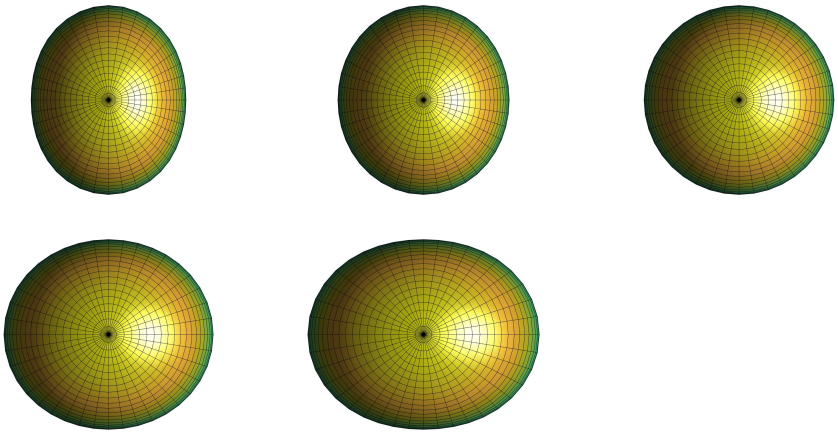

Figure D.6: Top view, l=2 m=±2 mode.

l=3 m=0 mode oscillation

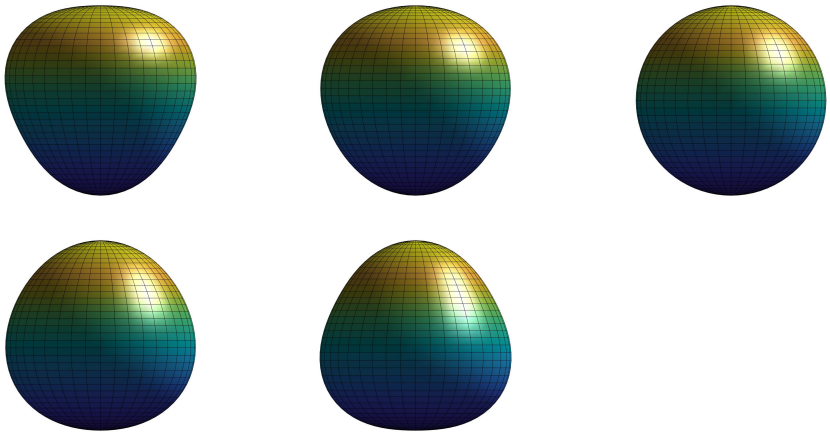

Figure D.7: Front view, l=3 m=0 mode.

l=3 m=±1 mode oscillation

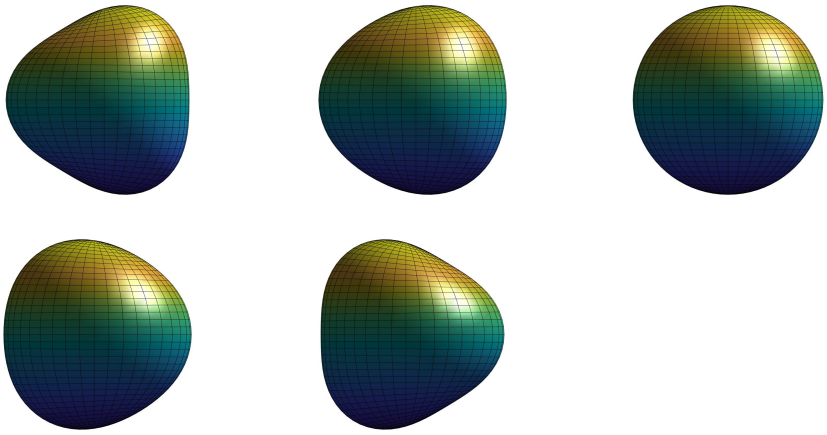

Figure D.8: Front view, l=3 m=±1 mode.

l=3 m=±2 mode oscillation

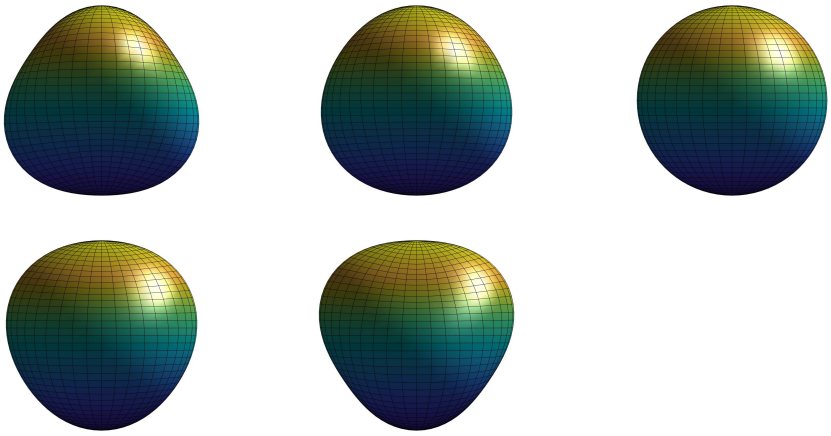

Figure D.9: Front view, l=3 m=±2 mode.

l=3 m=±3 mode oscillation

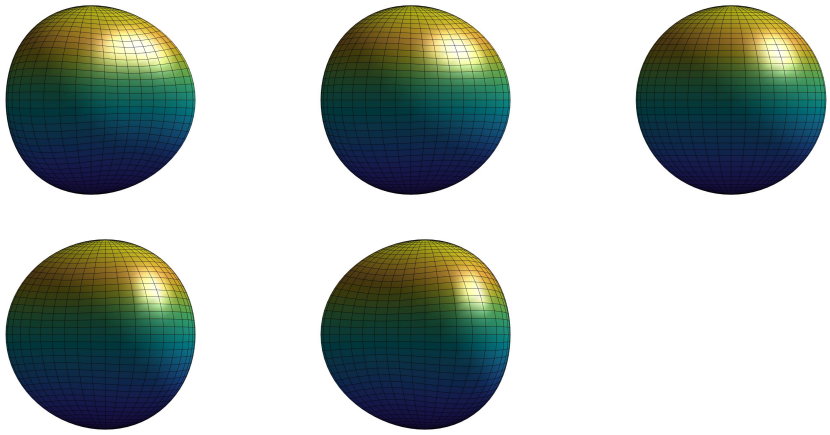

Figure D.10: Front view, l=3 m=±3 mode.

References

[1] J. Brillo. *Thermophysical Properties of Multicomponent Liquid Alloys*. De Gruyter Oldenbourg, 2016.

[2] T. Ishikawa, P. F. Paradis, and N. Koike. Non-contact thermophysical property measurements of liquid and supercooled platinum. *Jpn. J. Appl. Phys.*, 45:1719–1724, 2006.

[3] T. Ishikawa, J. T. Okada, P. F. Paradis, and Y. Watanabe. Measurement of spectral emissivity and constant pressure heat capacity of liquid platinum with an electrostatic levitator. *J. Chem. Thermodynamics.*, 112:7–12, 2017.

[4] D. R. Lide, editor. *CRC Handbook of Chemistry and Physics*. CRC Press, 2003.

[5] R. Gauntt, D. Kalinich, J. Cardoni, J. Phillips, A. Goldmann, S. Pickering, M. Francis, K. Robb, L. Ott, and D. Wang. Fukushima daiichi accident study (status as of april 2012). *Sandia Report*, 6173, 2012.

[6] M. Holt, R. J. Campbell, and M. B. Nikitin. Fukushima nuclear disaster, 2012.

[7] Director General. The fukushima daiichi accident. Technical report, International Atomic Energy Agency, Vienna, Austria, 8 2015.

[8] D. W. Akers, R. K. Mccardell, M. L. Russell, and G. Worku. Tmi-2 core materials and fission product inventory. *Nucl. Eng. Des.*, 118(3):451–461, 1990.

[9] J. M. Broughton, P. Kuan, D. A. Petti, and E. L. Tolman. A scenario of the three mile island unit 2 accident. *Nucl. Technol.*, 87(1):34–53, 1989.

[10] D. W. Akers, S. M. Jensen, and B. K. Schuetz. Examination of relocated fuel debris adjacent to the lower head of the tmi-2 reactor vessel. Technical report, Idaho National Engineering Laboratory, EG&G Idaho, Inc., 3 1994.

[11] S. T. Barlow, D. J. Bailey, A. J. Fisher, M. C. Stennett, C. Gausse, H. Ding, V. A. Krasnov, S. Yu. Sayenko, N. C. Hyatt, and C. L. Corkhill. Synthesis, characterisation and corrosion behaviour of simulant chernobyl nuclear meltdown materials. *npj Mater. Degrad.*, 4(1):3, 2020.

[12] S. A. Bogatov, A. A. Borovoi, A. S. Lagunenko, E. M. Pazukhin, V. F. Strizhov, and V. A. Khvoshchinskii. Formation and spread of chernobyl lavas. *Radiochemistry*, 50(6):650–654, 2008.

[13] E. B. Anderson, B. E. Burakov, and E. M. Pazukhin. High-uranium zircon from "chernobyl lavas". *Radiochimica Acta*, 60(2-3):149–152, 1993.

[14] E. B. Anderson, B. E. Burakov, and E. M. Pazukhin. Chernobylite, a reaction product of nuclear fuel and construction materials of the destroyed fourth block of the chernobyl npp. *Soviet Radiochemistry*, 34(5):624, 1993.

[15] B. E. Burakov, E. B. Anderson, S. I. Shabalev, E. E. Strykanova, S. V. Ushakov, M. Trotabas, J. Y. Blanc, P. Winter, and J. Duco. The behavior of nuclear fuel in first days of the chernobyl accident. *MRS Proceedings*, 465:1297, 1996.

[16] T. Kitagaki, T. Hoshino, K. Yano, N. Okamura, H. Ohara, T. Fukasawa, and K. Koizumi. Mechanical Properties of Cubic (U,Zr)O2. *J. Nucl. Eng. Radiat. Sci.*, 4(3), 05 2018.

[17] M. Marchetti, D. Laux, A. Seibert, P. D. Bottomley, T. Wiss, V. V. Rondinella, and G. Despaux. Elastic properties of severely degraded fuels. *J. Nucl. Mater.*, 529:151918, 2020.

[18] F. Nagase and H. Uetsuka. Thermal properties of three mile island unit 2 core debris and simulated debris. *J. Nucl. Sci. Technol.*, 49(1):96–102, 2012.

[19] J. R. Wolf, J. L. Rempe, L. A. Stickler, G. E. Korth, D. R. Diercks, L. A. Neimark, D. W. Akers, B. K. Schuetz, T. L. Shearer, S. A. Chavez, G. L. Thinnes, R. J. Witt, M. L. Corradini, and J. A. Kos. Tmi-2 vessel investigation project integration report. Technical report, Idaho National Engineering Laboratory, EG&G Idaho, Inc., 3 1994.

[20] A. Seibert, D. Staicu, D. Bottomley, M. Cologna, J. Boshoven, H. Hein, E. Kassim, S. Nourry, M. Ernstberger, D. Robba, and R. Konings. Thermophysical properties of u, zr-oxides as prototypic corium materials. *J. Nucl. Mater.*, 520:165–177, 2019.

[21] T. Yano, editor. *Characterization of the VULCANO test products for fuel debris removal from the Fukushima Daiichi Nuclear Power Plant*, volume 5, 3-7, Shimbashi 2-chome, Minato-ku, Tokyo 105-0004, Japan, 11 2018. The Atomic Energy Society of Japan, The Atomic Energy Society of Japan.

[22] Y. Ohishi, Y. Sun, Y. Ooi, and H. Muta. Mechanical properties and thermal conductivity of (u,zr)sio4. *J. Nucl. Mater.*, 556:153160, 2021.

[23] Y. Sun, Y. Abe, H. Muta, and Y. Ohishi. Mechanical and thermal properties of zr-b and fe-b alloys. *J. Nucl. Sci. Technol.*, 57(8):917–925, 2020.

[24] Y. Ohishi, M. Sugizaki, Y. Sun, H. Muta, and K. Kurosaki. Thermophysical and mechanical properties of crb and feb. *J. Nucl. Sci. Technol.*, 56(9-10):859–865, 2019.

[25] F. Nakamori, Y. Ohishi, H. Muta, K. Kurosaki, K. Fukumoto, and S. Yamanaka. Mechanical and thermal properties of zrsio4. *J. Nucl. Sci. Technol.*, 54(11):1267–1273, 2017.

[26] Y. Ohishi, H. Muta, K. Kurosaki, J. T. Okada, T. Ishikawa, Y. Watanabe, and S. Yamanaka. Thermophysical properties of molten core materials: Zr–fe alloys measured by electrostatic levitation. *J. Nucl. Sci. Technol.*, 53(12):1943–1950, 2016.

[27] F. Nakamori, Y. Ohishi, H. Muta, K. Kurosaki, K. Fukumoto, and S. Yamanaka. Mechanical and thermal properties of bulk zrb2. *J. Nucl. Mater.*, 467:612–617, 2015.

[28] F. Tanabe. Analysis of core melt accident in fukushima daiichi- unit 1 nuclear reactor. *J. Nucl. Sci. Technol.*, 48(8):1135–1139, 2011.

[29] T. Kitagaki, H. Ikeuchi, K. Yano, L. Brissonneau, B. Tormos, R. Domenger, J. Roger, and T. Washiya. Effect of quenching on molten core-concrete interaction product. *J. Nucl. Sci. Technol.*, 56(9-10):902–914, 2019.

[30] T. Kitagaki, K. Yano, H. Ogino, and T. Washiya. Thermodynamic evaluation of the solidification phase of molten core–concrete under estimated fukushima daiichi nuclear power plant accident conditions. *J. Nucl. Mater.*, 486:206–215, 2017.

[31] L. Brissonneau, H. Ikeuchi, P. Piluso, J. Gousseau, C. David, V. Testud, J. Roger, V. Bouyer, T. Kitagaki, A. Nakayoshi, S. Dubois, and T. Washiya. Material characterization of the vulcano corium concrete interaction test with concrete representative of fukushima daiichi nuclear plants. *J. Nucl. Mater.*, 528:151860, 2020.

[32] G. Li, J. Gao, P. Wen, Q. Zhao, J. Wang, J. Yan, and A. Yamaji. A review on mps method developments and applications in nuclear engineering. *Comput. Methods Appl. Mech. Eng.*, 367:113166, 2020.

[33] R. Yokoyama, M. Kondo, S. Suzuki, M. Harada, and K. Okamoto. Investigation of the outflow and spreading-solidification behaviour of stratified molten metal. *J. Nucl. Eng.*, 2(2):168–189, 2021.

[34] T. Kawahara and Y. Oka. Ex-vessel molten core solidification behavior by moving particle semi-implicit method. *J. Nucl. Sci. Technol.*, 49(12):1156–1164, 2012.

[35] G. Duan, A. Yamaji, and M. Sakai. A multiphase mps method coupling fluid–solid interaction/phase-change models with application to debris remelting in reactor lower plenum. *Ann. Nucl. Energy*, 166:108697, 2022.

[36] X. Li and A. Yamaji. A numerical study of isotropic and anisotropic ablation in mcci by mps method. *Prog. Nucl. Energy*, 90:46–57, 2016.

[37] C. Ronchi, J. P. Hiernaut, R. Selfslag, and G. J. Hyland. Laboratory measurement of the heat capacity of urania up to 8000 k: I. experiment. *Nucl. Sci. Eng.*, 113(1):1–19, 1993.

[38] H. C. Tsai and D. R. Olander. The viscosity of molten uranium dioxide. *J. Nucl. Mater.*, 44(1):83–86, 1972.

[39] R. E. Woodley. The viscosity of molten uranium dioxide. *J. Nucl. Mater.*, 50(1):103–106, 1974.

[40] O. L. G. Alderman, C. J. Benmore, J. K. R. Weber, L. B. Skinner, A. J. Tamalonis, S. Sendelbach, A. Hebden, and M. A. Williamson. Corium lavas: structure and properties of molten uo2-zro2 under meltdown conditions. *Sci. Rep.*, 8(1):2434, 2018.

[41] J. K. R. Weber, A. Tamalonis, C. J. Benmore, O. L. G. Alderman, S. Sendelbach, A. Hebden, and M. A. Williamson. Aerodynamic levitator for in situ x-ray structure measurements on high temperature and molten nuclear fuel materials. *Rev. Sci. Instrum.*, 87(7):073902, 2016.

[42] L. B. Skinner, C. J. Benmore, J. K. R. Weber, M. A. Williamson, A. Tamalonis, A. Hebden, T. Wiencek, O. L. G. Alderman, M. Guthrie, L. Leibowitz, and J. B. Parise. Molten uranium dioxide structure and dynamics. *Science*, 346(6212):984–987, 2014.

[43] O. L. G. Alderman, C. J. Benmore, J. K. R. Weber, L. B. Skinner, A. J. Tamalonis, S. Sendelbach, A. Hebden, and M. A. Williamson. The structure of liquid uo2- x in reducing gas atmospheres. *Appl. Phys. Lett.*, 110(8):081904, 2017.

[44] T. Kondo, H. Muta, K. Kurosaki, F. Kargl, A. Yamaji, M. Furuya, and Y. Ohishi. Density and viscosity of liquid zro2 measured by aerodynamic levitation technique. *Heliyon*, 5(7):e02049, 2019.

[45] T. Kondo, H. Muta, and Y. Ohishi. Droplet impingement method to measure the surface tension of molten zirconium oxide. *J. Nucl. Sci. Technol.*, 57(8):889–897, 2020.

[46] D. L. Maux, M. Courtois, T. Pierre, B. Lamien, and P. L. Masson. Density measurement of liquid 22mnb5 by aerodynamic levitation. *Rev. Sci. Instrum.*, 90:074904, 2019.

[47] B. Glorieux, M. Saboungi, F. Millot, J. Enderby, and J. Rifflet. Aerodynamic levitation: an approach to microgravity. *AIP Conf. Proc.*, 552:316–324, 2001.

[48] F. Kargl, C. Yuan, and G. N. Greaves. Aerodynamic levitation: Thermophysical property measurements of liquid oxides. *Int. J. Microgravity Sci. Appl.*, 32:320212, 2015.

[49] J. M. Borgard, A. Quaini, L. Soldi, E. Lizon, and T. Alpettaz. Simulation of an aerodynamic furnace for high temperature thermodynamic data acquisition, 2018.

[50] F. Millot, J. C. Rifflet, V. Sarou-Kanian, and G. Wille. High-temperature properties of liquid boron from contactless techniques. *Int. J. Thermophys.*, 23:1185–1195, 2002.

[51] J. W. Strutt. Vi. on the capillary phenomena of jets. *Proc. R. Soc. Lond.*, 29(196-199):71–97, 1879.

[52] W. K. Rhim, S. K. Chung, D. Barber, K. F. Man, G. Gutt, A. Rulison, and R. E. Spjut. An electrostatic levitator for high-temperature containerless materials processing in 1-g. *Rev. Sci. Instrum.*, 64(10):2961–2970, 1993.

[53] W. K. Rhim and K. Ohsaka. Thermophysical properties measurement of molten silicon by high-temperature electrostatic levitator: density, volume expansion, specific heat capacity, emissivity, surface tension and viscosity. *J. Cryst. Growth*, 208(1):313–321, 2000.

[54] W. K. Rhim, K. Ohsaka, P. F. Paradis, and R. E. Spjut. Noncontact technique for measuring surface tension and viscosity of molten materials using high temperature electrostatic levitation. *Rev. Sci. Instrum.*, 70(6):2796–2801, 1999.

[55] T. Ishikawa, J. T. Okada, Y. Watanabe, H. Tamaru, and Y. Nakamura. Thermophysical property measurements of oxide melts at high temperature by electrostatic levitation furnace on the iss. *Int. J. Microgravity Sci. Appl.*, 32:320410, 2015.

[56] C. Koyama, T. Ishikawa, H. Oda, H. Saruwatari, S.Ueno, M. Oshio, Y. Watanabe, and Y. Nakata. Densities of liquid lanthanoid sesquioxides measured with the electrostatic levitation furnace in the iss. *J. Am. Ceram. Soc.*, 104:2913–2918, 2021.

[57] A. Seidel, W. Soellner, and C. Stenzel. Eml - an electromagnetic levitator for the international space station. *J. Phys.: Conf. Ser.*, 327, 2011.

[58] X. Xiao, J. Brillo, J. Lee, R. W. Hyers, and D. M. Matson. Impact of convection on the damping of an oscillating droplet during viscosity measurement using the iss-eml facility. *npj Microgravity*, 7, 2021.

[59] M. Mohr, R. Wunderlich, R. Novakovic, E. Ricci, and H.J. Fecht. Precise measurements of thermophysical properties of liquid ti–6al–4v (ti64) alloy on board the international space station. *Adv. Eng. Mater.*, 22(7), 2020.

[60] R. K. Wunderlich, M. Mohr, Y. Dong, U. Hecht, D. M. Matson, R. Hyers, G. Bracker, J. Lee, S. Schneider, X. Xiao, and H.J. Fecht. Thermophysical properties of the tial-2cr-2nb alloy in the liquid phase measured with an electromagnetic levitation device on board the international space station, iss-eml. *Int. J. Mater. Res.*, 112(10):770–781, 2021.

[61] A. K. Gangopadhyay, M. E. Sellers, G. P. Bracker, D. Holland-Moritz, D. C. Van Hoesen, S. Koch, P. K. Galenko, A. K. Pauls, R. W. Hyers, and K. F. Kelton. Demonstration of the effect of stirring on nucleation from experiments on the international space station using the iss-eml facility. *npj Microgravity*, 7, 2021.

[62] D. Langstaff, M. Gunn, G. N. Greaves, A. Marsing, and F. Kargl. Aerodynamic levitator furnace for measuring thermophysical properties of refractory liquids. *Rev. Sci. Instrum.*, 84, 2013. 124901.

[63] O. L. G. Alderman, M. Liška, J. Macháček, C. J. Benmore, A. Lin, A. Tamalonis, and J. K. R. Weber. Temperature-driven structural transitions in molten sodium borates na20–b203: X-ray diffraction, thermodynamic modeling, and implications for topological constraint theory. *J. Phys. Chem. C*, 120(1):553–560, 01 2016.

[64] S. Kohara, J. Akola, L. Patrikeev, M. Ropo, K. Ohara, M. Itou, A. Fujiwara, J. Yahiro, J.T. Okada, T. Ishikawa, A. Mizuno, A. Masuno, Y. Watanabe, and T. Usuki. Atomic and electronic structures of an extremely fragile liquid. *Nat. Commun.*, 5(1):5892, 2014.

[65] I. Egry, H. Giffard, and S. Schneider. The oscillating drop technique revisited. *Meas. Sci. Technol.*, 16(2):426–431, 2005.

[66] H. Lamb. On the oscillations of a viscous spheroid. *Proc. London Math. Soc.*, s1-13(1):51–70, 1881.

[67] G. Lohöfer. Viscosity measurement by the "oscillating drop method": The case of strongly damped oscillations. *Int. J. Thermophys.*, 41, 2020.

[68] N. Brosius, K. Ward, E. Wilson, Z. Karpinsky, M. SanSoucie, T. Ishikawa, S. Matsumoto, and R. Narayanan. Benchmarking surface tension measurement method using two oscillation modes in levitated liquid metals. *npj Microgravity*, 10:2373–8065, 2021.

[69] J. Q. Feng and K. V. Beard. Small-amplitude oscillations of electrostatically levitated drops. *Proc. R. Soc. A*, 430(1878):133–150, 1990.

[70] H. Fukuyama and Y. Waseda. *High-Temperature Measurements of Materials*, volume 11 of *Advances in Materials Research*. Springer, Berlin, Heidelberg, first edition, 2009.

[71] P. F. Paradis, T. Ishikawa, and S. Yoda. Ground-based thermophysical property measurements of supercooled and liquid platinum-group metals by electrostatic levitation. *Microgravity Sci. Technol.*, 16:94–98, 2005.

[72] D. L. Cummings and D. A. Blackburn. Oscillations of magnetically levitated aspherical droplets. *J. Fluid Mech.*, 224:395–416, 1991.

[73] F. H. Busse. Oscillations of a rotating liquid drop. *J. Fluid Mech.*, 142:1–8, 1984.

[74] I. Egry, G. Lohoefer, and G. Jacobs. Surface tension of liquid metals: Results from measurements on ground and in space. *Phys. Rev. Lett.*, 75:4043–4046, Nov 1995.

[75] J. Jackson. *Classical Electrodynamics*. Wiley, New York, 1967.

[76] J. Brillo, G. Lohofer, F. Hohagen, S. Schneider, and I. Egry. Thermophysical property measurements of liquid metals by electromagnetic levitation. *Int. J. Mater. Prod. Technol.*, 26:247–273, 2006.

[77] J. A. Treverton and J. L. Margrave. Thermodynamic properties by levitation calorimetry iii. the enthalpies of fusion and heat capacities for the liquid phases of iron, titanium, and vanadium. *J. Chem. Thermodyn.*, 3(4):473–481, 1971.

[78] C. Tackes. Thermal analysis of undercooled metallic liquids by electromagnetic levitation drop calorimetry. Master's thesis, Iowa State University, 2013.

[79] R. K. Wunderlich, D. S. Lee, W. L. Johnson, and H. J. Fecht. Noncontact modulation calorimetry of metallic liquids in low earth orbit. *Phys. Rev. B*, 55:26–29, Jan 1997.

[80] H. Fukuyama, H. Kobatake, K. Takahashi, I. Minato, T. Tsukada, and S. Awaji. Development of modulated laser calorimetry using a solid platinum sphere as a reference. *Meas. Sci. Technol.*, 18(7):2059–2066, 2007.

[81] P. F. Paradis, T. Ishikawa, T. Aoyama, and S. Yoda. Thermophysical properties of vanadium at high temperature measured with an electrostatic levitation furnace. *J. Chem. Thermodyn.*, 34:1929–1942, 2002.

[82] P. F. Paradis, T. Ishikawa, and S. Yoda. Non-contact measurements of the thermophysical properties of hafnium-3 mass% zirconium at high temperature. *Int. J. Thermophys.*, 24:239–258, 2003.

[83] P. F. Paradis, T. Ishikawa, and S. Yoda. Noncontact measurements of thermophysical properties of molybdenum at high temperatures. *Int. J. Thermophys.*, 23:555–569, 2002.

[84] P. F. Paradis, T. Ishikawa, and S. Yoda. Non-contact measurements of thermophysical properties of niobium at high temperature. *J. Mater. Sci.*, 36:5125–5130, 2001.

[85] P. F. Paradis and W. K. Rhim. Non-contact measurements of thermophysical properties of titanium at high temperature. *J. Chem. Thermodyn.*, 32:123–133, 2000.

[86] T. Ishikawa, Y. Ito, J. T. Okada, P. F. Paradis, Y. Watanabe, and T. Masaki. Spectral emissivity measurements of liquid refractory metals by spectrometers combined with an electrostatic levitator. *Meas. Sci. Technol.*, 23:125602, 2012.

[87] T. Ishikawa, J. T. Okada, P. F. Paradis, and Y. Watanabe. Emissivity measurements of molten metals with an electrostatic levitator. *Int. J. Microgravity Sci. Appl.*, 34, 2017. 340305.

[88] T. Ishikawa, C. Koyama, Y. Nakata, Y. Watanabe, and P. F. Paradis. Spectral emissivity, hemispherical total emissivity, and constant pressure heat capacity of liquid vanadium measured by an electrostatic levitator. *J. Chem. Thermodyn.*, 163:106598, 2021.

[89] K. Sakata, Y. Watanabe, J.T. Okada, M.V. Kumar, P.F. Paradis, and T. Ishikawa. Ft-ir emissivity measurements of nb melt using an electrostatic levitation furnace. *J. Chem. Thermodyn.*, 91:116–120, 2015.

[90] T. Ishikawa, J. T. Okada, P.F. Paradis, and Y. Watanabe. Spectral emissivity and constant pressure heat capacity of molten nickel and rhodium measured by spectrometers combined with an electrostatic levitator. *J. Chem. Thermodyn.*, 103:107–114, 2016.

[91] T. Ishikawa, C. Koyama, Y. Nakata, Y. Watanabe, and P. F. Paradis. Spectral emissivity and constant pressure heat capacity of liquid titanium measured by an electrostatic levitator. *J. Chem. Thermodyn.*, 131:557–562, 2019.

[92] D. M. Herlach. Non-equilibrium solidification of undercooled metallic melts. *Metals*, 4:186–234, 2014.

[93] S. Jeon, M. P. Sansoucie, and D. M. Matson. Hypercooling limit, heat of fusion, and temperature-dependent specific heat of fe-cr-ni melts. *J. Chem. Thermodyn.*, 138:51–58, 2019.

[94] S. V. Ushakov, A. Shvarev, T. Alexeev, D. Kapush, and A. Navrotsky. Drop-and-catch (dnc) calorimetry using aerodynamic levitation and laser heating. *J. Am. Cerm. Soc.*, 100:754–760, 2016.

[95] P. F. Paradis, T. Ishikawa, J. Yu, and S. Yoda. Hybrid electrostatic–aerodynamic levitation furnace for the high-temperature processing of oxide materials on the ground. *Rev. Sci. Instrum.*, 72(6):2811–2815, 2001.

[96] P. F. Paradis, J. Yu, T. Ishikawa, T. Aoyama, and S. Yoda. Contactless density measurement of high-temperature $bifeo_3$ and $batio_3$. *Appl. Phys. A*, 79:1965–1969, 2004.

[97] P. F. Paradis and T. Ishikawa. Surface tension and viscosity measurements of liquid and undercooled alumina by containerless techniques. *Jpn. J. Appl. Phys.*, 44(7A):5082–5085, 2005.

[98] T. Ishikawa, P. F. Paradis, N. Koike, and Y. Watanabe. Effects of the positioning force of electrostatic levitators on viscosity measurements. *Rev. Sci. Instrum.*, 80(1):013906, 2009.

[99] Y. Arai, P. F. Paradis, T. Aoyama, T. Ishikawa, and S. Yoda. An aerodynamic levitation system for drop tube and quenching experiments. *Rev. Sci. Intrum.*, 74:1057–1063, 2003.

[100] S. V. Ushakov, A. Shvarev, T. Alexeev, D. Kapush, and A. Navrotsky. Drop-and-catch (dnc) calorimetry using aerodynamic levitation and laser heating. *J. Am. Ceram. Soc.*, 100:754–760, 2017.

[101] T. Ishikawa, P. F. Paradis, and S. Yoda. New sample levitation initiation and imaging techniques for the processing of refractory metals with an electrostatic levitator furnace. *Rev. Sci. Instrum.*, 72:2490–2495, Apr 2001.

[102] S. Krishnan, G. P. Hansen, R. H. Hauge, and J. L. Margrave. *Emissivities and optical constants of electromagnetically levitated liquid metals as functions of temperature and wavelength*, volume 1. Humana Press, Totowa, NJ, 1990.

[103] F. Wust, A. Meuthen, and R. Durrer. *Die Temperatur-Wärmeinhaltskurven der technisch wichtigen Metalle*. Springer, Berlin, Heidelberg, 1918.

[104] S. Umino. Latent heat of fusion and the heat of transformation of some metals. *Sci. Rep. Tohuku Univ.*, 15:597–617, 1926.

[105] E. M. Plaza. Thermodynamics of Solid and Liquid AuSn and Heat Contents of Gold and Tin. Technical report, U.S. Atomic Energy Commission, 1967. Report UCRL-17401.

[106] 14 - general physical properties. In W. F. Gale and T. C. Totemeier, editors, *Smithells Metals Reference Book (Eighth Edition)*, pages 14–1–14–45. Butterworth-Heinemann, Oxford, eighth edition edition, 2004.

[107] J. W. Tester, R. C. Feber, and C. C. Herrick. Calorimetric study of liquid gold. *J. Chem. Eng. Data*, 13:419–421, 1968.

[108] N. Wang, X. J. Han, and B. Wei. Specific heat and thermodynamics properties of undercooled liquid cobalt. *Appl. Phys. Lett.*, 80:28–30, 2001.

[109] M. Watanabe, J. Takano, M. Adachi, M. Uchikoshi, and H. Fukuyama. Thermophysical properties of liquid co measured by electromagnetic levitation technique in a static magnetic field. *J. Chem. Thermodyn*, 121:145–152, 2018.

[110] H. Hess, E. Kaschnitz, and G. Pottlacher. Thermophysical properties of liquid cobalt. *High Press. Res.*, 12:29–42, 1994.

[111] J. A. Treverton and J. L. Margrave. Levitation calorimetry. iv. the thermodynamic properties of liquid cobalt and palladium. *J. Phys. Chem.*, 75:3737–3740, 1971.

[112] J. L. Margrave. Determination of thermophysical properties of liquid metals at high temperatures by levitation methods. *Mater. Sci. Eng. A*, 178:83–88, 1994.

[113] V. Ya. Chekhovskoi, V. D. Tarasov, and Yu. V. Gusev. Calorific properties of liquid copper. *High Temp.*, 38:394–399, 2000.

[114] M. W. Chase. *NIST-JANAF Thermochemical Tables, 4th Edition*. American Institute of Physics, 1998.

[115] W. Dokko and R. G. Bautista. The high temperature heat content and heat capacity of liquid cerium-copper alloys by levitation calorimetry. *Metall. Trans. B*, 11:511–518, 1980.

[116] J. R. Wilson. The structure of liquid metals and alloys. *Metall. Rev.*, 10:381–590, 1965.

[117] M. Beutl, G. Pottlacher, and H. Jager. Thermophysical properties of liquid iron. *Int. J. Thermophys.*, 15:1323–1331, 1994.

[118] V. N. Korobenko, O. A. Polyakova, and A. I. Savvatimskii. Heat capacity of liquid hafnium from the melting point to the boiling point at atmospheric pressure. *High Temp.*, 43:38–44, 2005.

[119] S. Kang, D. H. Jeon, H. Yoo, J. T. Ishikawa, T. Okada, P. F. Paradis, and G. W. Lee. Nano-sized nucleus-supercooled liquid interfacial free energy and thermophysical properties of early and late transition liquid metals. *Cryst. Growth Des.*, 14:1103–1109, 2014.

[120] C. Cagran and G. Pottlacher. Thermophysical properties and normal spectral emittance of iridium up to 3500 k. *Int. J. Thermophys.*, 28:697–710, 2007.

[121] D. V. Minakov, M. A. Paramonov, and P. R. Levashov. Thermophysical properties of liquid molybdenum in the near-critical region using quantum molecular dynamics. *Phys. Rev. B*, 103:184204, 2021.

[122] C. Cagran, B. Wilthan, and G. Pottlacher. Normal spectral emissivity at a wavelength of 684.5 nm and thermophysical properties of solid and liquid molybdenum. *Int. J. Thermophys.*, 25:1551–1566, 2004.

[123] G. Pottlacher, E. Kaschnitz, and H. Jager. High-pressure, high-temperature thermophysical measurements on molybdenum. *J. Phys. Condens. Matter*, 3:5783–5792, 1991.

[124] K. Boboridis. Thermophysical property measurements on niobium and titanium by a microsecond-resolution pulse-heating technique using high-speed laser polarimetry and radiation thermometry. *Int. J. Thermophys*, 23:277–291, 2002.

[125] A. Cezairliyan and J. L. McClure. Heat capacity and electrical resistivity of liquid niobium near its melting temperature. *Int. J. Thermophys*, 8:803–808, 1987.

[126] O. Vollmer, R. Kohlhaas, and M. Braun. Die schmelzwärme und die atomwärme im schmelzflüssigen bereich von eisen, kobalt und nickel. *Z. Naturforsch.*, 21a:181–182, 1966.

[127] H. Geoffray, A. Ferier, and M. Olette. Mesure de la capacité calorifique du nickel à température élevée, de 1120 à 1919°c. *Compt. Rend.*, 256:139–141, 1963.

[128] C. Cagran and G. Pottlacher. Thermophysical properties of palladium. *Platinum Metals Rev.*, 50:144–149, 2006.

[129] J. W. Arblaster. The thermodynamic properties of palladium on its-90. *Calphad*, 19:327–337, 1995.

[130] R. I. L. Guthrie and T. Iida. Thermodynamic properties of liquid metals. *Mater. Sci. Eng.*, A178:35–41, 1994.

[131] M. Watanabe, M. Adachi, and H. Fukuyama. Heat capacities and thermal conductivities of palladium and titanium melts and correlation between thermal diffusivity and density of states for transition metals in a liquid state. *J. Mol. Liq.*, 324:115138, 2021.

[132] P. F. Paradis, T. Ishikawa, and S. Yoda. Ground-based thermophysical property measurements of supercooled and liquid platinum-group metals by electrostatic levitation. *Microgravity Sci. Technol.*, 16:94–98, 2005.

[133] I. Barin, O. Knacke, and O. Kubaschewski. *Thermochemical properties of inorganic substances*. Springer-Verlag Berlin Heidelberg, first edition, 1977.

[134] T. Hupf, C. Cagran, B. Wilthan, and G. Pottlacher. Thermophysical properties of rhodium obtained by fast pulse-heating. *J. Phys. Condens. Matter*, 21:125701, 2009.

[135] B. Wilthan, C. Cagran, and G. Pottlacher. Combined dsc and pulse-heating measurements of electrical resistivity and enthalpy of tungsten, niobium, and titanium. *Int. J. Theromphys.*, 26:1017–1029, 2005.

[136] G. Pottlacher, T. Hupf, B. Wilthan, and C. Cagran. Thermophysical data of liquid vanadium. *Thermochim. Acta*, 461:88–95, 2007.

[137] P. F. Paradis and W. K. Rhim. Thermophysical properties of zirconium at high temperature. *J. Mater. Res.*, 14:3713–3719, 1999.

[138] C. Brunner, C. Cagran, A. Seifter, and G. Pottlacher. The normal spectral emissivity at a wavelength of 684.5 nm and thermophysical properties of liquid zirconium up to the end of the stable liquid phase. *AIP Conf. Proc.*, 684:771–776, 2003.

[139] V. Pletser. *Preparation of Space Experiments*. IntechOpen, 2020.

[140] B. Wilthan, C. Cagran, and G. Pottlacher. Combined dsc and pulse-heating measurements of electrical resistivity and enthalpy of platinum, iron, and nickel. *Int. J. Thermophys.*, 25(5):1519–1534, 2004.

[141] R. S. Hixson and M. A. Winkler. Thermophysical properties of liquid platinum. *Int. J. Thermophys.*, 14:409–416, 1993.

[142] S. Mehmood, U. E. Klotz, and G Pottlacher. Thermophysical properties of platinum-copper alloys. *Metall. Mater. Trans. A*, 43:5029–5037, 2012.

[143] S. J. McCormack, A. Tamalonis, R. J. K. Weber, and W. M. Kriven. Temperature gradients for thermophysical and thermochemical property measurements to 3000 °c for an aerodynamically levitated spheroid. *Rev. Sci. Instrum.*, 90(1):015109, 2019.

[144] X. Ge, X. Xu, Q. Hua, W. Lu, L. Yang, S. Cao, M. Xia, and J. Lia. Ambiguous temperature difference in aerodynamic levitation process: Modelling, solving and application. *J. Mater. Sci. Technol.*, 35(8):1636–1643, 2019.

[145] J. Schroers, S. Bossuyt, W. K. Rhim, J. Li, Z. Zhou, and W. L. Johnson. Enhanced temperature uniformity by tetrahedral laser heating. *Rev. Sci. Instrum.*, 75(11):4523–4527, 2004.

[146] J. Brillo and G. Kolland. Surface tension of liquid Al-Au binary alloys. *J. Mater. Sci.*, 51:4888, 2016.

[147] Yu. V. Zubarev, V. I. Kostikov, B. S. Mitin, Yu. A. Nagibin, and V. V. Nischeta. Certain properties of molten (liquid) aluminum oxide. *Izv. Akad. Nauk SSSR Neorg. Mat*, 5:1563, 1968.

[148] E. E. Shpil'rain, K. A. Yakimovich, and A. F. Tsitsarkin. Experimental study of the density of liquid alumina up to 2750°c. *High Temp. High Press.*, 5:191–198, 1973.

[149] B. Glorieux, F. Millot, and J. C. Rifflet. Surface tension of liquid alumina from contactless techniques. *Int. J. Thermophys.*, 23(5):1249–1257, 2002.

[150] J. L. Bates, C. E. McNeilly, and J. J. Rasmussen. Properties of molten ceramics. In *Ceramics in Severe Environments*, pages 11–26. Springer, 1971.

[151] V. P. Elyutin. Properties of liquid aluminum oxide. *Fiz. Aerodisper-snykh Sist*, 57(7):104–109, 1972.

[152] W. Aniszewski, T. Arrufat, M. Crialesi-Esposito, S. Dabiri, D. Fuster, Y. Ling, J. Lu, L. Malan, S. Pal, R. Scardovelli, G. Tryggvason, P. Yecko, and S. Zaleski. Parallel, robust, interface simulator (paris). *Comput. Phys. Commun.*, 263:107849, 2021.

[153] M. Watanabe, M. Adachi, M. Uchikoshi, and H. Fukuyama. Densities of pt–x (x: Fe, co, ni and cu) binary melts and thermodynamic correlations. *Fluid Ph. Equilibria*, 515:112596, 2020.

[154] E. L. Dubin, V. M. Vlasov, A. I. Timofeev, S. O. Safonov, and A. I. Chegodaev. Температурная зависимость поверхностного натяжения и плотности платины и родия. *Izv. V. U. Z. Tsvetn. Metall.*, 4:160–161, 1975.

[155] G. R. Gathers, J. W. Shaner, and W. M. Hodgson. Thermodynamic characterization of liquid metals at high temperature by isobaric expansion measurements. *High Temp. High Press.*, 11:529–538, 1979.

[156] P. F. Paradis, T. Ishikawa, and N. Koike. Density of liquid gold measured by a non-contact technique. *Gold Bull.*, 41:242–245, 2008.

[157] L. Crovini, R. E. Bedford, and A. Moser. Extended list of secondary reference points. *Metrologia*, 13(4):197–206, oct 1977.

[158] J. Brillo and I. Egry. Density determination of liquid copper, nickel, and their alloys. *Int. J. Thermophys.*, 24(4):1155–1170, 2003.

[159] A. D. Kirshenbaum and J. A. Cahill. The density of liquid iron from the melting point to 2500 k. *Trans. Met. Soc. AIME*, 224, 8 1962.

[160] P. F. Paradis, T. Ishikawa, Y. Saita, and S. Yoda. Containerless property measurements of liquid palladium. *Int. J. Thermophys.*, 25:1905–1912, 2004.

[161] S. Ozawa, Y. Kudo, K. Kuribayashi, Y. Watanabe, and T. Ishikawa. Precise density measurement of liquid titanium by electrostatic levitator. *Mater. Trans.*, 58(12):1664–1669, 2017.

[162] P. F. Paradis, T. Ishikawa, and S. Yoda. Thermophysical property measurements of supercooled and liquid rhodium. *Int. J. Thermophys.*, 24:1121–1136, 2003.

[163] P. F. Paradis, T. Ishikawa, and S. Yoda. Thermophysical properties of liquid and supercooled ruthenium measured by noncontact methods. *J. Mater. Res.*, 19(2):590–594, 2004.

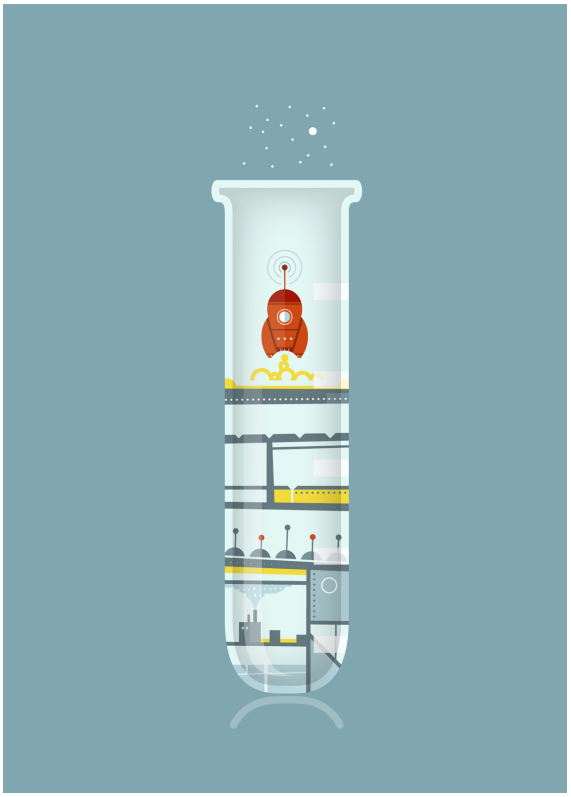

This thesis was typeset using LaTeX, originally developed by Leslie Lamport and based on Donald Knuth's TeX. The body text is set in 11 point Egenolff-Berner Garamond, a revival of Claude Garamont's humanist typeface. The above illustration, "Science Experiment 02", was created by Ben Schlitter and released under CC BY-NC-ND 3.0. A template that can be used to format a PhD thesis with this look and feel has been released under the permissive MIT (X11) license, and can be found online at github.com/suchow/Dissertate or from its author, Jordan Suchow, at suchow@post.harvard.edu.